

# Advanced MOSFET Designs and Implications for SRAM Scaling

*Changhwan Shin  
Tsu-Jae King Liu, Ed.  
Borivoje Nikolic, Ed.  
Eugene Haller, Ed.*

Electrical Engineering and Computer Sciences  
University of California at Berkeley

Technical Report No. UCB/EECS-2012-50

<http://www.eecs.berkeley.edu/Pubs/TechRpts/2012/EECS-2012-50.html>

May 1, 2012



Copyright © 2012, by the author(s).  
All rights reserved.

Permission to make digital or hard copies of all or part of this work for personal or classroom use is granted without fee provided that copies are not made or distributed for profit or commercial advantage and that copies bear this notice and the full citation on the first page. To copy otherwise, to republish, to post on servers or to redistribute to lists, requires prior specific permission.

Advanced MOSFET Designs and Implications for SRAM Scaling

By

Changhwan Shin

A dissertation submitted in partial satisfaction of the

requirements for the degree of

Doctor of Philosophy

in

Engineering - Electrical Engineering and Computer Sciences

in the

Graduate Division

of the

University of California, Berkeley

Committee in charge:

Professor Tsu-Jae King Liu, Chair

Professor Borivoje Nikolić

Professor Eugene E. Haller

Spring 2011

Advanced MOSFET Designs and Implications for SRAM Scaling

Copyright © 2011

by

Changhwan Shin

## Abstract

### Advanced MOSFET Designs and Implications for SRAM Scaling

by

Changhwan Shin

Doctor of Philosophy in Engineering – Electrical Engineering and Computer Sciences

University of California, Berkeley

Professor Tsu-Jae King Liu, Chair

Continued planar bulk MOSFET scaling is becoming increasingly difficult due to increased random variation in transistor performance with decreasing gate length, and thereby scaling of SRAM using minimum-size transistors is further challenging. This dissertation will discuss various advanced MOSFET designs and their benefits for extending density and voltage scaling of static memory (SRAM) arrays. Using three-dimensional (3-D) process and design simulations, transistor designs are optimized. Then, using an analytical compact model calibrated to the simulated transistor current-*vs.*-voltage characteristics, the performance and yield of six-transistor (6-T) SRAM cells are estimated. For a given cell area, fully depleted silicon-on-insulator (FD-SOI) MOSFET technology is projected to provide for significantly improved yield across a wide range of operating voltages, as compared with conventional planar bulk CMOS technology. Quasi-Planar (QP) bulk silicon MOSFETs are a lower-cost alternative and also can provide for improved SRAM yield. A more printable "notchless" QP bulk SRAM cell layout is proposed to reduce lithographic variations, and is projected to achieve six-sigma yield (required for terabit-scale SRAM arrays) with a minimum operating voltage below 1 Volt.

---

Professor Tsu-Jae King Liu, Chair  
Dissertation Committee Chair

To my parents for their unbounded love and support,  
to my brother for his sincere encouragement,  
and to my wife for her devoted love.

# Contents

<b>Table of Contents</b>	<b>ii</b>
<b>List of Figures</b>	<b>viii</b>
<b>List of Tables</b>	<b>x</b>
<b>Acknowledgements</b>	<b>xi</b>

## Table of Contents

<b>Chapter 1: Introduction</b>	<b>1</b>
1.1 Static Random Access Memory (SRAM)	1
1.1.1 SRAM Basics	1
1.1.2 Alternative SRAM Cell Architectures	3
1.1.3 Sources of $V_T$ Variation	5
1.1.3.1 Random Dopant Fluctuations (RDF)	6
1.1.3.2 Gate Length Fluctuations	7
1.1.3.3 Gate Work-Function Variation (WfV)	8
1.1.4 Approaches to Mitigating the Impact of $V_T$ Variation for SRAM	8

1.2 Advanced Transistor Designs for the 22nm Node and Beyond	9
1.2.1 Planar Silicon-on-Insulator (SOI) MOSFETs	9
1.2.1.1 Partially-depleted SOI (PD-SOI) MOSFET	9
1.2.1.2 fully-depleted SOI (FD-SOI) MOSFET	10
1.2.2 Multiple-Gate MOSFETs	12
1.2.2.1 Double-Gate FinFET and SOI Tri-Gate MOSFETs	12
1.2.2.2 Gate-All-Around (GAA) MOSFET	13
1.3 Research Objectives and Thesis Overview	14
1.4 References	15

## **Chapter 2: Performance and Area Scaling Benefits of FD-SOI Technology for 6-T SRAM Cells at the 22nm node** .....23

2.1 Introduction	23
2.2 Thin-BOX FD-SOI Technology	23
2.2.1 MOSFET Design Optimization	23
2.2.2 Impact of Random Variations	27
2.3 6-T SRAM Cell Performance Comparison	28
2.3.1 Nominal Cell Design	28



2.3.2 Dependency of SRAM Performance Metrics on Cell Ratio, Pull-Up Ratio, and $V_{DD}$	30
2.4 Yield-Aware SRAM Cell Design	31
2.4.1 Iso-Area Comparison	32
2.4.2 Iso-Yield Comparison	33
2.4.3 Minimum Operating Voltage ( $V_{min}$ ) for read and write operation	33
2.5 Summary	34
2.6 References	35
2.A Appendix	37

## **Chapter 3: Study of Random Dopant Fluctuation (RDF) Effects for the Quasi-Planar Bulk MOSFET** .....38

3.1 Introduction	38
3.2 Device Simulation Approach	39
3.2.1 Nominal Bulk MOSFET Designs	39
3.2.2 Methodology for Atomistic Device Simulation	39
3.3 Results and Discussion	42
3.3.1 Planar vs. Quasi-Planar Bulk MOSFET Designs	42
3.3.2 Body RDF vs. Source/Drain RDF	43

3.3.3 Assessment of $V_{TH}$ Adjustment Approaches	43
3.4 Summary	45
3.5 References	45

## **Chapter 4: Full three-dimensional Simulation of 6-T SRAM Cells for the 22nm node** .....47

4.1 Introduction	47
4.2 Segmented Bulk MOSFET Structure and Fabrication Process	49
4.3 6-T SRAM Cell Designs	49
4.4 Global and Local Variation Analysis	52
4.5 Simulation of Single-Event-Upset	53
4.6 Summary	55
4.7 References	55

## **Chapter 5: Quasi-Planar Bulk CMOS Technology for Improved SRAM Scalability** .....58

5.1 Introduction	58
5.2 Device Fabrication	59
5.3 Results and Discussion	61

5.3.1 Quasi-Planar vs. Planar MOSFETs .....	61
5.3.1.1 Improved Performance .....	61
5.3.1.2 Suppressed $V_{TH}$ Variation .....	62
5.3.1.3 Improved Short-Channel Effect .....	64
5.3.1.4 Increased Narrow Width Effect .....	65
5.3.1.5 Compact Transistor Model .....	65
5.3.1.4 Increased Narrow Width Effect .....	65
5.3.2 Benefits of Quasi-Planar Bulk CMOS Technology for 6-T SRAM .....	67
5.3.2.1 Cell Yield Enhancement .....	67
5.3.2.2 Supply-Voltage Reduction .....	67
5.3.1.2 Suppressed $V_{TH}$ Variation .....	62
5.4 Summary .....	68
5.5 References .....	69

## **Chapter 6: Performance and Yield Benefits of Quasi-Planar Bulk CMOS Technology for 6-T SRAM at the 22 nm Node .....71**

6.1 Introduction .....	71
6.2 Quasi-Planar Bulk Technology .....	73
6.2.1 Optimized MOSFET Performance .....	73

6.2.2 Impact of Random and Systematic Variations	75
6.3 Notchless 6-T SRAM Cell Designs	77
6.4 SRAM Yield Estimation	81
6.4.1 Iso-Area and Iso-Yield Comparisons between Planar and Quasi-Planar Bulk Cell Designs	81
6.4.2 Notchless Quasi-Planar Bulk SRAM Cell Yield	82
6.5 Summary	83
6.6 References	83
<b>Chapter 7: Conclusion</b>	<b>87</b>
7.1 Contribution of This Work	87
7.2 Suggested Future Work	90
A. Improved Manufacturability	91
B. Independent Biasing Transistors	92
C. Compatibility with Advanced Device Architecture	92
7.3 References	93

# List of Figures

1.1	Circuit schematic for a six-transistor (6-T) SRAM cell	2
1.2	Definition of the static noise margin and write-ability current	3
1.3	Alternative SRAM bit-cell architecture	4
1.4	Standard deviation of threshold voltage <i>vs.</i> channel length	5
1.5	Randomly distributed dopant atoms in an n-channel MOSFET	6
1.6	Illustration of a nano-scale MOSFET showing line-edge-roughness	7
1.7	Illustration of hypothetical metal gate film	8
1.8	Transmission electron micrograph image of a PD-SOI n-MOSFET with HK/MG	9
1.9	Product design compromises for planar bulk, PD-SOI, and FD-SOI	10
1.10	Experimental data for SOI layer thickness variation	11
1.11	FD-SOI technology features	12
1.12	Transmission electron micrograph image of FinFET structures	13
1.13	Transmission electron micrograph image of Omega-/Tri-gate MOSFET structures	13
1.14	Transmission electron micrograph image of twin silicon nanowire MOSFET	14
2.1a	Cross-sectional view of a thin-BOX FD-SOI MOSFET structure	24
2.1b	Experimental data for SOI thickness variation	25
2.2	Transfer characteristics of planar bulk and FD-SOI MOSFETs	26
2.3	Simulated I-V curves of pull-down transistor for LER/RDF	26
2.4	Comparisons of SNM and write current	29
2.5	Comparison of SRAM cell performance metrics	30
2.6	Impact of $V_{DD}$ scaling on 6-T SRAM cell performance metrics	31
2.7	Yield of $I_w$ <i>vs.</i> Yield of SNM for FD-SOI and planar bulk	32
2.8	Yield of $I_w$ <i>vs.</i> Yield of SNM for FD-SOI and enlarged planar bulk	33
2.9	Dependence of yield on $V_{DD}$	34
3.1	3D bird-eye view and cross-sectional view of the quasi-planar bulk MOSFET	39
3.2	Example of a QP bulk MOSFET with atomistic doping profiles and isometric view	40
3.3	Simulated I-V curves for planar and QP bulk MOSFETs with atomistic doping	41
3.4	Comparison of body RDF <i>vs.</i> source/drain RDF effects	43
3.5	Impact of nominal $V_{TH}$ adjustment on $V_{TH}$ variation	44
4.1a	Cross-sectional views of a two-striped SegFET	48
4.1b	Front-end-of-line fabrication process steps for a SegFET	48

4.2	6T-SRAM cell area scaling trend	49
4.3	3D 6-T SRAM cells simulation results	50
4.4	3D 6T-SRAM cell structures with fine meshing	51
4.5	SNM and $I_w$ vs. $V_{DD}$	52
4.6	SegFET vs. planar MOSFET comparison	53
4.7	Heavy ion beam modeling	54
4.8	Transient simulations of heavy-ion-beam strike on the high storage node	54
5.1	Sequence of front-end-of-line CMOS fabrication process steps for QP MOSFET	60
5.2a	0.149 $\mu\text{m}^2$ SRAM cell plan-view CDSEM image after gate patterning	60
5.2b	XTEM taken along a poly-Si gate electrode in an SRAM array	60
5.3	Comparison of ON/OFF current statistics for planar vs. QP MOSFETs	61-62
5.4	Comparison of saturation $V_{TH}$ statistics for planar vs. QP MOSFETs	63
5.5	Pelgrom plots for NMOS and PMOS logic devices	64
5.6	Saturation threshold voltage with decreasing gate length	64
5.7	Measured reverse narrow width effect for devices with 36nm gate length	65
5.8	Comparison of measured and modeled output characteristics	66
5.9	Sigma and 3-sigma/median values for SNM and WRM	67
5.10	Degradation in 3-sigma/median for SNM and WRM	68
6.1	Bird-eye view of a quasi-planar bulk MOSFET and along/across the channel	72
6.2	Simulated transfer characteristics for planar and quasi-planar bulk MOSFETs	73
6.3	Simulated $V_{TH,SAT}$ for planar bulk vs. quasi-planar bulk MOSFETs	76
6.4	Half-bit cell layouts for notched and notchless SRAM cell designs	78
6.5	3-D 6-T SRAM cell simulation results	79
6.6a	SRAM cell read current	80
6.6b	PD device gate capacitance	80
6.6c	Pseudo-transient simulation of the storage-node voltage during a write operation	80
6.7	SRAM cell sigma comparisons for SNM and $I_w$	82
6.8	SRAM cell sigma comparisons for SNM and $I_w$	82
7.1a	Proposed new layout of the 6-T SRAM bit-cell	91
7.1b	Circuit schematic of the 6-T SRAM bit-cell with external voltage skews	91
7.2	Conventional layout of a 6-T SRAM bit-cell	92

# List of Tables

2.1	Optimized thin-BOX FD-SOI and Planar bulk MOSFET design parameters	25
2.2	Comparison of device performance parameters for $V_{DD} = 0.9$ V	26
2.3	FD-SOI 6-T SRAM cell dimensions	29
2.4	Summary of SRAM cell performance metrics	34
4.1	SegFET 6T-SRAM cell dimensions for the 22nm node	50
6.1	Summary of transistor performance parameters	74
6.2	22nm-node 6-T SRAM cell layout parameters	79
6.3	Comparison of projected performance metrics and cell areas	81
7.1	Comparison of three different device architectures	90

# Acknowledgements

During my time at Berkeley, lots of people have sincerely guided my research. I would like to begin by appreciating all of their kind help.

In fact, I could not write this page without expressing my deepest thanks to my academic advisor, Professor Tsu-Jae King Liu, who is the epitome of a great mentor and guided me from unsure beginning as a fresh researcher to the bleeding-edge in my field of study. She has always been cordial, attentive, available and supportive throughout all the peaks and valleys of my Ph.D. course. In all research meeting, she never failed to advise me with her inspiring perspective, amazing engineering-intuition, tireless enthusiasm, and firm and solid knowledge. There is much about her management style that I would like to bring with me as I go into industry and/or academia.

I am grateful for all the support and advice of Professor Borivoje Nikolić, chairing my qualifying examination and serving as a member of my dissertation committee. His keen perspective on SRAM was exceptionally helpful, and his sincere advice on leading my research opportunities toward a very meaningful contribution to device and circuit co-optimization was tremendously valuable.

I also thank Professor Eugene E. Haller for serving on both my qualifying examination committee and my dissertation committee, and thank Professor Sayeef Salahuddin for serving my qualifying examination committee.

Dr. Yasumasa Tsukamoto, former visiting scholar, provided invaluable guidance on SRAM designs, for which I am greatly grateful. His firm and rigorous SRAM knowledge has provided a great advantage toward understanding SRAM and all its tradeoffs. His experience in industry was also helpful for my research and future career. I hope to be as informative and impactful with my future colleagues as he is with his.

Dr. Si-woo Lee, another former visiting scholar, became my wise counselor for both my research and life. While he was staying at Berkeley, I learned something new from him every day.

I would like to thank several former and current students with regards to this work. With Dr. Andrew Carlson, Dr. Xin Sun, Min Hee Cho, and Nattapol Damrongplasit, I could establish the foundation of my research. They provided kind assistance and several helpful discussions on SRAM, advanced device structures, and their variability. With Dr. Zheng Guo, Seng Oon Toh, Aikaterini Papadopoulou, and Jaehwa Kwak, I had a lot of discussions on SRAM in test chips. They also kindly assisted with the logistics of tapeout and testing.



In addition to the above, several others have provided indirect assistance. Dr. Donovan Lee and Dr. Joanna Lai helped me, among many other things, to acquire an American English language and to adapt myself to new circumstances at Berkeley. Jemin Park and Kanghoon Jeon sincerely helped me in times of need. Prof. Man Young Sung, Prof. Suki Kim, Prof. Soo-Won Kim, Prof. Tae-Geun Kim, Prof. Sang Bin Lee, Prof. Jae-Sung Rieh, Prof. Tae-Woong Yoon, Prof. James Jungho Pak, Prof. Woo-Young Choi, Prof. Songhwai Oh, Prof. Hyuck Choo, Dr. Vidya Varadarajan, Dr. Alvaro Padilla, Dr. Reinaldo Vega, Dr. Hei Kam, Dr. Louis Hutin, Dr. Jiwoong Lee, Dr. Daekyeong Moon, Dr. Jaemin Jeong, Dr. Chuck Choongyeun Cho, Dr. Kihoon Kim, Dr. Gregory Freeman, Dr. Dae-kyu Park, Jason Cheng, Rhesa Nathanael, Zachery Jacobson, Wookhyun Kwon, Jaeseok “Jay” Jeon, Sung Hwan Kim, Byron Ho, Nuo Xu, Peter Matheu, Eung Seok Park, I-Ru “Tim” Chen, Yenhao “Philip” Chen, Jack Yaung, Sriramkumar V., Darsen D. Lu, Stan Baek, Ji-Hoon Park, Namseog Kim, Jung-Dong Park, Kwangmo Jung, Tae Joon Seok, Se Yong Park, Changho Suh, Kyoo Hyun Noh, Sunyoung Lee, Hyojin Kim, Hyerin Lee, Kangwook Lee, Sangyoon Han, Youngki Yoon, Shinwon Kang, Hongki Kang, Jaewon Jang, Chang-Seo Park, Yunsup Lee, Hyun Oh Song have also provided technical, educational, personal assistance in some form. I appreciate all of their help.

This work has been funded through a few sources. First of all, my financial stability for my Ph.D. work came from the Korea Foundation of Advanced Studies (KFAS) Fellowship. This work was also supported in part by the Center for Circuit & System Solutions (C2S2) Focus Center, which is one of five research centers funded under the Focus Center Research Program (a Semiconductor Research Corporation program). In addition, fabrication of a 28nm test chip for studying 28nm quasi-planar bulk technology and data for FD-SOI wafer was donated by UMC (Dr. Cheng-Tzung Tsai and all the other UMC engineers involved to the 28nm test chip) and Soitec (especially, Dr. Carlos Mazuré and Mrs. Bich-Yen Nguyen), respectively. I would like to express my sincere gratitude for the financial and technical supports, and I will not forget to contribute back to them in future.

Finally, I would not be here today were it not for my family. I can not thank my parents and my younger brother enough for their unbounded love and sacrifices. Their love will always hold a special place in my heart. Lastly, but most certainly not least, I would like to thank my wife, Yun Jeong Hwang, for her devoted love. She is my light at the end of the long tunnel, and I appreciate her.

# Chapter 1

## Introduction

Improvement in integrated circuit (IC) performance and cost has been achieved largely by transistor scaling (*i.e.*, minimum feature size reduction by a factor of 0.7 in every new technology node, or every 2 years) according to Moore's Law [1, 2]. The resultant exponential growth in device count per chip has been led by the miniaturization of the static-random-access-memory (SRAM) bit-cell. Increasing process-induced variations in transistor performance with miniaturization down to the 22 nm technology node and beyond is a major technical challenge for continued advancement of planar-bulk/partially-depleted silicon-on-insulator (PD-SOI) complementary metal-oxide-semiconductor (CMOS) technology [3, 4]. In particular, continued SRAM cell-area scaling for increased storage density, reduction in operating voltage ( $V_{DD}$ ) for lower stand-by power consumption, and enhanced yield necessary to realize larger-capacity SRAM arrays (*i.e.*, embedded level-2 or level-3 cache memory for microprocessor) become increasingly difficult to achieve. This thesis explores the benefits of advanced transistor structures and bit-cell design co-optimization for continued SRAM scaling.

### 1.1 Static Random Access Memory (SRAM)

#### 1.1.1 SRAM Basics

The SRAM cell incorporates a static latch, comprising two cross-coupled inverters, so that it does not require *periodic refreshing* to retain the stored information, provided that there is adequate power supply voltage for the cell ( $V_{DD,cell}$ ).

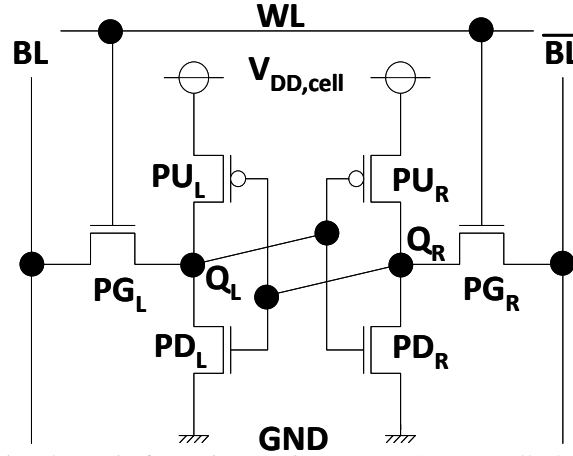


Figure 1.1. Circuit schematic for a six-transistor (6-T) SRAM cell, the most commonly used SRAM bit-cell architecture.

**Fig. 1.1** shows the most commonly used SRAM bit-cell architecture, that is the six-transistor (6-T) SRAM cell. It consists of two cross-coupled inverters (PMOS pull-up transistors  $PU_L$  and  $PU_R$  and NMOS pull-down transistors  $PD_L$  and  $PD_R$ ) and two access transistors (NMOS pass-gate transistors  $PG_L$  and  $PG_R$ ). When the horizontally-running word-line (WL) is enabled (*i.e.*, a row is selected in an array), the access transistors are turned on, and connect the storage nodes to the vertically-running bit-lines (BL and  $\overline{BL}$ ). In other words, they allow access to the cell for read and write operations, acting as bi-directional transmission gates.

The 6-T SRAM cell operates as follows: **(1) For a read operation**, the bit-lines are usually *pre-charged* to a high level ( $V_{DD}$ ) and then the word-line is selected (pulsed to a high level). On the side of the cell storing a logical ‘0’ (*i.e.*, a low voltage), the bit-line is discharged via the pass-gate transistor and pull-down transistor, so that a differential voltage develops between the bit-lines. This differential voltage should be large enough for a sense amplifier to detect the state of the cell. The differential voltage should not be too large, however; otherwise the cross-coupled inverters could flip their state. (The read operation should be *non-destructive*.) The cell *beta ratio*, which is the ratio of the strength (drive current) of the pull-down transistor to that of the pass-gate transistor, should be sufficiently large to ensure that such a *read disturbance* does not occur. **(2) For a write operation**, the bit-lines are driven to complementary voltage levels via a write driver and then the word-line is selected. On the side of the cell for which the bit-line voltage is logical ‘0’ (*i.e.*, a low voltage), the internal storage node is discharged through the pass-gate transistor. The cross-coupled inverters raise the voltage on the opposite storage node and latch the cell. The discharging strength of the pass-gate transistor must overcome the restoring strength of the pull-up transistor. The cell *gamma ratio*, which is the ratio of the strength of the pass-gate transistor to that of the pull-up transistor, should be sufficiently large to ensure that *write failure* does not occur.

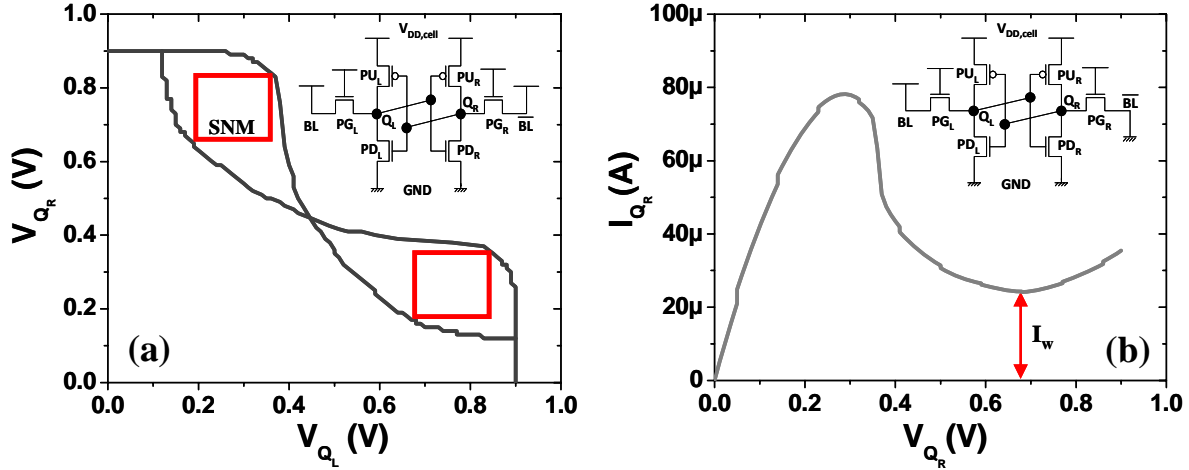


Figure 1.2. (a) Definition of the static noise margin (SNM) from the read voltage transfer characteristics (VTC), or “butterfly curves” for a 6-T SRAM cell. The inset shows the biasing conditions for read operation. (b) Definition of the write-ability current from the write “N-curve.” The inset shows the biasing conditions for write operation. Note that the storage node  $Q_L$  is at logical ‘0’ voltage level.

Since Seevinck’s seminal work [5] in 1987, the most common metric for SRAM read stability is the read static noise margin (SNM), illustrated in **Fig. 1.2(a)**. SNM is the maximum tolerable DC noise voltage at a storage node that does not cause a read disturbance, and it is the length of the side of the largest square that can fit into the “eyes” of the butterfly curves, *i.e.*, the read voltage transfer characteristics (VTC), for the SRAM cell. The other metric for read stability utilizes the read N-curve [6, 7], which is measured by sweeping the voltage at the storage node  $Q_L$  (or  $Q_R$ ) via the bit-line, with the word-line and two bit-lines biased at  $V_{DD}$ , and monitoring the current sourced into the storage node.

The write N-curve illustrated in **Fig. 1.2(b)** is obtained by sweeping the voltage at the storage node  $Q_R$  ( $Q_L$ ), with  $BL$  ( $BL$ ) and  $WL$  biased at  $V_{DD}$  and  $BL$  ( $BL$ ) biased at  $GND$ , and monitoring the current sourced into the storage node. The write-ability current [8, 9],  $I_w$ , is defined as the minimum current past the inverter  $PU_L$ - $PD_L$  trip point, and is a measure of the difference between  $PG_R$  and  $PU_R$  currents.

### 1.1.2 Alternative SRAM Cell Architectures

As explained in the previous section, the transistors within a 6-T SRAM cell must be sized properly (since drive current is proportional to transistor width) for the cell to meet both read and write margin specifications to guarantee proper operation. There is a fundamental tradeoff, therefore, between cell yield and cell layout area (*i.e.*, cost). This tradeoff is worsened by the need to include design margin for process-induced variations in transistor threshold voltage ( $V_T$ ) since drive current is a function of  $V_{DD} - V_T$ .

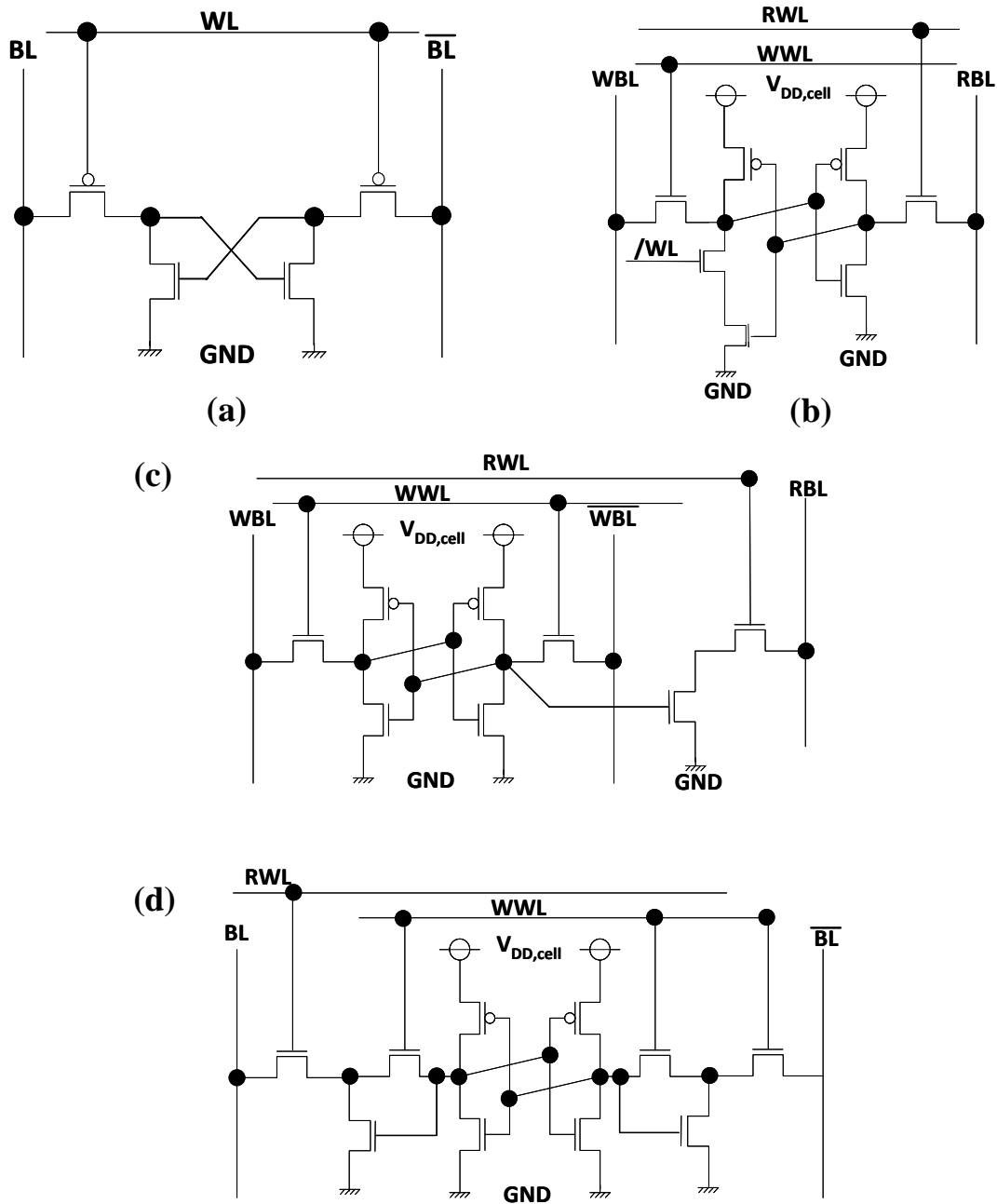


Figure 1.3. Alternative SRAM bit-cell architectures: (a) 4-T SRAM cell, (b) 7-T SRAM cell, (c) 8-T SRAM cell, and (d) 10-T SRAM cell.

Various alternative SRAM bit-cell architectures have been proposed to reduce cell area or to decouple the requirements for read stability and write-ability. The 4-T SRAM cell (**Fig. 1.3(a)**) consists of two PMOS pass-gate transistors and two NMOS pull-down transistors, resulting in relatively smaller cell area than the 6-T SRAM design [10-15]. It

maintains a logical ‘1’ state at one of the internal storage nodes via PMOS transistor off-state leakage current. This results not only in higher static power consumption but also in larger susceptibility to  $V_T$  variation (since transistor off-state leakage current varies exponentially with  $V_T$ ), so that the 4-T SRAM cell architecture is not promising for sub-22 nm SRAM technologies. The 7-T SRAM cell (**Fig. 1.3(b)**) [16] utilizes dedicated word-lines and bit-lines for read *vs.* write operations to avoid the possibility of a read disturbance even if the read SNM is lower than 0, so that minimum-width transistors can be used for minimal cell area. Takeda et al. [17] demonstrated 23% area-savings for a layout-optimized 7-T SRAM array (*vs.* a 6-T SRAM array), for the same operating speed. However, it has complexity in layout. The 8-T SRAM cell (**Fig. 1.3(c)**) [18-21] also utilizes dedicated word-lines and bit-lines for read *vs.* write operations, but uses complementary bit-lines for write operation as does a 6-T SRAM cell. Write disturbance is still a general issue for these alternative cell architectures. The 10-T SRAM cell (**Fig. 1.3(d)**) [22] decouples the storage nodes from the bit-lines to improve read stability, but requires the use of peripheral write-assist circuitry. These alternative SRAM cell architectures each have undesirable tradeoffs in cell area or performance as compared to the 6-T SRAM cell. This thesis therefore focuses on technological approaches to improve the scalability of the 6-T SRAM cell.

### 1.1.3 Sources of $V_T$ Variation

$V_T$  variation is caused by two types of sources: systematic and random. Systematic sources include lithography-induced variations in channel length and width, which are deterministic and predictable. Random sources include as gate line-edge-roughness (LER), random-dopant-fluctuation (RDF), and gate work-function variation (WFV), which are non-deterministic and are projected to be the dominant sources of  $V_T$  variation for transistors with channel length below 30 nm, as shown in **Fig. 1.4** [23].

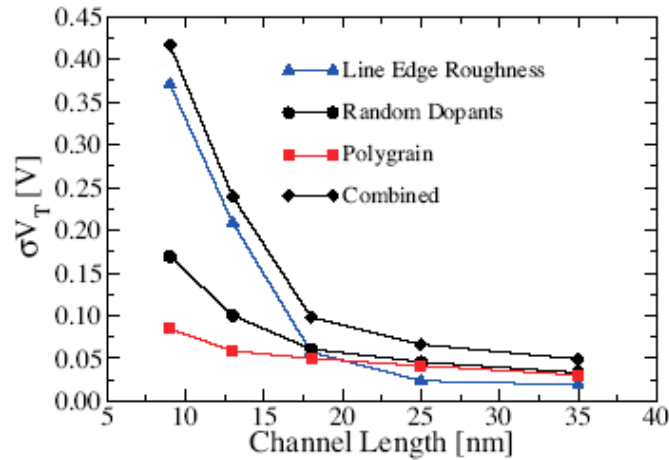


Figure 1.4. Standard deviation of threshold voltage variation *vs.* channel length, for square planar bulk MOSFETs. Constant gate line edge roughness (4 nm) is assumed [23].

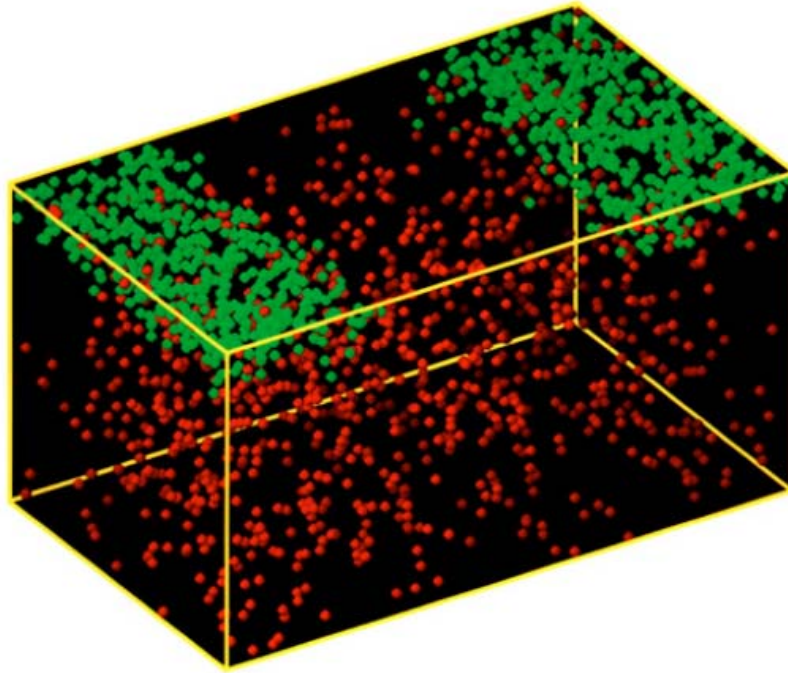


Figure 1.5. Randomly distributed dopant atoms in an n-channel MOSFET with channel length of 30 nm and channel width of 50 nm [24]. (Green-colored atoms are donors and red-colored atoms are acceptors.)

### 1.1.3.1 Random Dopant Fluctuations (RDF)

In the early 1970s, Keyes explored the effects of random fluctuation in the number of impurity atoms [25], as one of the issues for continued transistor scaling. Experiments confirmed his theory, for a wide range of fabricated devices [26]. Analytical models [3] and three-dimensional (3D) fine-grid statistical device simulations [27, 28] were subsequently used to understand and predict RDF-induced  $V_T$  variation in deep sub-micron devices. It is well known that RDF-induced  $V_T$  is inversely proportional to  $(W \times L)^{0.5}$ , where  $W$  and  $L$  are the transistor channel width and length, respectively. Recently, in a 100,000-sample 3D simulation study [29], the complete  $V_T$  distribution caused by RDF was constructed through the discrete convolution of a Poisson distribution with the mean ( $N$ ) of the number of dopants in channel region, and a Gaussian distribution of  $V_T$  for a fixed  $N$ . As the channel doping and/or halo doping in conventional Planar-bulk/PD-SOI MOSFETs is increased with scaling to suppress short-channel effects, RDF-induced variation will worsen. The use of a lightly doped (fully depleted) SOI MOSFET structure with a thin ( $\sim 10$  nm-thick) buried oxide (BOX) and a heavily doped substrate has been reported to be effective for suppressing this variation [30].

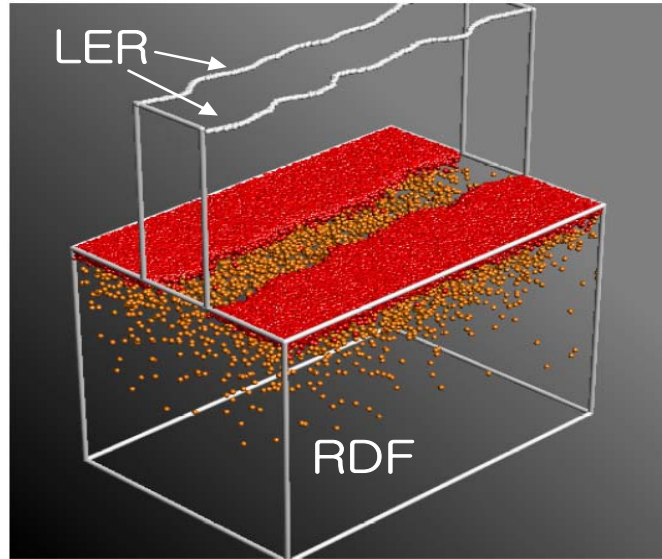


Figure 1.6. Illustration of a nano-scale MOSFET showing gate line-edge-roughness across the width of the transistor, with randomly placed dopants in the source/drain and channel regions [31].

### 1.1.3.2 Gate Length Fluctuations

Polymer erosion at the edges of a photoresist line during the development process has been shown to create a rough profile [32, 33]. As a result, a lithographically patterned gate electrode exhibits line edge roughness (LER) across the width of the transistor, as shown in **Fig. 1.6**. Gate LER is not only dependent on the photoresist material and coat and develop process conditions, but also on the gate material microstructure and etch process conditions. As shown in **Fig. 1.4**, LER can become the dominant source of random  $V_T$  variation for gate lengths below 20 nm, if it does not scale down with the transistor minimum dimension. Spacer gate lithography [34, 35] can suppress LER-induced variation in transistor performance, and is effective even if LER does not scale because the LER for the “outer edges” of the spacers will be strongly correlated with that of the “inner edges”.

In addition to LER, proximity effects can affect the width of a developed photoresist feature. Diffraction effects limit the resolution of modern optical projection lithography systems: higher-order diffraction components are lost due primarily to the finite size of the focusing lens, resulting in a loss of fidelity in the printed image manifest as corner rounding. The use of a lens with higher NA (Numerical Aperture) results in a higher fidelity image.



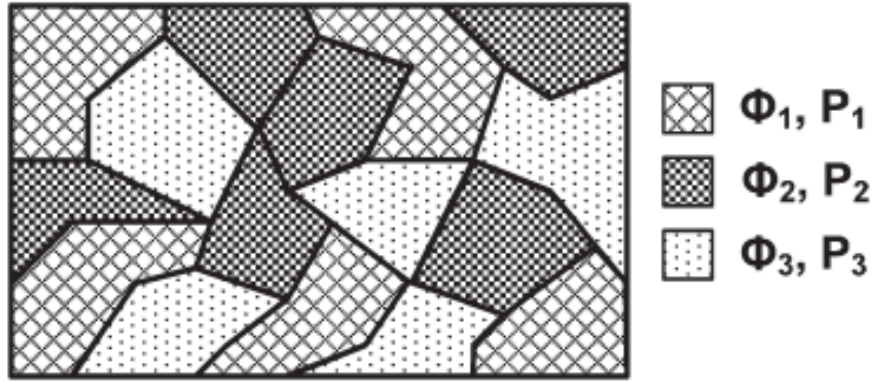


Figure 1.7. Illustration of a hypothetical metal gate film comprising grains of three different orientations and hence three different work-function values ( $\Phi_1 \sim \Phi_3$ ), each orientation having a certain occurrence probability ( $P_1 \sim P_3$ ) [36].

### 1.1.3.3 Gate Work-Function Variation (WfV)

Beginning at the 45 nm generation of CMOS technology, advanced gate stack materials *i.e.*, high-permittivity gate dielectric and metal gate (HK/MG), have been used to reduce the effective gate-oxide thickness and thereby improve the electrostatic integrity of nano-scale transistors. As illustrated in **Fig. 1.7**, a metal film typically comprises microcrystalline grains of various orientations, each with an associate work function (WF). The random distribution of grains within a metal gate film results in a probabilistic distribution of WF values. WfV can become a significant source of random  $V_T$  variation in future transistors with nano-scale gate length. Dadgour [36, 37] highlighted and experimentally verified this source of random  $V_T$  fluctuation in HK/MG transistors and proposed a statistical framework to investigate device- and circuit-level implications.

### 1.1.4 Approaches to Mitigating the Impact of $V_T$ Variation for SRAM

Random  $V_T$  variation presents a serious challenge for scaling SRAM cell area and operating voltage to the 22 nm technology node and beyond. Circuit-design approaches to address this challenge include read-assist and write-assist techniques which enhance SRAM read and write margins, respectively. Examples of these include read/write-assist column circuitry, word-line bias, pulsed bit lines, lower column supply voltages during write, and negative voltage on bit-line [38, 39]. These techniques inevitably result in lower array area efficiency. A complementary approach is to improve the robustness of the transistor design

to process-induced  $V_T$  variation. In the following section, various advanced transistor designs are introduced.

## 1.2 Advanced Transistor Designs for the 22 nm Node and Beyond

New technologies have been introduced to enable continued scaling of the planar bulk MOSFET structure beyond the 130 nm technology node. These include HK/MG gate stacks [40, 41] and channel stress technology (*e.g.*, strained-silicon substrate [42], embedded- $\text{Si}_{1-x}\text{Ge}_x$  ( $\text{Si}_{1-x}\text{C}_x$ ) for p-channel (n-channel) MOSFETs [43], and raised source/drain [44]). Since the planar bulk MOSFET requires a heavily doped channel region and/or halo doping to suppress DIBL (Drain Induced Barrier Lowering) and the short-channel effect ( $V_T$  reduction with decreasing gate length), it inevitably suffers RDF effects. To avoid the use of heavy channel doping, thin body (fully depleted) and multi-gate transistor structures have been investigated in recent years.

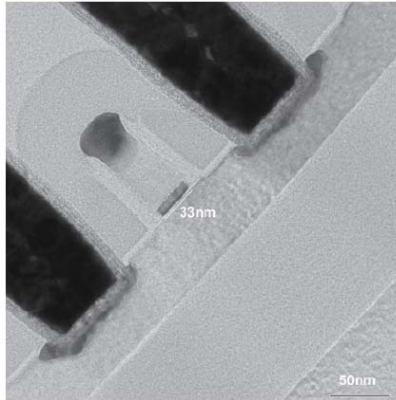


Figure 1.8. Transmission electron micrograph image of a partially depleted silicon-on-insulator (SOI) n-channel MOSFET with HK/MG stack. The channel length is 33 nm [45].

### 1.2.1 Planar Silicon-on-Insulator (SOI) MOSFETs

#### 1.2.1.1 Partially-depleted SOI (PD-SOI) MOSFET

Partially depleted silicon-on-insulator (PD-SOI) transistors (**Fig. 1.8**) [45, 46] are used for high-performance applications because they have significantly reduced junction capacitances (the buried oxide (BOX) layer is typically  $>100$  nm thick) and hence increased circuit operating speed compared to bulk silicon MOSFETs. However, PD-SOI MOSFETs suffer from the “floating-body” effect [47]: if the body region is not tied to a bias voltage, then majority carriers generated by impact ionization (when the transistor is in the on state)

accumulate in the body region and forward-bias the source junction, effectively lowering  $V_T$ . This results in an increase in on-state current that is dependent on the transistor operating history [48, 49]. In addition, like the planar bulk MOSFET, a PD-SOI MOSFET still requires a heavily doped channel region and/or halo doping to reduce DIBL and  $V_T$  roll-off, and thus inevitably suffers from RDF effects which limit its scalability.

### 1.2.1.2 Fully-depleted SOI (FD-SOI) MOSFET

Increasing variability in transistor and circuit performance for planar bulk and/or PD-SOI CMOS technology requires more complex chip design, and hence results in non-optimal product design (**Fig. 1.9(a)**) [50]. Rather than doping the channel heavily to suppress off-state leakage, it can be made to be very thin to eliminate sub-surface leakage paths and reduce DIBL [51]. In the latter case, the channel/body region is so thin (with a thickness that is less than one fourth of the transistor channel length) that it is fully depleted of mobile charge carriers when the transistor is in the off state. Such a fully depleted MOSFET structure is most easily implemented with an extremely-thin SOI substrate [52]. The floating-body effect is negligible in an FD-SOI MOSFET because there is no quasi-neutral body region which serves as a potential well to hold majority carriers [53]. Also, RDF-induced  $V_T$  variation can be dramatically lower in a FD-SOI MOSFET since light channel/body doping can be used [54]. FD-SOI technology compares well against planar bulk technology across key figures of merit (**Fig. 1.9(b)**). The same chip design flow can be used for FD-SOI technology as for planar bulk technology, which is advantageous for reduced design cost and time-to-market [54].

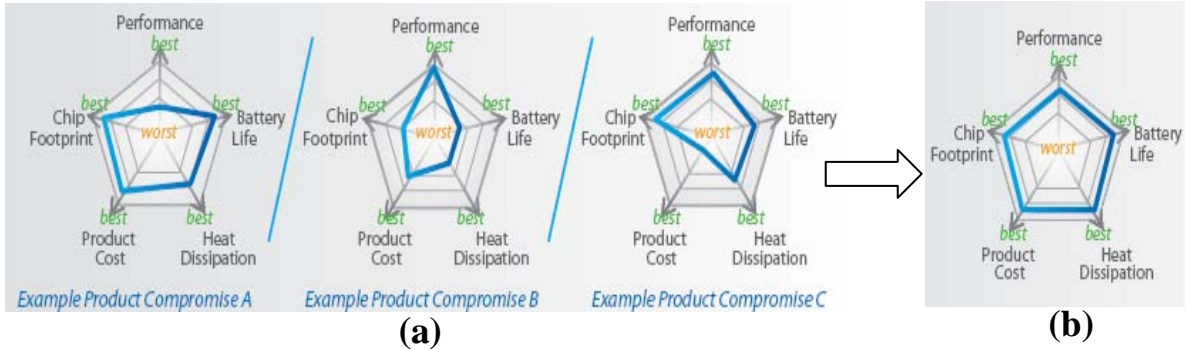


Figure 1.9. (a) There are product design compromises for planar bulk and/or PD-SOI CMOS technology. (b) FD-SOI technology is superior across all figures of merit [50].

FD-SOI technology faces a number of challenges for widespread adoption. First is the need for uniformly thin Si films. For gate lengths ( $L_g$ ) below 15 nm, the Si thickness ( $T_{si}$ ) should be less than 4 nm [52] in order to control short channel effect (*i.e.*,  $T_{si}$  should be less than a quarter of physical gate length). In this thickness range, quantum confinement effects (which cause  $V_T$  to increase geometrically with decreasing  $T_{si}$ ) make  $V_T$  very sensitive to variations in  $T_{si}$  [55]. Second is parasitic resistance associated with ultra-thin

source/drain regions. By thickening the source/drain regions via selective epitaxial growth, this resistance can be reduced, but at the cost of increased gate-to-source/drain capacitance [56]. Metallic source/drain regions can be used [57], but then a very low Schottky barrier technology would be needed. Third is the need for thin-BOX substrates to allow for  $V_T$  tuning via sub-BOX doping and/or dynamic  $V_T$  control via back-biasing [58], which come at the cost of increased source/drain junction capacitance. Recent progress in the manufacture of SOI substrates with uniformly ultra-thin Si ( $T_{si} \sim 10$  nm) and thin BOX ( $T_{BOX} \sim 25$  nm or less) has enabled successful demonstrations of nano-scale FD-SOI devices [59]. **Fig. 1.10** shows measured  $T_{si}$  variation across a wafer and across many wafer batches. The SOI Consortium is now promoting FD-SOI technology as a solution that can meet requirements for mobile applications with regard to power consumption, performance, manufacturability, scalability, and cost efficiency (**Fig. 1.11**).

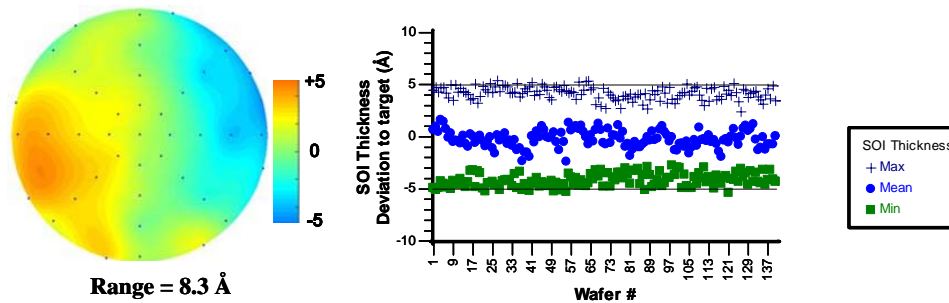


Figure 1.10. Experimental data (courtesy of Soitec) for SOI layer thickness ( $T_{si}$ ) variation across a wafer (left) and from wafer to wafer (right). The peak-to-peak variation is less than 1 nm [59].

<b>Mobile Consumer Equipment</b>	Great Apps, Faster Web Browsing, Dazzling Multimedia, Fantastic User Interfaces ...without draining the battery		
	Avoiding system over-heat	Cost-optimized for Consumer Market	Longer usage time
<b>System</b>	Superior "Power - Performance - Area - Cost - Time to Market" balance, across all use cases		
<b>Design</b>	Low SRAM $VDD_{min}$ (Low Power operation/retention); Dense and Stable SRAM with 7-sigma yield	Less design guard-bands required Easier Timing Closure	
	Superior Analog Behavior	Opportunities of enhanced efficiency for SoC Design Techniques : Voltage Scaling (DVFS), Retention Modes, Back-bias etc.	
	High Peak Performance Remarkable Performance at lower Vdd	Flexibility to exploit new operating points	
	Area efficiency	Essentially unchanged design flows, tools and methodologies	
	Intrinsically low leakage		
	Good receptivity to back-bias		
<b>Silicon Technology</b>	Excellent transistor $V_T$ variability and matching	No 'Floating Body' or other SOI-specific effect	
	Excellent electrostatic and electrical behavior of transistors (DIBL, Subthreshold slope, GIDL, junction leakage) even in very small geometries	Co-integration of traditional bulk CMOS legacy + FD-SOI on same chip possible	
	Same fab equipment	Simpler process	
<b>Technology Fundamentals</b>	Extremely uniform Ultra-Thin SOI starting wafers available for high volume manufacturing	<ul style="list-style-type: none"> <li>• Ultra-Thin Body Transistor Geometry</li> <li>• Undoped Channel</li> <li>• Ultra-thin Buried Oxide</li> </ul>	Planar CMOS approach with no unconventional process steps

Figure 1.11. FD-SOI technology features lead to benefits for mobile products [50].

## 1.2.2 Multiple-Gate MOSFETs

### 1.2.2.1 Double-Gate FinFET and SOI Tri-Gate MOSFETs

The fundamental concept behind a multiple-gate MOSFET (in which the gates are all tied together) is to increase gate control (vs. drain control) of the channel potential, particularly the source-to-channel potential barrier. The double-gate MOSFET has two gates located on opposing sides of the Si channel/body region, to control the channel potential. It is most easily implemented as a vertical structure, with a single gate electrode running across (straddling the two opposing sides of) a tall and narrow Si channel/body “fin.” This “FinFET” structure has been widely investigated [60-64], and can be implemented either on an SOI substrate [65] or a bulk-Si substrate [66] (**Fig. 1.12**).

To adequately suppress short-channel effects, the width of the Si fin in a FinFET should be uniformly less than one half of the channel length. For good layout area efficiency, the height of the Si fin should be tall [67] ( $>3\times$  its width). The formation of tall and uniformly narrow Si fins presents significant manufacturing challenges, not only for lithography and etch processes but also for doping processes. High-tilt-angle ion implantation or plasma doping or solid-source diffusion are necessary to dope the source/drain regions. For bulk-Si FinFETs, the need for steep retrograde “channel-stop” doping at the bases of the tall fin channel/body regions presents a significant processing challenge.  $V_T$  control is another manufacturing challenge for FinFET technology. For low-power (high  $V_T$ ) applications, a single gate material with work function corresponding to a Fermi level near the middle of the Si energy bandgap can be used. To achieve lower values of  $V_T$ , tuning of the gate work function, or the use of different gate materials, is required [68]. (Alternatively, precise reduction in electrical channel length can be used [69].) Dynamic  $V_T$  control requires physical separation and independent biasing of the front and back gates, which comes at the cost of added process complexity and layout area [70]. A design challenge for FinFET technology is the fact that transistor strength is adjusted not by changing the Si width but by changing the number of fins [60]. Thus, adaptations in automated design tools and cell libraries will be necessary for FinFET technology to be used for general purpose logic applications. For these reasons, the adoption of FinFET technology has been delayed. It is anticipated that FinFETs will be first used only in SRAM arrays where low leakage is imperative.

To mitigate the need for ultra-narrow Si fins, gating of additional channel surfaces as in the omega-gate [71, 72] and tri-gate SOI MOSFET [73] structures have been proposed (**Fig. 1.13**). These structures still face the same challenges of  $V_T$  control and design flow adaptation as the FinFET, however.



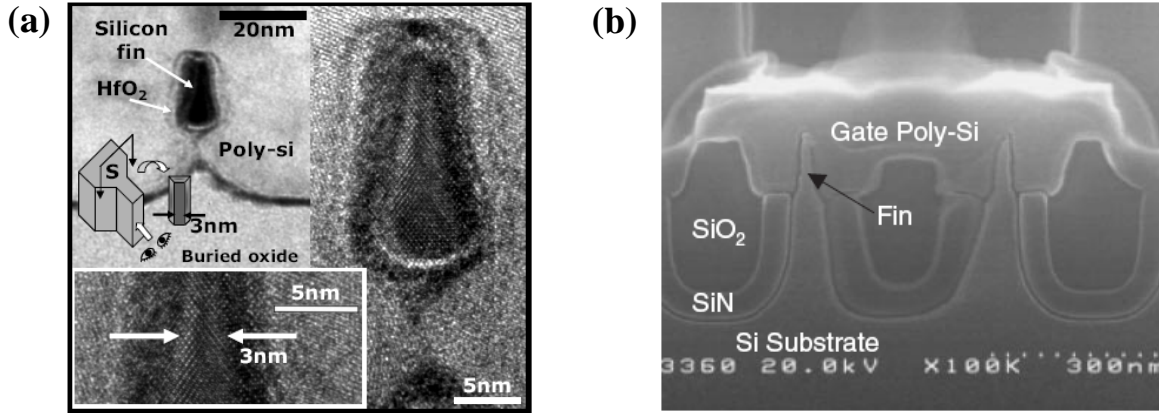


Figure 1.12. Transmission electron microscopy images of FinFET structures: (a) sub-5 nm gate length SOI FinFET with 3 nm-width fin and 1.4 nm-thick  $\text{HfO}_2$  gate dielectric. A blurry boundary delineates the source extension region [65]. (b) Bulk-Si FinFET after gate patterning and contact opening [66].

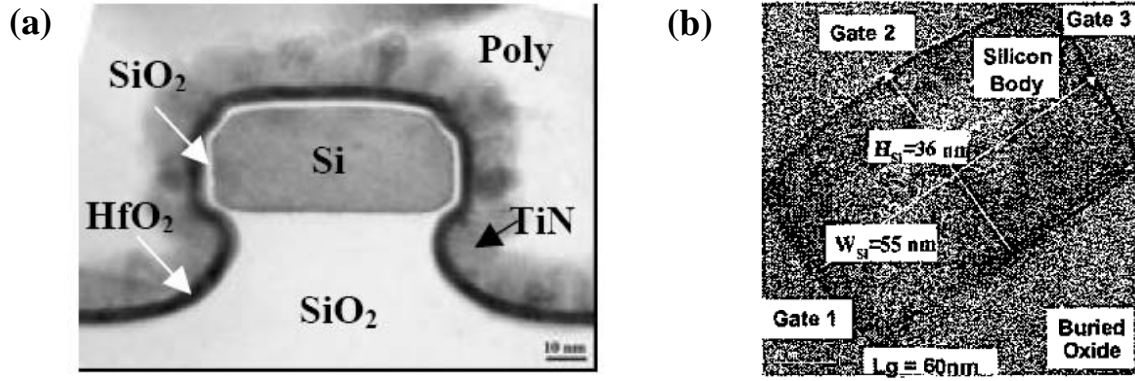


Figure 1.13. Transmission electron microscopy images of (a) Omega-gate FET with a 60 nm-wide channel/body and TiN/HfO<sub>2</sub> gate stack [72], (b) Tri-Gate SOI MOSFET [73].

### 1.2.2.2 Gate-All-Around (GAA) MOSFET

The best possible gate control is achieved by gating all of the channel surfaces, as in a Gate-All-Around (GAA) MOSFET. Thus, the most scalable transistor design is a nanowire MOSFET. As shown in **Fig. 1.14**, Suk et al. [74, 75] fabricated a GAA twin silicon nanowire MOSFET (TSNWFET) with 5-nm-radius, 30-nm-long channels on a bulk silicon wafer. N- and p-channel drive currents are 2.37 mA/ $\mu\text{m}$  and 1.30 mA/ $\mu\text{m}$  for off-state currents of 6.2 nA/ $\mu\text{m}$  and 6.7 pA/ $\mu\text{m}$  at  $V_{\text{DD}} = 1$  V, respectively. (A mid-gap gate work function is needed to achieve symmetric NMOS and PMOS  $V_{\text{T}}$  values.) Excellent gate control is evidenced by low sub-threshold swing ( $<70$  mV/dec) and DIBL  $< 25$  mV/V. The

major disadvantages of the GAA MOSFET are that it is difficult to manufacture with high precision, and that the current flow per nanowire is relatively low. Therefore, GAA MOSFETs are unlikely to be adopted for large-scale manufacturing in the near future.

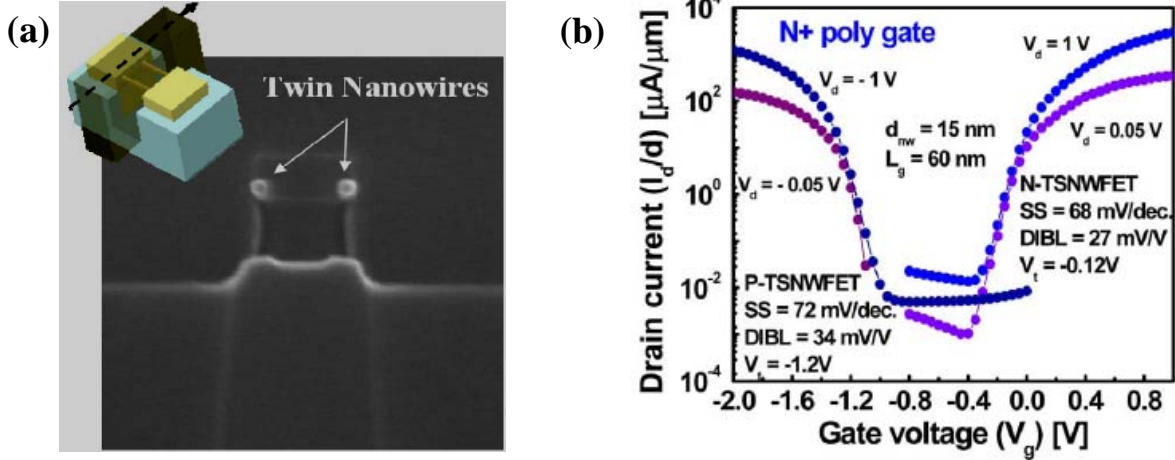


Figure 1.14. (a) Cross-sectional transmission electron micrograph of twin silicon nanowire MOSFET, (b) measured transfer characteristics of n+ poly gate TSNWFETs [75].

### 1.3 Research Objectives and Thesis Overview

In **Chapter 2** the benefits of thin-BOX FD-SOI technology for 6-T SRAM scaling are investigated. Firstly, three-dimensional atomistic process and device simulations for thin-BOX FD-SOI and planar bulk MOSFET designs for low-operating-power (LOP) applications at the 22 nm node are presented. Then the benefits of transistor performance improvement and  $V_T$  variation reduction offered by FD-SOI technology are assessed via iso-area and iso-yield analysis. Finally, the minimum operating voltage ( $V_{min}$ ) for 6 $\sigma$  yield is projected for FD-SOI and planar bulk SRAM cells.

To avoid the need for costly silicon-on-insulator substrates or complex fabrication processes, the quasi-planar (QP) bulk MOSFET design for CMOS scaling to the end of the roadmap was recently proposed [76]. The following four chapters (**Chapters 3 to 6**) theoretically and experimentally investigate the QP bulk device structure, *e.g.*, how best to suppress  $V_T$  variation, to maximize performance, to minimize SRAM  $V_{min}$ , and to enhance SRAM yield.

In **chapter 3**, RDF-induced  $V_T$  variation for the quasi-planar bulk MOSFET *vs.* the planar bulk MOSFET at the 22 nm node (25 nm gate length) is studied using atomistic three-dimensional device simulation. The impact of body/channel or source/drain doping

profile on  $V_T$  variation is presented. Lastly, a new method of  $V_T$  tuning in the quasi-planar bulk MOSFET is proposed to mitigate the tradeoff between  $V_T$  variation and short-channel effect suppression.

In **chapter 4**, full 3-D 6T-SRAM cell simulations are used to assess the benefits of the quasi-planar bulk MOSFET design for 22 nm SRAM technology. A segmented channel design is proposed to enhance SRAM yield and improve immunity to single-event upsets.

In **chapter 5**, a simple method (*i.e.*, a timed dilute-HF etch for recessing the shallow trench isolation just prior to gate-stack formation) of manufacturing quasi-planar bulk MOSFET structures is experimentally demonstrated in a 28 nm CMOS technology. The benefits of the quasi-planar bulk structure for improving device performance and reducing variation in 6T-SRAM read and write margins are presented. Due to its increased benefits with decreasing channel width, quasi-planar bulk MOSFET technology is a promising solution for future CMOS technology generations (22 nm and beyond).

In **chapter 6**, 3D device simulation with considerations of three main random variation factors (*i.e.*, line-edge-roughness, random dopant fluctuation, and work-function variation) is used to quantitatively show the benefits of the quasi-planar bulk MOSFET (improved performance and reduced  $V_T$  variation) as compared against a planar bulk MOSFET. A compact analytical model is used to quantitatively project the benefits of QP bulk CMOS technology, specifically enhancement of write-ability and write time for comparable read stability, as well as SRAM yield improvement and  $V_{min}$  reduction. Additionally, a notchless quasi-planar bulk SRAM cell design is proposed for improved printability.

In **chapter 7**, the contributions of this dissertation are summarized and suggestions for future research are made.

## 1.4 References

- [1] G. E. Moore, "Cramming more components onto integrated circuits," *Proc. of the IEEE*, vol. 86, no. 1, pp. 82-85, Jan. 1998.
- [2] International Technology Roadmap for Semiconductors (ITRS). [Online]. Available: <http://public.itrs.net>
- [3] M. J. M. Pelgrom, A. Duinmaijer, and A. Welbers, "Matching properties of MOS transistors," *IEEE J. Solid-State Circuits*, vol. 24, no. 5, pp. 1433-1440, Oct. 1989.
- [4] K. J. Kuhn, "Reducing variation in advanced logic technologies: approaches to process and design for manufacturability of nanoscale CMOS," *IEDM Tech. Dig.*, Dec. 2007, pp. 471-474.
- [5] E. Seevinck, F. J. List, and J. Lohstroh, "Static-noise margin analysis of MOS SRAM cells," *IEEE J. Solid-State Circuits*, vol. 22, no. 5, pp. 748-754, Oct. 1987.



- [6] C. Wann, R. Wong, D. J. Frank, R. Mann, S.-B. Ko, P. Croce, D. Lea, D. Hoyniak, Y.-M. Lee, J. Toomey, M. Weybright, and J. Sudijono, "SRAM cell design for stability methodology," *Proc. IEEE VLSI-TSA*, Apr. 2005, pp. 21–22.
- [7] E. Grossar, M. Stucchi, K. Maex, and W. Dehaene, "Read stability and write-ability analysis of SRAM cells for nanometer technologies," *IEEE J. Solid-State Circuits*, vol. 41, no. 11, pp. 2577–2588, Nov. 2006.
- [8] A. Carlson, Z. Guo, S. Balasubramanian, L.-T. Pang, T.-J. King Liu, and B. Nikolic, "FinFET SRAM with enhanced read/write margins," *IEEE International SOI Conference*, Oct. 2006, pp. 105–106.
- [9] Rashmi, A. Kranti, and G. A. Armstrong, "6-T SRAM cell design with nanoscale double-gate SOI MOSFETs: impact of source/drain engineering and circuit topology," *IOP Semiconductor Science and Technology*, vol. 23, no. 7, pp. 1-13, Jul. 2008.
- [10] R. F. Lyon and R. R. Schediwy, "CMOS static memory with a new four transistor memory cell," *Proc. of Stanford conference on advanced research in VLSI*, pp. 111–131, 1987.
- [11] K. Noda, K. Matsui, K. Imai, K. Inoue, K. Tokashiki, H. Kawamoto, K. Yoshida, K. Takeda, N. Nakamura, T. Kimura, H. Toyoshima, Y. Koishikawa, S. Maruyama, T. Saitoh, and T. Tanigawa, "A 1.9- $\mu\text{m}^2$  loadless CMOS four-transistor SRAM cell in a 0.18- $\mu\text{m}$  logic technology," *IEDM Tech. Dig.*, Dec. 1998, pp. 643–646.
- [12] N. Lindert, Y.-K. Choi, L. Chang, E. Anderson, W. Lee, T.-J. King, J. Bokor, and C. Hu, "Quasi-planar NMOS FinFETs with sub-100 nm gate lengths," *IEEE Device Research Conference*, Jun. 2001, pp. 26–27.
- [13] O. Semenov, A. Pavlov, and M. Sachdev, "Sub-quarter micron SRAM cells stability in low-voltage operation: a comparative analysis," *IEEE International Reliability Workshop*, Oct. 2002, pp. 168–171.
- [14] Z. Guo, S. Balasubramanian, R. Zlatanovici, T.-J. King, and B. Nikolic, "FinFET-based SRAM design," *IEEE International Symposium on Low Power Electronics and Design*, Aug. 2005, pp. 2–7.
- [15] B. Giraud, A. Amara, and A. Vladimirescu, "A comparative study of 6T and 4T SRAM cells in double gate CMOS with statistical variation," *IEEE International Symposium on Circuits and Systems*, May 2007, pp. 3022–3025.
- [16] K. Takeda, Y. Hagihara, Y. Aimoto, M. Nomura, Y. Nakazawa, T. Ishii, and H. Kobatake, "A Read-Static-Noise-Margin-Free SRAM cell for low- $V_{\text{DD}}$  and high-speed applications," *ISSCC Dig. of Tech. Papers*, Feb. 2005, pp. 478-479.
- [17] K. Takeda, Y. Hagihara, Y. Aimoto, M. Nomura, Y. Nakazawa, T. Ishii, and H. Kobatake, "A Read-Static-Noise-Margin-Free SRAM cell for low- $V_{\text{DD}}$  and high-speed applications," *IEEE J. Solid-State Circuits*, vol. 41, no. 1, pp. 113–121, Jan. 2006.
- [18] R. Joshi, R. Houle, K. Batson, D. Rodko, P. Patel, W. Huott, R. Franch, Y. Chan, D. Plass, S. Wilson, and P. Wang "6.6+ GHz low  $V_{\text{min}}$ , read and half select disturb-free 1.2 Mb SRAM," *VLSI Symp. Circuit Dig.*, Jun. 2007, pp. 250-251.
- [19] L. Chang, Y. Nakamurat, R. K. Montoye, J. Sawada, A. K. Martin, K. Kinoshita, F. H. Gebara, K. B. Agarwalt, D. J. Acharyya, W. Haensch, K. Hosokawat, and D. Jamsek, "A 5.3GHz 8-T SRAM with operation down to 0.41V in 65nm CMOS," *VLSI Symp. Circuit Dig.*, Jun. 2007, pp. 252-253.

- [20] S. Ishikura, M. Kurumada, T. Terano, Y. Yamagami, N. Kotani, K. Satomi, K. Nii, M. Yabuuchi, Y. Tsukamoto, S. Ohbayashi, T. Oashi, H. Makino, H. Shinohara, and H. Akamatsu, "A 45nm 2 port 8T-SRAM using hierarchical replica bitline technique with immunity from simultaneous R/W access issues," *VLSI Symp. Circuit Dig.*, Jun. 2007, pp. 254-255.
- [21] Y. Morita, H. Fujiwara, H. Noguchi, Y. Iguchi, K. Nii, H. Kawaguchi, and M. Yoshimoto, "An area-conscious low-voltage-oriented 8T-SRAM design under DVS environment," *VLSI Symp. Circuit Dig.*, Jun. 2007, pp. 256-257.
- [22] I. J. Chang, J.-J. Kim, S. P. Park, K. Roy "A 32kb 10T subthreshold SRAM array with bit-interleaving and differential read scheme in 90nm CMOS," *ISSCC Dig. of Tech. Papers*, Feb. 2008, pp. 388-389.
- [23] A. Asenov, "Simulation of statistical variability in nano MOSFETs," *VLSI Symp. Tech. Dig.*, Jun. 2007, pp. 86-87.
- [24] A. Asenov, "Random dopant induced threshold voltage lowering and fluctuations in sub 50 nm MOSFETs: a statistical 3D 'atomistic' simulation study," *IOP Semiconductor Science and Technology*, vol. 10, no. 2, pp. 153-158, Feb. 1999.
- [25] R. W. Keyes, "Physical limits in digital electronics," *Proc. of the IEEE*, vol. 63, no. 5, pp. 740-767, May 1975.
- [26] T. Mizuno, J.-I. Okamura, and A. Toriumi, "Experimental study of threshold voltage fluctuation due to statistical variation of channel dopant number in MOSFETs," *IEEE Trans. Electron Devices*, vol. 41, no. 11, pp. 2216-2221, Nov. 1994.
- [27] A. Asenov and S. Saini, "Suppression of random dopant-induced threshold voltage fluctuations in sub-0.1- $\mu\text{m}$  MOSFET's with epitaxial and  $\delta$ -doped channels," *IEEE Trans. Electron Devices*, vol. 46, no. 8, pp. 1718-1724, Aug. 1999.
- [28] A. Cathignol, B. Cheng, D. Chanemougame, A. R. Brown, K. Rochereau, G. Ghibaudo, and A. Asenov, "Quantitative evaluation of statistical variability sources in a 45-nm technological node LP N-MOSFET," *IEEE Electron Device Lett.*, vol. 29, no. 6, pp. 609-611, Jun. 2008.
- [29] D. Reid, C. Millar, G. Roy, S. Roy, and A. Asenov, "Analysis of threshold voltage distribution due to random dopants: A 100 000-sample 3-D simulation study," *IEEE Trans. Electron Devices*, vol. 56, no. 10, pp. 2255-2263, Oct. 2009.
- [30] T. Ohtou, N. Sugii, and T. Hiramoto, "Impact of parameter variations and random dopant fluctuations on short-channel fully depleted SOI MOSFETs with extremely thin BOX," *IEEE Electron Device Lett.*, vol. 28, no. 8, pp. 740-742, Aug. 2007.
- [31] M. Hane, T. Ikezawa, and T. Ezaki, "Coupled atomistic 3D process/device simulation considering both line-edge roughness and random-discrete-dopant effects," *IEEE International conference on simulation of semiconductor processes and devices (SISPAD)*, Sep. 2003, pp. 99-102.
- [32] T. Yoshimura, H. Shiraishi, J. Yamamoto, and S. Okazaki, "Nanoedge roughness in polymer resist patterns," *Appl. Phys. Lett.*, vol. 63, no. 6, pp. 764-766, Aug. 1993.
- [33] T. Yamaguchi, K. Yamazaki, M. Nagase, and H. Namatsu, "Line-edge roughness: characterization and material origin," *Jpn. J. Appl. Phys.*, vol. 42, no. 6B, pp. 3755-3762, Jun. 2003.

- [34] X. Sun and T.-J. King Liu, "Spacer gate lithography for reduced variability due to line edge roughness," *IEEE Trans. Semiconductor Manufacturing*, vol. 23, no. 2, pp. 311-315, May 2010.
- [35] Y.-K. Choi, T.-J. King, and C. Hu, "A spacer patterning technology for nanoscale CMOS," *IEEE Trans. Electron Devices*, vol. 49, no. 3, pp. 436-441, Mar. 2002.
- [36] H. F. Dadgour, K. Endo, V. K. De, and K. Banerjee, "Grain-orientation induced work function variation in nanoscale metal-gate transistors—part I: modeling, analysis, and experimental validation," *IEEE Trans. Electron Devices*, vol. 57, no. 10, pp. 2504-2514, Oct. 2010.
- [37] H. F. Dadgour, K. Endo, V. K. De, and K. Banerjee, "Grain-orientation induced work function variation in nanoscale metal-gate transistors—part II: implications for process, device, and circuit design," *IEEE Trans. Electron Devices*, vol. 57, no. 10, pp. 2515-2525, Oct. 2010.
- [38] H. Pilo, J. Barwin, G. Bracer, C. Browning, S. Burns, J. Gabric, S. Lamphier, M. Miller, A. Roberts, and F. Towler, "An SRAM design in 65nm and 45nm technology nodes featuring read and write-assist circuits to expand operating voltage," *VLSI Symp. Circuit Dig.*, Jun. 2006, pp. 15-16.
- [39] K. Zhang, U. Bhattacharya, Z. Chen, F. Hamzaoglu, D. Murray, N. Vallepalli, Y. Wang, B. Zheng, and M. Bohr, "A 3 GHz 70Mb SRAM in 65nm CMOS technology with integrated column-based dynamic power supply," *ISSCC Dig. of Tech. Papers*, Feb. 2005, pp. 474-475.
- [40] K. Mistry, C. Allen, C. Auth, B. Beattie, D. Bergstrom, M. Bost, M. Brazier, M. Buehler, A. Cappellani, R. Chau, C.-H. Choi, G. Ding, K. Fischer, T. Ghani, R. Grover, W. Han, D. Hanken, M. Hattendorf, J. He, J. Hicks, R. Huessner, D. Ingerly, P. Jain, R. James, L. Jong, S. Joshi, C. Kenyon, K. Kuhn, K. Lee, H. Liu, J. Maiz, B. McIntyre, P. Moon, J. Neiryneck, S. Pae, C. Parker, D. Parsons, C. Prasad, L. Pipes, M. Prince, P. Ranade, T. Reynolds, J. Sandford, L. Shifren, J. Sebastian, J. Seiple, D. Simon, S. Sivakumar, P. Smith, C. Thomas, T. Troeger, P. Vandervoorn, S. Williams, and K. Zawadzki, "A 45nm logic technology with high-k + metal gate transistors, strained silicon, 9 Cu interconnect layers, 193nm dry patterning, and 100% Pb-free packaging," *IEDM Tech. Dig.*, Dec. 2007, pp. 247-250.
- [41] C. Auth, A. Cappellani, J.-S. Chun, A. Dalis, A. Davis, T. Ghani, G. Glass, T. Glassman, M. Harper, M. Hattendorf, P. Hentges, S. Jaloviar, S. Joshi, J. Klaus, K. Kuhn, D. Lavric, M. Lu, H. Mariappan, K. Mistry, B. Norris, N. Rahhal-orabi, P. Ranade, J. Sandford, L. Shifren, V. Souw, K. Tone, F. Tambwe, A. Thompson, D. Towner, T. Troeger, P. Vandervoorn, C. Wallace, J. Wiedemer, and C. Wiegand, "45nm high-k + metal gate strain-enhanced transistors," *VLSI Symp. Tech. Dig.*, Jun. 2008, pp. 128-129.
- [42] O. Weber, O. Faynot, F. Andrieu, C. Buj-Dufournet, F. Allain, P. Scheiblin, J. Foucher, N. Daval, D. Lafond, L. Tosti, L. Brevard, O. Rozeau, C. Fenouillet-Beranger, M. Marin, F. Boeuf, D. Delprat, K. Bourdelle, B.-Y. Nguyen, and S. Deleonibus, "High immunity to threshold voltage variability in undoped ultra-thin FDSOI MOSFETs and its physical understanding," *IEDM Tech. Dig.*, Dec. 2008, pp. 1-4.

- [43] S. Narasimha, K. Onishi, H. M. Nayfeh, A. Waite, M. Weybright, J. Johnson, C. Fonseca, D. Corliss, C. Robinson, M. Crouse, D. Yang, C-H. J. Wu, A. Gabor, T. Adam, I. Ahsan, M. Belyansky, L. Black, S. Butt, J. Cheng, A. Chou, G. Costrini, C. Dimitrakopoulos, A. Domenicucci, P. Fisher, A. Frye, S. Gates, S. Greco, S. Grunow, M. Hargrove, J. Holt, S-J. Jeng, M. Kelling, B. Kim, W. Landers, G. Larosa, D. Lea, M.H. Lee, X. Liu, N. Lustig, A. McKnight, L. Nicholson, D. Nielsen, K. Nummy, V. Ontalus, C. Ouyang, X. Ouyang, C. Prindle, R. Pal, W. Rausch, D. Restaino, C. Sheraw, J. Sim, A. Simon, T. Standaert, C.Y. Sung, K. Tabakman, C. Tian, R. Van Den Nieuwenhuizen, H. Van Meer, A. Vayshenker, D. Wehella-Gamage, J. Werking, R. C. Wong, J. Yu, S. Wu, R. Augur, D. Brown, X. Chen, D. Edelstein, A. Grill, M. Khare, Y. Li, S. Luning, J. Norum, S. Sankaran, D. Schepis, R. Wachnik, R. Wise, C. Wann, T. Ivers, and P. Agnello, "High performance 45-nm SOI technology with enhanced strain, porous low-k BEOL, and immersion lithography," *IEDM Tech. Dig.*, Dec. 2006, pp. 1–4.
- [44] K. Cheng, A. Khakifirooz, P. Kulkarni, S. Kanakasabapathy, S. Schmitz, A. Reznicek, T. Adam, Y. Zhu, J. Li, J. Faltermeier, T. Furukawa, L. F. Edge, B. Haran, S.-C. Seo, P. Jamison, J. Holt, X. Li, R. Loesing, Z. Zhu, R. Johnson, A. Upham, T. Levin, M. Smalley, J. Herman, M. Di, J. Wang, D. Sadana, P. Kozlowski, H. Bu, B. Doris, and J. O'Neill, "Fully depleted extremely thin SOI technology fabricated by a novel integration scheme featuring implant-free, zero-silicon-loss, and faceted raised source/drain," *VLSI Symp. Tech. Dig.*, Jun. 2009, pp. 212–213.
- [45] M. Chudzik, B. Doris, R. Mo, J. Sleight, E. Cartier, C. Dewan, D. Park, H. Bu, W. Natzle, W. Yan, C. Ouyang, K. Henson, D. Boyd, S. Callegari, R. Carter, D. Casarotto, M. Gribelyuk, M. Hargrove, W. He, Y. Kim, B. Linder, N. Moumen, V.K. Paruchuri, J. Stathis, M. Steen, A. Vayshenker, X. Wang, S. Zafar, T. Ando, R. Iijima, M. Takayanagi, V. Narayanan, R. Wise, Y. Zhang, R. Divakaruni, M. Khare, and T.C. Chen, "High-performance high-k/metal gates for 45nm CMOS and beyond with gate-first processing," *VLSI Symp. Tech. Dig.*, Jun. 2007, pp. 194–195.
- [46] S. Narasimha, K. Onishi, H. M. Nayfeh, A. Waite, M. Weybright, J. Johnson, C. Fonseca, D. Corliss, C. Robinson, M. Crouse, D. Yang, C-H. J. Wu, A. Gabor, T. Adam, I. Ahsan, M. Belyansky, L. Black, S. Butt, J. Cheng, A. Chou, G. Costrini, C. Dimitrakopoulos, A. Domenicucci, P. Fisher, A. Frye, S. Gates, S. Greco, S. Grunow, M. Hargrove, J. Holt, S-J. Jeng, M. Kelling, B. Kim, W. Landers, G. Larosa, D. Lea, M.H. Lee, X. Liu, N. Lustig, A. McKnight, L. Nicholson, D. Nielsen, K. Nummy, V. Ontalus, C. Ouyang, X. Ouyang, C. Prindle, R. Pal, W. Rausch, D. Restaino, C. Sheraw, J. Sim, A. Simon, T. Standaert, C.Y. Sung, K. Tabakman, C. Tian, R. Van Den Nieuwenhuizen, H. Van Meer, A. Vayshenker, D. Wehella-Gamage, J. Werking, R. C. Wong, J. Yu, S. Wu, R. Augur, D. Brown, X. Chen, D. Edelstein, A. Grill, M. Khare, Y. Li, S. Luning, J. Norum, S. Sankaran, D. Schepis, R. Wachnik, R. Wise, C. Wann, T. Ivers, P. Agnello, "High performance 45-nm SOI technology with enhanced strain, porous low-k BEOL, and immersion lithography," *IEDM Tech. Dig.*, Dec. 2006, pp. 1–4.

- [47] D. Suh and J. G. Fossum, "Dynamic floating-body instabilities in partially depleted SOI CMOS circuits," *IEDM Tech. Dig.*, Dec. 1994, pp. 661–664.
- [48] P.-F. Lu, C.-T. Chuang, J. Ji, L. F. Wagner, C.-M. Hsieh, J. B. Kuang, L. L.-C. Hsu, M. M. Pelella, S.-F. S. Chu, and C. J. Anderson, "Floating-body effects in partially depleted SOI CMOS circuits," *IEEE J. Solid-State Circuits*, vol. 32, no. 8, pp. 1241–1253, Aug. 1997.
- [49] C.-T. Chuang, P.-F. LU, and C. J. Anderson, "SOI for digital CMOS VLSI: design considerations and advances," *Proc. of the IEEE*, vol. 86, no. 4, pp. 689–720, Apr. 1998.
- [50] SOI Industry Consortium [Online]. Available: <http://www.soiconsortium.org>
- [51] Y.-K. Choi, K. Asano, N. Lindert, V. Subramanian, T.-J. King, J. Bokor, and C. Hu, "Ultra-thin body SOI MOSFET for deep-sub-tenth micron era," *IEDM Tech. Dig.*, Dec. 1999, pp. 919–921.
- [52] K. Cheng, A. Khakifirooz, P. Kulkarni, S. Ponoth, J. Kuss, D. Shahrjerdi, L. F. Edge, A. Kimball, S. Kanakasabapathy, K. Xiu, S. Schmitz, A. Reznicek, T. Adam, H. He, N. Loubet, S. Holmes, S. Mehta, D. Yang, A. Upham, S.-C. Seo, J. L. Herman, R. Johnson, Y. Zhu, P. Jamison, B. S. Haran, Z. Zhu, L. H. Vanamurth, S. Fan, D. Horak, H. Bu, P. J. Oldiges, D. K. Sadana, P. Kozlowski, D. McHerron, J. O'Neill, B. Doris, "Extremely thin SOI (ETSOI) CMOS with record low variability for low power system-on-chip applications," *IEDM Tech. Dig.*, Dec. 2009, pp. 1-4.
- [53] C. L. Chen, R.T. Chang, P.W. Wyatt, C. K. Chen, D.-R. Yost, J. M. Knecht, and C. L. Keast, "Floating body effects on the RF performance of FDSOI RF amplifiers," *IEEE International SOI Conference*, Oct. 2005, pp. 44-46.
- [54] C. Mazuré, R. Ferrant, B.-Y. Nguyen, W. Schwarzenbach, C. Moulin, "FDSOI: from substrate to devices and circuit applications," *Proc. of European Solid-State Circuits Conference (ESSCIRC)*, Sep. 2010, pp. 45-51.
- [55] T. Ernst, S. Cristoloveanu, G. Ghibaudo, T. Ouisse, S. Horiguchi, Y. Ono, Y. Takahashi, and K. Murase, "Ultimately thin double-gate SOI MOSFETs," *IEEE Trans. Electron Devices*, vol. 50, no. 3, pp. 830-838, Mar. 2003.
- [56] Z. Krivokapic, W. P. Maszara, and M.-R. Lin, "Manufacturability of 20-nm ultrathin body fully depleted SOI devices with FUSI metal gates," *IEEE Trans. Semiconductor Manufacturing*, vol. 18, no. 1 pp. 5-12, Feb. 2005.
- [57] V. Carron, F. Nemouchi, Y. Morand, T. Poiroux, M. Vinet, S. Bernasconi, O. Louveau, D. Lafond, V. Delaye, F. Allain, S. Minoret, L. Vandroux, and T. Billon, "Platinum silicide metallic source & drain process optimization for FDSOI pMOSFETs," *IEEE International SOI Conference*, Oct. 2009, pp. 1-2.
- [58] T. Ohtou, N. Sugii, and T. Hiramoto, "Impact of parameter variations and random dopant fluctuations on short-channel fully depleted SOI MOSFETs with extremely thin BOX," *IEEE Electron Device Lett.*, vol. 28, no. 8, pp. 740-742, Aug. 2007.
- [59] D. Delprat, F. Boedt, C. David, P. Reynaud, A. Alami-Idrissi, D. Landru, C. Girard, and C. Maleville, "SOI substrate readiness for 22/20 nm and for fully depleted planar device architectures," *IEEE International SOI Conference*, Oct. 2009, pp. 1-4.
- [60] D. Hisamoto, W.-C. Lee, J. Kedzierski, E. Anderson, H. Takeuchi, K. Asano, T.-J. King, J. Bokor, and C. Hu, "A folded-channel MOSFET for deep-sub-tenth micron era," *IEDM Tech. Dig.*, Dec. 1998, pp. 1032-1034.

- [61] N. Lindert, Y.-K. Choi; L. Chang; E. Anderson, W.-C. Lee, T.-J. King, J. Bokor, C. Hu, "Quasi-planar NMOS FinFETs with sub-100nm gate lengths," *IEEE Device Research Conference*, Jun. 2001, pp. 26-27.
- [62] H. Kawasaki, M. Khater, M. Guillorn, N. Fuller, J. Chang, S. Kanakasabapathy, L. Chang, R. Muralidhar, K. Babich, Q. Yang, J. Ott, D. Klaus, E. Kratschmer, E. Sikorski, R. Miller, R. Viswanathan, Y. Zhang, J. Silverman, Q. Ouyang, A. Yagishita, M. Takayanagi, W. Haensch, and K. Ishimaru, "Demonstration of highly scaled FinFET SRAM cells with high-K/metal gate and investigation of characteristic variability for the 32nm node and beyond," *IEDM Tech. Dig.*, Dec. 2008, pp. 237-240.
- [63] C. C. Wu, D. W. Lin, A. Keshavarzi, C. H. Huang, C. T. Chan, C. H. Tseng, C. L. Chen, C. Y. Hsieh, K. Y. Wong, M. L. Cheng, T. H. Li, Y. C. Lin, L.Y. Yang, C. P. Lin, C. S. Hou, H. C. Lin, J. L. Yang, K. F. Yu, M. J. Chen, T. H. Hsieh, Y. C. Peng, C. H. Chou, C. J. Lee, C. W. Huang, C. Y. Lu, F. K. Yang, H. K. Chen, L. W. Weng, P. C. Yen, S. H. Wang, S. W. Chang, S. W. Chuang, T. C. Gan, T. L. Wu, T. Y. Lee, W. S. Huang, Y. J. Huang, Y. W. Tseng, C. M. Wu, E. Ou-Yang, K. Y. Hsu, L. T. Lin, S. B. Wang, T. M. Kwok, C. C. Su, C. H. Tsai, M. J. Huang, H. M. Lin, A. S. Chang, S. H. Liao, L. S. Chen, J. H. Chen, P. S. Lim, X. F. Yu, S. Y. Ku, Y. B. Lee, P. C. Hsieh, P. W. Wang, Y. H. Chiu, S. S. Lin, H. J. Tao, M. Cao, and Y.J. Mii, "High performance 22/20nm FinFET CMOS devices with advanced high-k/metal gate scheme," *IEDM Tech. Dig.*, Dec. 2010, pp. 27.1.1-27.1.4.
- [64] A. Veloso, S. Demuyne, M. Ercken, A. M. Goethals, S. Locorotondo, F. Lazzarino, E. Altamirano, C. Huffman, A. De Keersgieter, S. Brus, M. Demand, H. Struyf, J. De Backer, J. Hermans, C. Delvaux, B. Baudemprez, T. Vandeweyer, F. Van Roey, C. Baerts, D. Goossens, H. Dekkers, P. Ong, N. Heylen, K. Kellens, H. Volders, A. Hikavyy, C. Vrancken, M. Rakowski, S. Verhaegen, M. Dusa, L. Romijn, C. Pignoret, A. Van Dijk, R. Schreutelkamp, A. Cockburn, V. Gravey, H. Meiling, B. Hultermans, S. Lok, K. Shah, R. Rajagopalan, J. Gelatos, O. Richard, H. Bender, G. Vandenberghe, G. P. Beyer, P. Absil, T. Hoffmann, K. Ronse, and S. Biesemans, "Demonstration of scaled  $0.099\mu\text{m}^2$  FinFET 6T-SRAM cell using full-field EUV lithography for (Sub-)22nm node single-patterning technology," *IEDM Tech. Dig.*, Dec. 2009, pp. 27.1.1-27.1.4.
- [65] H. Lee, L.-E. Yu, S.-W. Ryu, J.-W. Han, K. Jeon, D.-Y. Jang, K.-H. Kim, J. Lee, J.-H. Kim, S. C. Jeon, G. S. Lee, J. S. Oh, Y. C. Park, W. H. Bae, H. M. Lee, J. M. Yang, J. J. Yoo, S. I. Kim, and Y.-K. Choi, "Sub-5nm all-around gate FinFET for ultimate scaling," *VLSI Symp. Tech. Dig.*, Jun. 2006, pp. 58-59.
- [66] T. Park, S. Choi, D. H. Lee, J. R. Yoo, B. C. Lee, J. Y. Kim, C. G. Lee, K. K. Chi, S. H. Hong, S. J. Hyun, Y. G. Shin, J. N. Han, I. S. Park, U. I. Chung, J. T. Moon, E. Yoon, and J. H. Lee, "Fabrication of body-tied FinFETs (Omega MOSFETs) using bulk Si wafers," *VLSI Symp. Tech. Dig.*, Jun. 2003, pp. 135-136.
- [67] T.-J. King, "FinFET promise and challenges," *Extended Abstracts of the 2003 International Conference on Solid-State Devices and Materials (SSDM)*, Sep. 2003, pp. 280-281.

- [68] L. Chang, S. Tang, T.-J. King, J. Bokor, and C. Hu, "Gate length scaling and threshold voltage control of double-gate MOSFETs," *IEDM Tech. Dig.*, Dec. 2000, pp. 719-722.
- [69] V. Vidya and T.-J. King Liu, " $V_T$  adjustment by  $L_{eff}$  engineering for LSTP single gate work-function CMOS FinFET technology," *Proc. of 16th Biennial University Government Industry Microelectronics Symposium*, Jun. 2006.
- [70] S. A. Tawfik and V. Kursun, "Portfolio of FinFET memories: innovative techniques for an emerging technology," *Proc. of International SoC Design Conference (ISOCC)*, Nov. 2008, pp. I-101 – I-104.
- [71] F.-L. Yang, H.-Y. Chen, F.-C. Chen, C.-C. Huang, C.-Y. Chang, H.-K. Chiu, C.-C. Lee, C.-C. Chen, H.-T. Huang, C.-J. Chen, H.-J. Tao, Y.-C. Yeo, M.-S. Liang, and C. Hu, "25 nm CMOS omega FETs," *IEDM Tech. Dig.*, Dec. 2002, pp. 255–258.
- [72] C. Jahan, O. Faynot, M. Cassé, R. Ritzenthaler, L. Brévard, L. Tosti, X. Garros, C. Vizios, F. Allain, A.M. Papon, H. Dansas, F. Martin, M. Vinet, B. Guillaumot, A. Toffoli, B. Giffard, and S. Deleonibus, "QFETs transistors with TiN metal gate and  $HfO_2$  down to 10nm," *VLSI Symp. Tech. Dig.*, Jun. 2005, pp. 112-113.
- [73] B. Doyle, B. Boyanov, S. Datta, M. Doczy, S. Harelend, B. Jin, J. Kavalieros, T. Linton, R. Rios, and R. Chau, "Tri-gate fully-depleted CMOS transistors: fabrication, design and layout," *VLSI Symp. Tech. Dig.*, Jun. 2003, pp. 133-134.
- [74] S. D. Suk, S.-Y. Lee, S.-M. Kim, E.-J. Yoon, M.-S. Kim, M. Li, C. W. Oh, K. H. Yeo, S. H. Kim, D.-S. Shin, K.-H. Lee, H. S. Park, J. N. Han, C. J. Park, J.-B. Park, D.-W. Kim, D. Park, and B.-I. Ryu, "High performance 5nm radius Twin Silicon Nanowire MOSFET(TSNWFET): fabrication on bulk Si wafer, characteristics, and reliability," *IEDM Tech. Dig.*, Dec. 2005, pp. 717–720.
- [75] S. D. Suk, K. H. Yeo, K. H. Cho, M. Li, Y. Y. Yeoh, S.-Y. Lee, S. M. Kim, E.-J. Yoon, M. S. Kim, C. W. Oh, S. H. Kim, D.-W. Kim, and D. Park, "High-performance Twin Silicon Nanowire MOSFET (TSNWFET) on bulk Si wafer," *IEEE Trans. Nanotechnology*, vol. 7, no. 2, pp. 181-184, Mar. 2008.
- [76] X. Sun, Q. Lu, V. Moroz, H. Takeuchi, G. Gebara, J. Wetzel, S. Ikeda, C. Shin, and T.-J. King Liu, "Tri-gate bulk MOSFET design for CMOS scaling to the end of the roadmap," *IEEE Electron Device Lett.*, vol. 29, no. 5, pp. 491-493, May 2008.

## Chapter 2

# Performance and Area Scaling Benefits of FD-SOI Technology for 6-T SRAM Cells at the 22nm node

### 2.1 Introduction

Increasing variation in transistor performance with gate-length ( $L_{\text{GATE}}$ ) scaling is a major challenge for continued bulk CMOS technology advancement [1]. The primary causes for random variations in transistor threshold voltage ( $V_{\text{TH}}$ ) are gate line-edge roughness (LER) and random dopant fluctuations (RDF) [2]. A lightly doped (fully depleted, FD) silicon-on-insulator (SOI) MOSFET structure with a very thin ( $\sim 10$  nm-thick) buried oxide (BOX) layer and a heavily doped substrate (“ground plane”) has been shown to be effective for reducing the impact of parameter variations and RDF, due to its excellent electrostatic integrity and the elimination of channel doping [3]. Recently, functional SRAM cells were demonstrated using such FD-SOI devices, for the 32 nm technology node and beyond [4]. Also, thin-BOX FD-SOI MOSFET technology has been projected to provide for improved SRAM yield as compared to SOI FinFET technology at the 22 nm technology node [5]. In this chapter, which follows [6], the potential advantages of thin-BOX FD-SOI technology *vs.* bulk CMOS technology with regard to six-transistor (6-T) SRAM cell performance and yield are assessed in detail, for the 22 nm technology node.

### 2.2 Thin-BOX FD-SOI Technology

#### 2.2.1 MOSFET Design Optimization

The thin-BOX FD-SOI CMOSFET designs were optimized via three-dimensional (3-D) process and device simulations with advanced physical models including the density-



gradient and drift-diffusion transport models [7] and the phenomenological van Dort quantum correction model to account for energy quantization in the channel region. Physical and operating parameters (gate length, gate oxide thickness, supply voltage, etc.) were taken from the International Technology Roadmap for Semiconductors for low operating power (LOP) technology at the 22 nm node [8]. The width of the gate-sidewall spacers ( $W_{\text{spacer}}$ ) is constrained by the gate-to-contact spacing design rule for the 6-T SRAM cell, and was selected to be 15nm based on [10] and in consideration of the design optimization guidelines in [9]. **Fig. 2.1(a)** shows a cross-sectional view of the simulated n-channel MOSFET structure. An implantation-free process is used in order to avoid dopant-atom straggle and defects in the thin body region, to minimize RDF-induced variations, as follows [10]: faceted raised-source/drain regions are formed by a low-temperature, zero-silicon-loss epitaxial growth process with in-situ doping ( $10^{20}\text{cm}^{-3}$ ) to reduce series resistance with minimal increase in gate-sidewall capacitance; then the lightly doped source/drain extension regions are formed by diffusion of dopant atoms from the raised-source/drain regions. The electrical channel length ( $L_{\text{eff}}$ , defined as the distance between the lateral positions where the source and drain doping concentrations fall to  $2 \times 10^{19}\text{cm}^{-3}$  [11]) is tuned by adjusting the duration of the dopant-diffusion anneal step, to achieve the maximum drive current for a gate voltage swing and drain bias equal to the supply voltage  $V_{\text{DD}}$  (0.9V). The gate work function values were then selected to adjust the nominal  $V_{\text{TH}}$  values in order to meet the off-state leakage current ( $I_{\text{OFF}}$ ) specification, 3nA/ $\mu\text{m}$ . The optimized device parameters for the FD-SOI devices are summarized in **Table 2.1**.

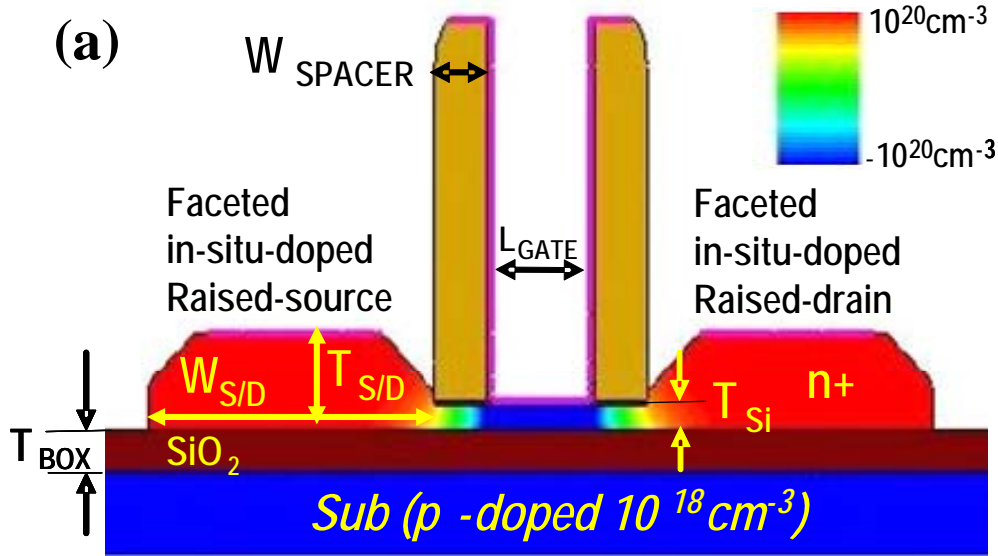


Figure 2.1. (a) Cross-sectional view of the simulated thin-BOX fully-depleted (FD) SOI MOSFET structure. The gate electrode is a thin metal layer with a specified work function.

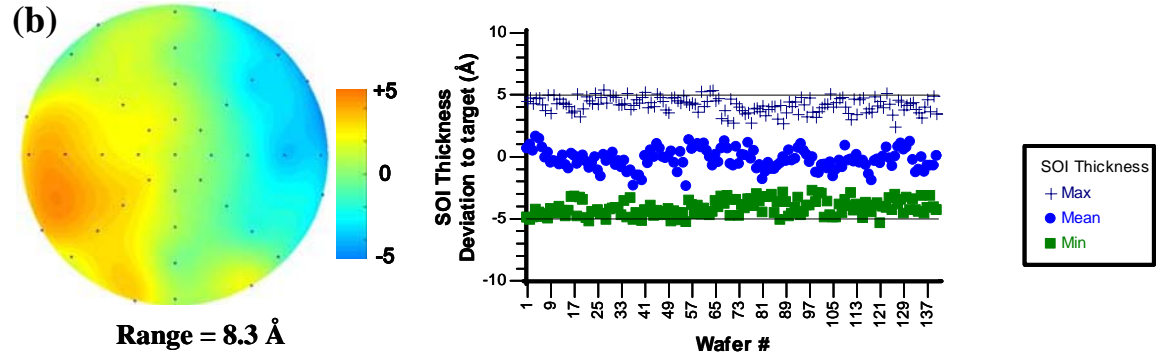


Figure 2.1. (b) Experimental data (courtesy of SOITEC) for SOI layer thickness ( $T_{Si}$ ) variation across a wafer (left) and from wafer to wafer (right). The peak-to-peak variation is less than 1 nm.

	FD-SOI		Planar Bulk	
Parameter	N-type	P-type	N-type	P-type
$L_{GATE}$	25nm	25nm	25nm	25nm
$W_{SPACER}$	15nm	15nm	15nm	15nm
$T_{OX}$	1nm	1nm	1nm	1nm
$T_{BOX}$	10nm	10nm	NA	NA
$T_{Si}$	6nm	6nm	NA	NA
$X_{J,EXT}$	NA	NA	10nm	10nm
$X_{J,S/D}$	NA	NA	22nm	22nm
$\Phi_M$	4.45eV	4.85eV	4.05eV	5.20eV
$T_{S/D}$	22.6nm	22.6nm	NA	NA
$W_{S/D}$	72nm	72nm	72nm	72nm

Table 2.1. Optimized thin-BOX FD-SOI and Planar bulk (uniform channel doping  $\sim 10^{18} \text{cm}^{-3}$ ) MOSFET design parameters for  $V_{DD}=0.9\text{V}$ .

For comparison, planar bulk CMOSFETs meeting the same  $I_{OFF}$  specification also were designed (**Table 2.1**). **Fig. 2.2** compares the transfer characteristics ( $I_{DS}$  vs.  $V_{GS}$ ) for the optimized n-channel FD-SOI and planar bulk MOSFET structures. The FD-SOI device exhibits steeper sub-threshold slope due to negligible depletion capacitance, and higher drive current due to higher carrier mobility. A summary comparison of device performance parameters is given in **Table 2.2**. Both the FD-SOI and planar bulk MOSFET structures meet the general specification for drain-induced barrier lowering (DIBL) to be no greater than 100mV/V. DIBL for the planar bulk devices is comparable to that of the FD-SOI device because of the very shallow source/drain extension depths.

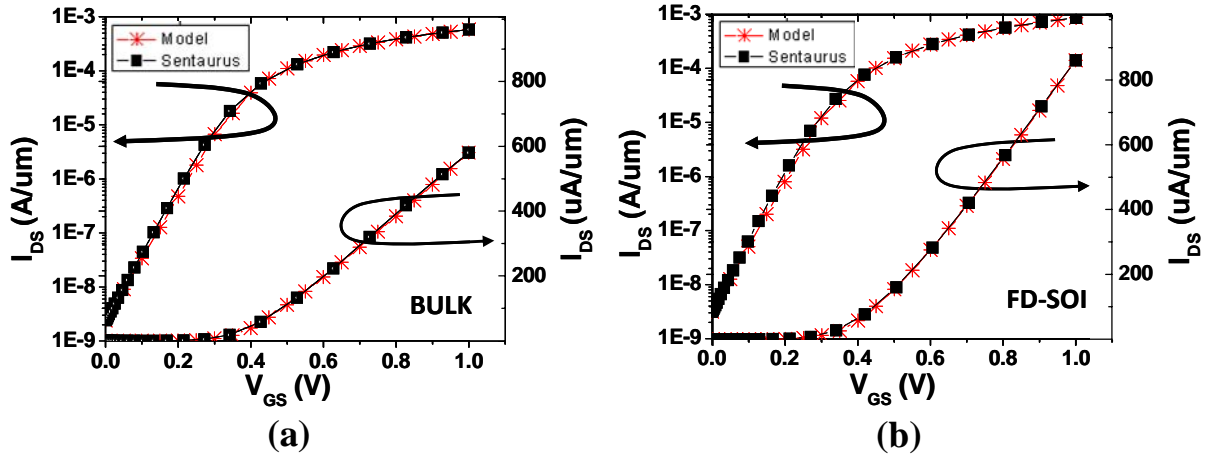


Figure 2.2. Transfer characteristics: (a) Planar bulk MOSFET, (b) FD-SOI MOSFET. The analytical I-V model is fit (to within 5%) to the simulated characteristics, using the current values at 6 points:  $(V_{GS}, V_{DS}) = \{(1.0, 1.0), (1.0, 0.5), (1.0, 0.1), (0.5, 1.0), (0.5, 0.1), (0.0, 1.0)\}$ .

$V_{DD} = 0.9V$	FD-SOI		Planar Bulk	
	N-type	P-type	N-type	P-type
$I_{ON}$ [ $\mu A/\mu m$ ]	704	417	483	301
$I_{OFF}$ [nA/ $\mu m$ ]	3	3	3	3
SS [mV/dec]	75	83	81	89
$V_{T,LIN}$ [mV]	164	-186	182	-207
$V_{T,SAT}$ [mV]	118	-124	134	-142
DIBL [mV/V]	54.1	72.9	56.5	76.5
$L_{eff}$ [nm]	35.6	30.7	46.1	40.5

Table 2.2. Comparison of device performance parameters for  $V_{DD} = 0.9 V$ .

An analytical I-V model for the short-channel MOSFET (Eq. (1) in the Appendix) was fit to the simulated current-vs.-voltage characteristics, and then used to compute SRAM metrics such as read static noise margin (SNM) [12, 14], write current ( $I_w$ ) [13, 14] and read '0' current, following the methodology described in [22]. Five simulated I-V targets corresponding to the operating biases most critical for modeling SRAM metrics, *i.e.*,  $(V_{GS}, V_{DS}) = (1.0V, 0.1V), (1.0V, 1.0V), (0.5V, 1.0V), (1.0V, 0.5V),$  and  $(0.0V, 1.0V)$ , in addition to linear ( $V_{DS} = 0.1V$ ) and saturation ( $V_{DS} = 1.0V$ ) threshold voltage values, were used to fit the analytical I-V model, for each case of + or – 10% variation in channel length (L), channel width (W), gate oxide thickness ( $T_{ox}$ ) or  $V_{TH}$ . Linear interpolation or extrapolation was then used to obtain the analytical I-V curves for arbitrary variations in L, W,  $T_{ox}$  and  $V_{TH}$ , which were then used to compute the SRAM metrics. L, W and  $T_{ox}$  are assumed to have Gaussian distribution (with 3-sigma corresponding to  $\pm 10\%$ ) while the standard deviation in  $V_{TH}$  due to random variations was determined as described in the next section.

### 2.2.2 Impact of Random Variations

The impacts of gate LER and RDF were evaluated via 3-D device and process simulations with atomistic doping profiles [7]. A scanning electron microscopy (SEM) image of photoresist lines processed for the 22 nm node was sampled 100 times to provide the realistic gate electrode profiles for 3-D device simulations. Thirty Kinetic Monte Carlo (KMC) simulations -- which account for reactions between defects and impurities as predicted by molecular dynamics -- were performed for each of these gate electrode profile cases. The source/drain extensions in the planar bulk structure are formed by dopant ion implantation; the resultant defects result in larger  $I_{dsat}$  variation for the planar bulk structure. In contrast, the source/drain extensions in the FD-SOI structure are formed by dopant diffusion; because implant damage is avoided, less  $I_{dsat}$  variation (and smaller  $\sigma(V_{TH})$ ) is seen for the FD-SOI structure. The device simulation results are shown in **Fig. 2.3**. The impact of gate work function variations (WFV) can be significant for nanometer-scale MOSFETs. Based on [15],  $\sigma(V_{TH})$  due to WFV is estimated to be 12.4 mV for the pull-down transistors in the 22 nm-node SRAM cell. Under the assumption that WFV is statistically independent of gate LER and RDF [16], the total  $V_{TH}$  variation is calculated as follows:

$$\sigma(V_{TH})|_{Total, random} \approx \sqrt{\sigma(V_{TH})^2|_{LER} + \sigma(V_{TH})^2|_{RDF} + \sigma(V_{TH})^2|_{WFV}} \quad (1)$$

Due to reduced  $V_{TH}$  roll-off and light channel doping, the FD-SOI structure provides for smaller  $V_{TH}$  variation than the planar bulk structure:  $\sigma(V_{TH})|_{SOI} = 26$  mV *vs.*  $\sigma(V_{TH})|_{BULK} = 50$  mV. It also shows less lowering of the average value of  $V_{TH}$  due to less atomistic doping effects.

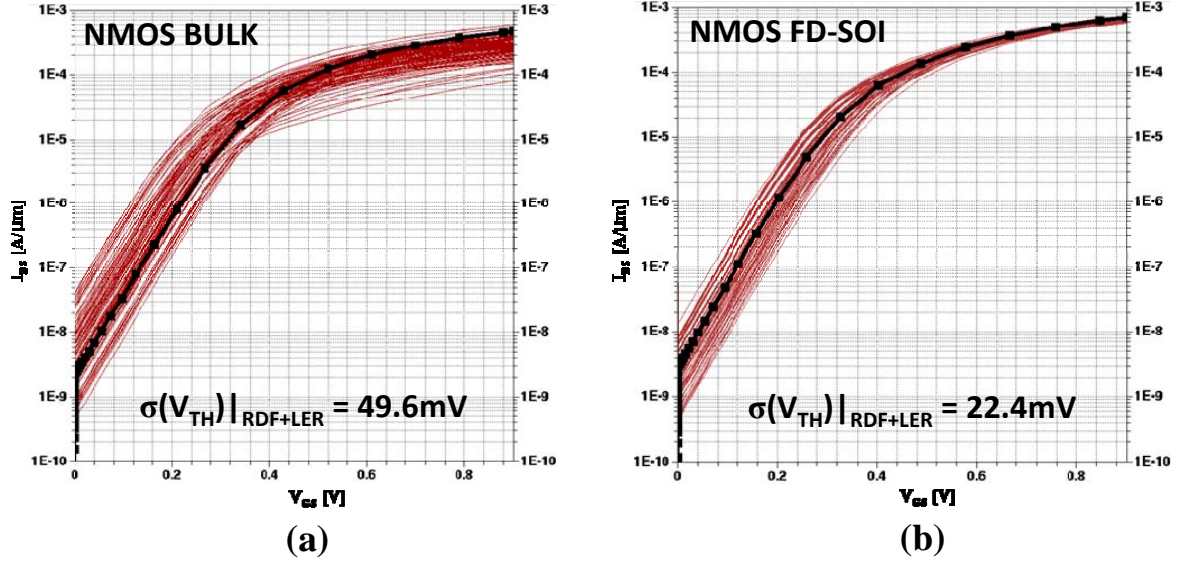
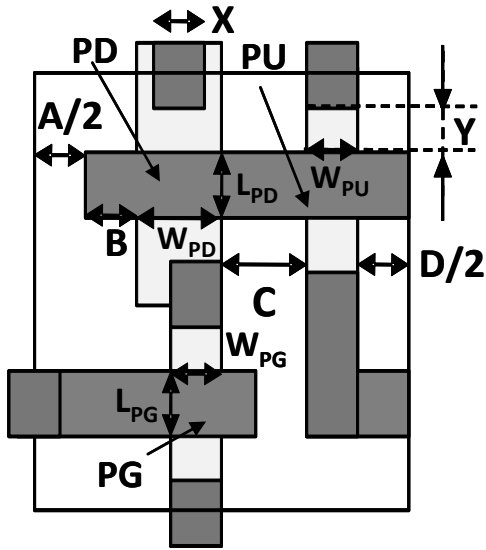


Figure 2.3. Simulated transfer characteristics of the pull-down transistor for 500 cases of gate-LER and atomistic doping: (a) Planar bulk MOSFET, (b) FD-SOI MOSFET.  $V_{DD} = 0.9$  V. The simulated transfer characteristics for continuum doping are also shown (with thicker lines) for reference.

## 2.3 6-T SRAM Cell Performance Comparison

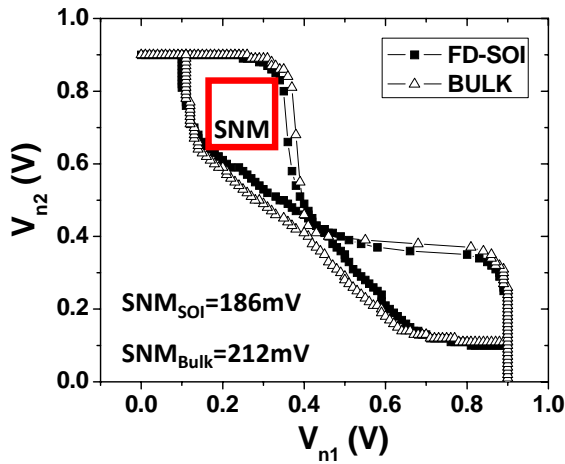
### 2.3.1 Nominal Cell Design

Based on recent publications [17-21], the dimensions for 22 nm-node 6-T SRAM cells were selected for this study. The cell layout parameters are summarized in **Table 2.3**. **Figs. 2.4a and 2.4b** show the butterfly plots and write-N curves, respectively, obtained using the analytical I-V model. Although the FD-SOI cell has slightly lower static noise margin (SNM) due to its lower switching voltage, it has higher write-ability ( $\sim 70\%$  higher  $I_w$ ) and Read-‘0’ current ( $\sim 60\%$  higher  $I_{read}$ ). Thus, the FD-SOI cell offers a better trade-off between read stability and write-ability, as compared to the planar bulk cell.

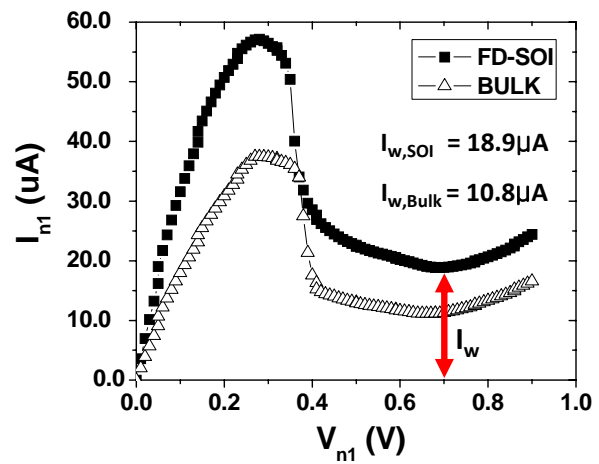


Design rules		Symbol	Size [nm]
Cell Height	PG CH length	$L_{PG}$	25
	PD CH length	$L_{PD}$	25
	CONT size	X	30
	Gate-to-CONT	Y	20
	Total	190	
Cell Width	POLY-to-POLY	A	30
	POLY-to-DIF ext	B	20
	PD Width	$W_{PD}$	55
	N/P isolation	C	50
	PU width	$W_{PU}$	32
	DIF-DIF (min)	D	50
	PG width	$W_{PG}$	35
Total		394	
A SRAM cell area		0.07486 $\mu m^2$	

Table 2.3. FD-SOI 6-T SRAM cell dimensions. A half-bit cell image is shown on the left side.



(a)



(b)

Figure 2.4. Comparisons of (a) SNM and (b) write current ( $I_w$ ), for  $V_{DD} = 0.9$  V. The write-ability of the FD-SOI SRAM cell is larger by 71%, but the SNM is lower by 10%.

### 2.3.2 Dependency of SRAM Performance Metrics on Cell Ratio, Pull-Up Ratio, and $V_{DD}$

For a fixed cell area, there is room to adjust the width of the pass-gate transistors ( $W_{PG}$ ) in order to optimize the trade-off between the various SRAM performance metrics (*i.e.*, SNM,  $I_w$ ,  $I_{read}$ ). This is because the SNM increases with increasing cell ( $\beta$ ) ratio ( $= W_{PD}/W_{PG}$ ), which decreases with increasing  $W_{PG}$ ;  $I_w$  increases with decreasing pull-up ( $\alpha$ ) ratio ( $= W_{PU}/W_{PG}$ ), which decreases with increasing  $W_{PG}$ ; and  $I_{read}$  increases directly with  $W_{PG}$ . **Figs. 2.5a, 2.5b, and 2.5c** show the dependencies of SNM,  $I_w$ , and  $I_{read}$  on cell ratio, pull-up ratio, and  $W_{PG}$ , respectively. The improved tradeoff between read stability and write-ability offered by the FD-SOI cell can be evaluated graphically using these figures. For example, the FD-SOI can achieve comparable SNM ( $\sim 212$  mV) as the planar bulk cell if  $W_{PG}$  is decreased to 27.2 nm (so that cell ratio  $= W_{PD}/W_{PG} = 55\text{nm}/27.2\text{nm} = 2.02$ , and pull-up ratio  $= W_{PU}/W_{PG} = 32\text{nm}/27.2\text{nm} = 1.18$ ), in which case  $I_w$  ( $\sim 12.4$   $\mu\text{A}$ ) is still 15% higher than that for the planar bulk cell ( $\sim 10.8$   $\mu\text{A}$ ) and  $I_{read}$  ( $\sim 15.5$   $\mu\text{A}$ ) is still 34% higher than that for the planar bulk cell (11.6  $\mu\text{A}$ ).

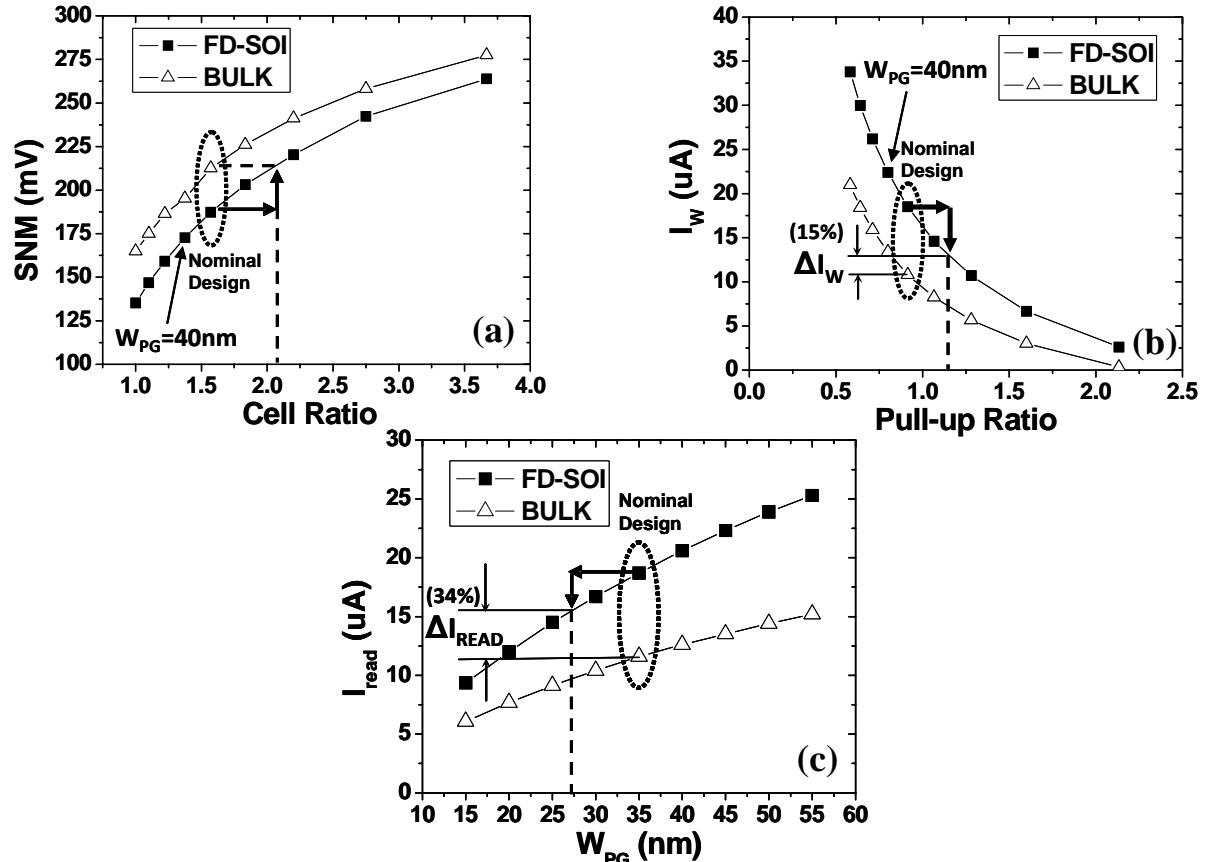


Figure 2.5. Comparison of cell performance metrics for FD-SOI vs. Planar bulk 6-T SRAM cells: (a) SNM, (b)  $I_w$ , and (c)  $I_{read}$ . (The curves are each obtained by adjusting the value of  $W_{PG}$ ).

**Fig. 2.6** compares the dependencies of SNM,  $I_w$ , and  $I_{\text{read}}$  on  $V_{DD}$  for this case (in which  $W_{PG}$  is reduced to 27.2 nm for the FD-SOI cell). The FD-SOI benefit of improved write-ability ( $I_w$ ) and speed ( $I_{\text{read}}$ ) for comparable read stability (SNM) is retained as  $V_{DD}$  is reduced.

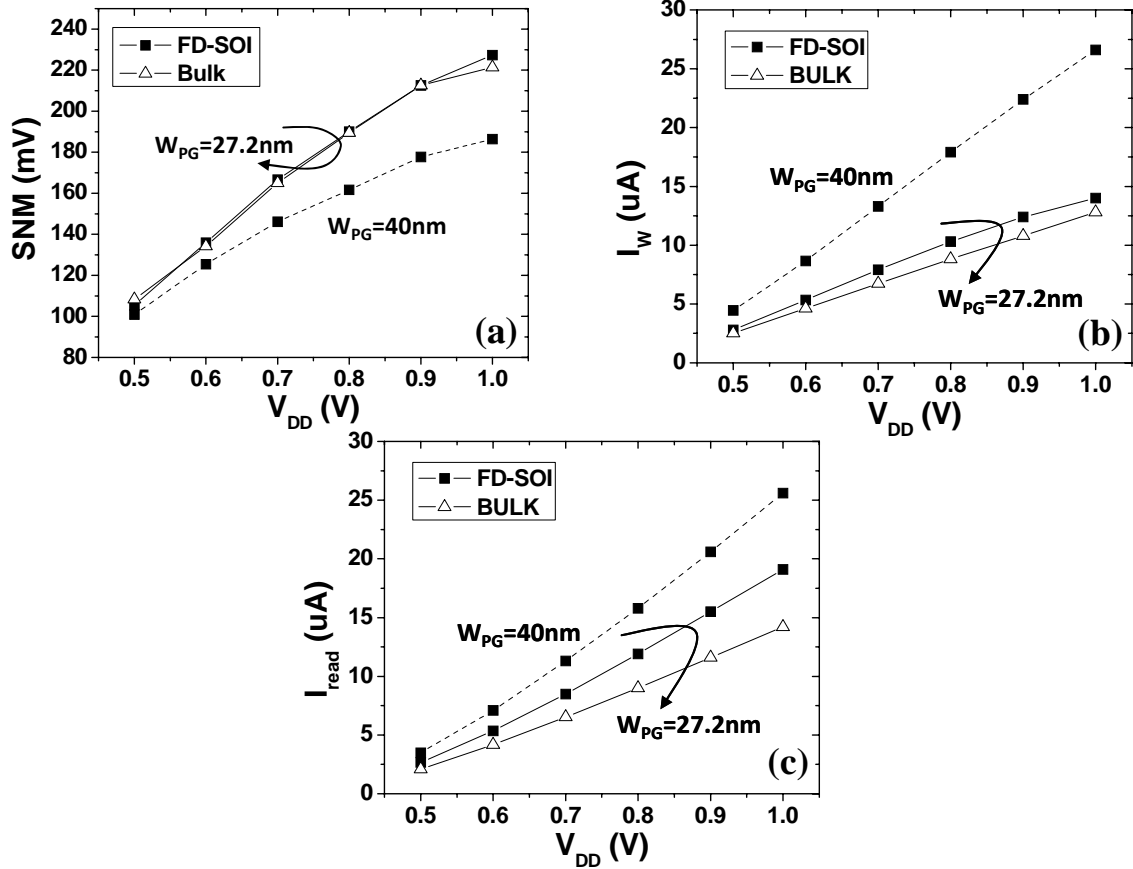


Figure 2.6. Impact of  $V_{DD}$  scaling on 6-T SRAM cell performance metrics: (a) SNM, (b)  $I_w$ , and (c)  $I_{\text{read}}$ .

## 2.4 Yield-Aware SRAM Cell Design

In the previous section, the FD-SOI cell was shown to offer improved trade-off between the nominal values of SNM and  $I_w$ , for fixed cell area. In this section, the corresponding improvement in cell yield is evaluated using the concept of cell sigma, defined as the minimum amount of variation for read/write failure [22]. Assuming that the metric (SNM or  $I_w$ ) has a Gaussian distribution, this is simply the mean divided by the standard deviation. If a metric “f” is subject to small, independent parameter variations “ $X_i$ ” in a range such that “f” can be approximated as a linear function of “ $X_i$ ” then the distribution of the metric is Gaussian, according to the Central Limit Theorem. The cell sigma is given by



$$cell\ sigma = \frac{f(0)}{\sqrt{\sum_i (\frac{\partial f}{\partial x_i})^2 \sigma_{x_i}^2}} \quad (2)$$

It should be noted that SNM and  $I_w$  each exhibit a linear response to small variations in  $X_i$ . Although their sensitivities can become non-linear for large variations (beyond several  $\sigma X_i$ ), the most probable combination of variations in  $L$ ,  $W$ ,  $T_{ox}$  and  $V_{TH}$  does not exceed  $\sim 4\sigma$  variation in a single parameter. Thus, this method of estimating SRAM yield is reasonably accurate [22].

As explained above, random variations due to gate LER and RDF, as well as global (Gaussian) variations due to process-induced variations ( $\pm 10\%$ ) in gate length, channel width, gate oxide thickness, and body thickness (**Fig. 2.1(b)**) are considered.

### 2.4.1 Iso-Area Comparison

In the future, six-sigma ( $6\sigma$ ) yield or larger will be required for large SRAM arrays to be functional. **Fig. 2.7** shows the trade-off between  $I_w$  yield and SNM yield for FD-SOI and planar bulk cells, for  $V_{DD} = 0.9V$ . ( $W_{PG}$  is varied along the curves.) In order for a cell design to meet the  $6\sigma$  yield requirement, both SNM and  $I_w$  must be able to tolerate at least 6 sigma variation. The FD-SOI cell can satisfy the  $6\sigma$  yield requirement, and achieves maximum cell sigma with  $W_{PG} = 40$  nm. Approximately 10 nm variation in  $W_{PG}$  can be tolerated, at this design point. In contrast, the planar bulk cell cannot satisfy the  $6\sigma$  yield requirement. The optimal planar bulk cell design corresponds to  $W_{PG} = 35$  nm, and has  $\sim 1.2\sigma$  worse SNM yield and  $\sim 2.2\sigma$  worse  $I_w$  yield than the FD-SOI cell.

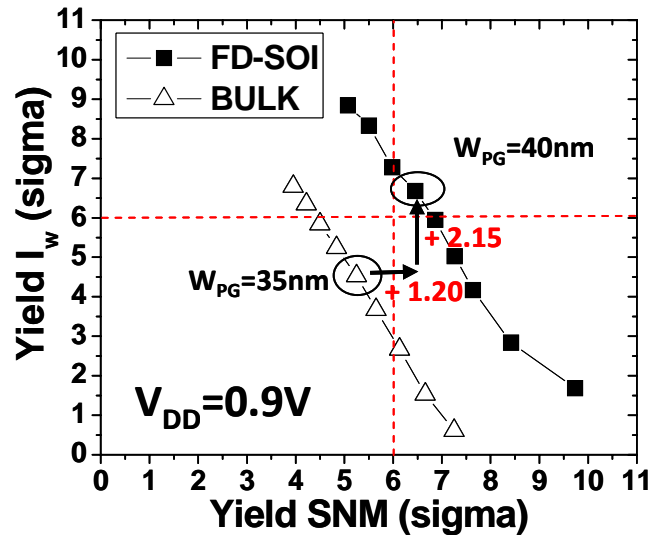


Figure 2.7. Yield of  $I_w$  vs. Yield of SNM. The optimal design points for planar bulk and FD-SOI cells are indicated (corresponding to  $W_{PG} = 35$  nm for the optimal planar bulk cell, and  $W_{PG} = 40$  nm for the optimal FD-SOI cell).

### 2.4.2 Iso-yield Comparison

In order for the planar bulk cell to achieve  $>6\sigma$  yield, comparable to that of the optimized FD-SOI cell (with  $W_{PG} = 40$  nm), the pull-down and pull-up transistor widths must be increased to  $W_{PD} = 95$  nm and  $W_{PU} = 50$  nm, respectively, so that the cell area is increased by  $\sim 30\%$  (from  $\sim 0.075 \mu m^2$  to  $\sim 0.1 \mu m^2$ ). In other words, the area savings offered by the FD-SOI cell is  $\sim 25\%$ . The resultant  $I_w$  yield vs. SNM yield curve is plotted in **Fig. 2.8**, along with the curves from **Fig. 2.7**. The spot-lighted design point corresponds to  $W_{PG} = 65$  nm.

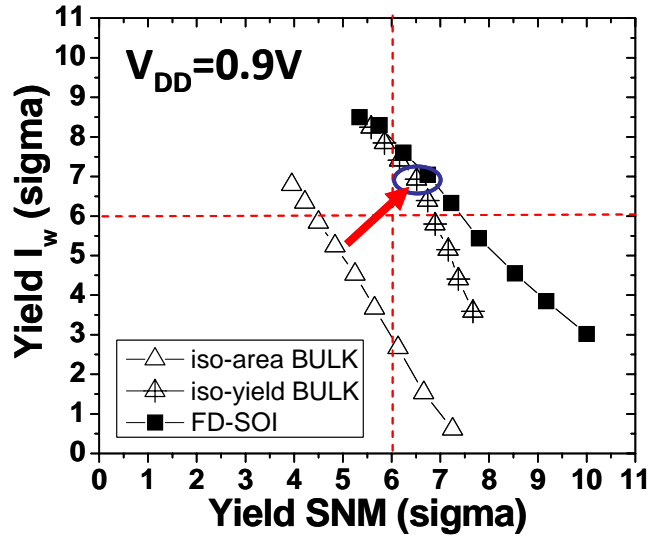


Figure 2.8. By up-sizing the planar bulk cell, yield that is comparable to that of the FD-SOI cell can be achieved. However, the trade-off between Yield of  $I_w$  and Yield of SNM is more severe for the planar bulk cell due to lower drive current and larger random  $V_{TH}$  variation.

### 2.4.3 Minimum Operating Voltage ( $V_{min}$ ) for read and write operation

By plotting  $I_w$  yield vs. SNM yield for various values of  $V_{DD}$ ,  $V_{min}$  can be estimated. **Figs. 2.9a and 2.9b** show the impact of  $V_{DD}$  reduction on yield, for the planar bulk and FD-SOI cells, respectively. At  $V_{DD} \sim 0.6V$  the FD-SOI cell can no longer meet the  $6\sigma$  criterion, *i.e.*,  $V_{min} \sim 0.6V$ . At  $V_{DD} \sim 0.8V$  the increased-area planar bulk cell can no longer meet the  $6\sigma$  criterion, *i.e.*,  $V_{min} \sim 0.8V$ . The FD-SOI cell achieves lower  $V_{min}$  because it provides for higher transistor drive current and reduced variability. **Table 2.4** summarizes the performance metrics of the FD-SOI and enlarged planar bulk SRAM cells at  $V_{min}$  and nominal  $V_{DD}$ .

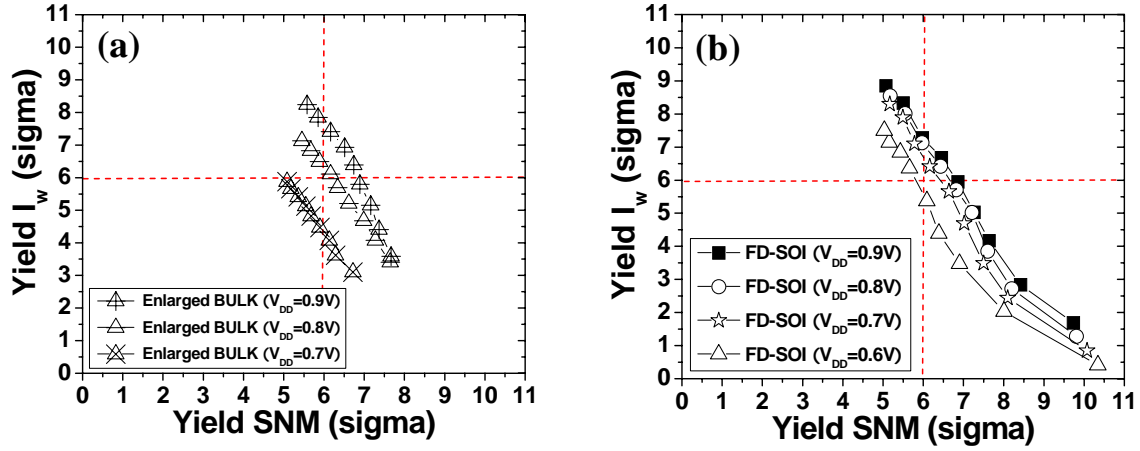


Figure 2.9. Dependence of yield on  $V_{DD}$ : (a) up-sized planar bulk cell (b) FD-SOI cell. At  $V_{DD} \sim 0.8V$ , the planar bulk cell cannot satisfy the  $6\sigma$  requirement, in contrast to the FD-SOI cell.  $V_{min}$  is significantly lower,  $\sim 0.6V$ , for the FD-SOI cell.

	FD-SOI SRAM cell		Enlarged Planar bulk SRAM cell	
Supply voltage	$V_{min} (= 0.6V)$	$V_{DD} (=0.9V)$	$V_{min} (= 0.8V)$	$V_{DD} (=0.9V)$
Cell area [ $\mu m^2$ ]	0.075	0.075	0.097	0.097
SNM [mV]	123	178	182	200
$I_w$ [ $\mu A$ ]	8.2	22.4	17.6	21.8
$I_{read}$ [ $\mu A$ ]	7.0	20.6	16.3	20.9
$W_{PG}$ [nm] for maximum yield	38	40	65	65

Table 2.4. Summary of SRAM cell performance metrics, for FD-SOI and enlarged planar bulk SRAM cells.

## 2.5 Summary

Thin-BOX FD-SOI and planar bulk CMOSFET designs were optimized via 3-D process and device simulations, for LOP CMOS technology at the 22 nm node. For the same  $I_{OFF}$ , the FD-SOI device achieves higher drive current and reduced random  $V_{TH}$  variation. Using an analytical model fit to the simulated I-V characteristics for the optimized device designs, 6-T SRAM cell performance metrics (SNM,  $I_w$ , and  $I_{read}$ ) were

estimated. For fixed cell area, FD-SOI technology was found to provide for improved SNM yield (by  $1.2\sigma$ ), and  $I_w$  yield (by  $2.2\sigma$ ). For fixed yield, the FD-SOI cell provides an area savings of  $\sim 25\%$ . The minimum operating voltage for  $6\sigma$  yield ( $V_{\min}$ ) is  $\sim 0.6V$  for the FD-SOI cell whereas it is  $>0.8V$  for the planar bulk cell. Thus, thin-BOX FD-SOI technology can facilitate the scaling of 6-T SRAM cell area and operating voltage. However, one practical drawback of FD-SOI technology is the higher cost of silicon-on-insulator (SOI) substrates. Therefore, in the subsequent chapters, a more cost-effective alternative transistor architecture will be discussed in detail.

## 2.6 References

- [1] K. J. Kuhn, "Reducing variation in advanced logic technologies: Approaches to process and design for manufacturability of nanoscale CMOS," *IEDM Tech. Dig.*, Dec. 2007, pp. 471–474.
- [2] A. Asenov, "Simulation of statistical variability in nano MOSFETs," *VLSI Symp. Tech. Dig.*, Jun. 2007, pp. 86–87.
- [3] T. Ohtou, N. Sugii, and T. Hiramoto, "Impact of parameter variations and random dopant fluctuations on short-channel fully depleted SOI MOSFETs with extremely thin BOX," *IEEE Electron Device Lett.*, vol. 28, no. 8, pp. 740–742, Aug. 2007.
- [4] C. Fenouillet-Beranger, S. Denorme, P. Perreau, C. Buj, O. Faynot, F. Andrieu, L. Tosti, S. Barnola, T. Salvetat, X. Garros, M. Casse, F. Allain, N. Loubet, L. Pham-Nguyen, E. Deloffre, M. Gros-Jean, R. Beneyton, C. Laviro, M. Marin, C. Leyris, S. Haendler, F. Leverd, P. Gouraud, P. Scheiblin, L. Clement, R. Pantel, S. Deleonibus, and T. Skotnicki, "FDSOI devices with thin BOX and ground plane integration for 32 nm node and below," *Solid State Electron.*, vol. 53, no. 7, pp. 730–734, Jul. 2009.
- [5] T.-J. K. Liu, C. Shin, M. H. Cho, X. Sun, B. Nikolić, and B.-Y. Nguyen, "SRAM cell design considerations for SOI technology," *Proc. IEEE Int. SOI Conf.*, Oct. 2009, pp. 1–4.
- [6] C. Shin, M. H. Cho, Y. Tsukamoto, B.-Y. Nguyen, B. Nikolić, and T.-J. K. Liu, "SRAM yield enhancement with thin-BOX FD-SOI," *Proc. IEEE Int. SOI Conf.*, Oct. 2009, pp. 1–2.
- [7] Sentaurus User's Manual, Synopsys, Inc., Mountain View, CA, 2009.06, Jun. 2009.
- [8] International Technology Roadmap for Semiconductors. [Online]. Available: <http://www.itrs.net>
- [9] A. K. Rashimi and G. A. Armstrong, "Insights into gate-underlap design in double gate based 6-T SRAM cell for low voltage applications," *Proc. IEEE Int. SOI Conf.*, Oct. 2008, pp. 61–62.
- [10] K. Cheng, A. Khakifirooz, P. Kulkarni, S. Kanakasabapathy, S. Schmitz, A. Reznicek, T. Adam, Y. Zhu, J. Li, J. Faltermeier, T. Furukawa, L. F. Edge, B. Haran, S.-C. Seo, P. Jamison, J. Holt, X. Li, R. Loesing, Z. Zhu, R. Johnson, A. Upham, T. Levin, M. Smalley, J. Herman, M. Di, J. Wang, D. Sadana, P. Kozlowski, H. Bu, B.

- Doris, and J. O'Neill, "Fully depleted extremely thin SOI technology fabricated by a novel integration scheme featuring implant-free, zero-silicon-loss, and faceted raised source/drain," *VLSI Symp. Tech. Dig.*, Jun. 2009, pp. 212–213.
- [11] Y. Taur and T. H. Ning, *Fundamentals of Modern VLSI Devices*. Cambridge, U.K.: Cambridge Univ. Press, 2006.
- [12] E. Seevinck, F. J. List, and J. Lohstroh, "Static-noise margin analysis of MOS SRAM cells," *IEEE J. Solid-State Circuits*, vol. SSC-22, no. 5, pp. 748–754, Oct. 1987.
- [13] C. Wann, R. Wong, D. J. Frank, R. Mann, S.-B. Ko, P. Croce, D. Lea, D. Hoyniak, Y.-M. Lee, J. Toomey, M. Weybright, and J. Sudijono, "SRAM cell design for stability methodology," *Proc. IEEE VLSI-TSA*, Apr. 2005, pp. 21–22.
- [14] E. Grossar, M. Stucchi, K. Maex, and W. Dehaene, "Read stability and write-ability analysis of SRAM cells for nanometer technologies," *IEEE J. Solid-State Circuits*, vol. 41, no. 11, pp. 2577–2588, Nov. 2006.
- [15] H. Dadgour, K. Endo, V. De, and K. Banerjee, "Modeling and analysis of grain-orientation effects in emerging metal-gate devices and implications for SRAM reliability," *IEDM Tech. Dig.*, Dec. 2008, pp. 705–708.
- [16] A. Cathignol, B. Cheng, D. Chanemougame, A. R. Brown, K. Rochereau, G. Ghibaudo, and A. Asenov, "Quantitative evaluation of statistical variability sources in a 45-nm technological node LP N-MOSFET," *IEEE Electron Device Lett.*, vol. 29, no. 6, pp. 609–611, Jun. 2008.
- [17] H. S. Yang, R. Wong, R. Hasumi, Y. Gao, N. S. Kim, D. H. Lee, S. Badrudduza, D. Nair, M. Ostermayr, H. Kang, H. Zhuang, J. Li, L. Kang, X. Chen, A. Thean, F. Arnaud, L. Zhuang, C. Schiller, D. P. Sun, Y. W. Teh, J. Wallner, Y. Takasu, K. Stein, S. Samavedam, D. Jaeger, C. V. Baiocco, M. Sherony, M. Khare, C. Lage, J. Pape, J. Sudijono, A. L. Steegen, and S. Stiffler, "Scaling of 32 nm low power SRAM with high-K metal gate," *IEDM Tech. Dig.*, 2008, pp. 233–236.
- [18] H. Kawasaki, M. Khater, M. Guillorn, N. Fuller, J. Chang, S. Kanakasabapathy, L. Chang, R. Muralidhar, K. Babich, Q. Yang, J. Ott, D. Klaus, E. Kratschmer, E. Sikorski, R. Miller, R. Viswanathan, Y. Zhang, J. Silverman, Q. Ouyang, A. Yagishita, M. Takayanagi, W. Haensch, and K. Ishimaru, "Demonstration of highly scaled FinFET SRAM cells with high-K/metal gate and investigation of characteristic variability for the 32 nm node and beyond," *IEDM Tech. Dig.*, 2008, pp. 237–240.
- [19] B. S. Haran, A. Kumar, L. Adam, J. Chang, V. Basker, S. Kanakasabapathy, D. Horak, S. Fan, J. Chen, J. Faltermeier, S. Seo, M. Burkhardt, S. Burns, S. Halle, S. Holmes, R. Johnson, E. McLellan, T. M. Levin, Y. Zhu, J. Kuss, A. Ebert, J. Cummings, D. Canaperi, S. Paparao, J. Arnold, T. Sparks, C. S. Koay, T. Kanarsky, S. Schmitz, K. Petrillo, R. H. Kim, J. Demarest, L. F. Edge, H. Jagannathan, M. Smalley, N. Berliner, K. Cheng, D. LaTulipe, C. Koburger, S. Mehta, M. Raymond, M. Colburn, T. Spooner, V. Paruchuri, W. Haensch, D. McHerron, and B. Doris, "22 nm technology compatible fully functional 0.1  $\mu\text{m}^2$  6T-SRAM cell," *IEDM Tech. Dig.*, 2008, pp. 625–628.
- [20] C. H. Diaz, K. Goto, H. T. Huang, Y. Yasuda, C. P. Tsao, T. T. Chu, W. T. Lu, V. Chang, Y. T. Hou, Y. S. Chao, P. F. Hsu, C. L. Chen, K. C. Lin, J. A. Ng, W. C. Yang, C. H. Chen, Y. H. Peng, C. J. Chen, C. C. Chen, M. H. Yu, L. Y. Yeh, K. S. You, K. S.

- Chen, K. B. Thei, C. H. Lee, S. H. Yang, J. Y. Cheng, K. Y. Huang, J. J. Liaw, Y. Ku, S. M. Jang, H. Chuang, and M. S. Liang, “32 nm gate-first high-k/metal gate technology for high performance low power applications,” *IEDM Tech. Dig.*, 2008, pp. 629–632.
- [21] F. Arnaud, J. Liu, Y. M. Lee, K. Y. Lim, S. Kohler, J. Chen, B. K. Moon, C. W. Lai, M. Lipinski, L. Sang, F. Guarin, C. Hobbs, P. Ferreira, K. Ohuchi, J. Li, H. Zhuang, P. Mora, Q. Zhang, D. R. Nair, D. H. Lee, K. K. Chan, S. Satadru, S. Yang, J. Koshy, W. Hayter, M. Zaleski, D. V. Coolbaugh, H.W. Kim, Y. C. Ee, J. Sudijono, A. Thean, M. Sherony, S. Samavedam, M. Khare, C. Goldberg, and A. Steegen, “32 nm general purpose bulk CMOS technology for high performance applications at low voltage,” *IEDM Tech. Dig.*, 2008, pp. 633–636.
- [22] A. E. Carlson, “Device and circuit techniques for reducing variation in nanoscale SRAM,” Ph.D. dissertation, Univ. California Berkeley, Berkeley, CA, May 2008.

## 2.A Appendix

The analytical MOSFET I-V model used to estimate SRAM performance metrics in this work is:

$$\begin{aligned}
 I_{DS} &= \mu_s C_{ox} \frac{W}{2mL} \frac{(V_{GS} - V_{TH})^2}{1 + \frac{V_{GS} - V_{TH}}{E_{sat} L}} (1 + \lambda V_{DS}) + I_{sub} (1 - e^{\frac{V_{DS}}{V_{TH}}}) & \text{if } V_{GS} > V_{TH} \text{ \& } V_{DS} \geq \frac{V_{GS} - V_{TH}}{m} \\
 &= \mu_l C_{ox} \frac{W}{L} \frac{V_{DS} (V_{GS} - V_{TH} - \frac{m V_{DS}}{V_0})}{1 + \frac{V_{GS} - V_{TH}}{E_{sat} L}} (1 + \lambda V_{DS}) + I_{sub} (1 - e^{\frac{V_{DS}}{V_{TH}}}) & \text{if } V_{GS} > V_{TH} \text{ \& } V_{DS} < \frac{V_{GS} - V_{TH}}{m} \quad \dots Eq.(1) \\
 &= I_{sub} (1 - e^{\frac{V_{DS}}{V_{TH}}}) e^{\frac{V_{GS} - V_{TH}}{S}} & \text{if } V_{GS} \leq V_{TH}
 \end{aligned}$$

where  $C_{ox}$  is the gate oxide capacitance per area,  $L$  is the gate length,  $W$  is the device width,  $I_{sub}$  is the current level corresponding to  $V_{TH}$ ,  $S$  is the sub-threshold swing, and  $V_{TH}$  is the threshold voltage which is dependent on drain bias ( $V_{TH} = V_{T0} - DIBL \times V_{DS}$ ).  $\mu_l$  and  $\mu_s$  are the carrier mobility values in the linear and saturation regimes of operation, respectively.  $V_0$  is defined as  $1/(1 - \mu_s/2\mu_l)$ .  $E_{sat}$  is the saturation electric field, which determines the amount of velocity saturation.  $m$  is a fitting parameter. As experimentally verified in [22], this model accurately captures planar bulk MOSFET short-channel effects and operation in the sub-threshold, linear, and saturation regimes. So long as the analytical I-V model can be well fit to the simulated (or measured) I-V data for FD-SOI devices, it can accurately represent their behavior as well.

## Chapter 3

# Study of Random Dopant Fluctuation (RDF) Effects for the Quasi-Planar Bulk MOSFET

### 3.1 Introduction

Threshold voltage ( $V_{TH}$ ) variation due to random dopant fluctuations (RDF) is already an issue for modern CMOS technologies [1], and will increase dramatically as MOSFET gate lengths are scaled below 30 nm [2]. To suppress  $V_{TH}$  variation due to RDF, light channel surface doping achieved via a retrograde or delta-shaped body doping profile [3] or a thin-body (fully depleted) transistor structure [4, 5] should be used. Improved electrostatic integrity, *e.g.*, via a reduction in equivalent gate oxide thickness (EOT) [6] or the use of a multiple-gate structure [7, 8], is beneficial for reducing the sensitivity of  $V_{TH}$  to channel length and hence for reducing RDF-induced  $V_{TH}$  variation as well. In this chapter, a modified atomistic simulation methodology [9] is used together with a commercial device simulator [10] to investigate the effects of randomly placed dopants in planar *vs.* quasi-planar bulk MOSFETs with 20 nm gate length ( $L_G$ ) and 20 nm layout width ( $W$ ). The effects of body RDF *vs.* source/drain RDF are elucidated.  $V_{TH}$ -adjustment approaches for the quasi-planar bulk MOSFET structure are compared with regard to robustness to RDF.

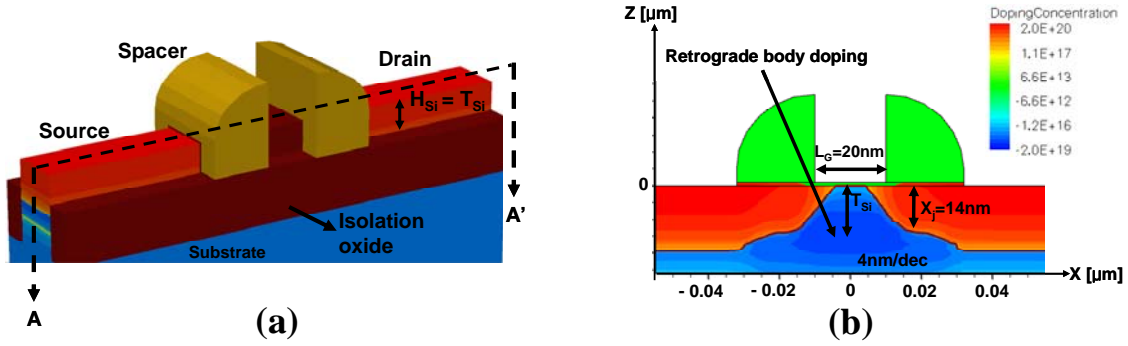


Figure 3.1. (a) 3D bird-eye view of the quasi-planar bulk MOSFET structure. The gate stack is not shown, in order to allow the channel region to be seen. (b) Cross-sectional view along the A-A' line.

## 3.2 Device Simulation Approach

### 3.2.1 Nominal Bulk MOSFET Designs

Based on the International Technology Roadmap for Semiconductors (ITRS) specifications, the nominal planar bulk MOSFET design is optimized using three-dimensional (3D) device simulations with continuum doping profiles, by selecting the electrical channel length ( $L_{eff}$ , defined as the distance between the points where the source/drain doping profiles fall to  $2 \times 10^{19} \text{ cm}^{-3}$ ), retrograde body doping peak depth ( $T_{Si}$ ), and source/drain-extension (SDE) junction depth ( $X_J$ ) to achieve maximum drive current for an effective oxide thickness (EOT) of 9 Å, gate work function ( $\Phi_M$ ) of 4.08 eV (n+ poly-Si), and an off-state leakage current specification of 5 nA/ $\mu\text{m}$  at 1 V supply voltage ( $V_{DD}$ ). The vertical retrograde body and lateral SDE doping gradients are 4 nm/dec and 2 nm/dec, respectively. The parameters for the optimized design are  $L_{eff} = 20 \text{ nm}$ ,  $T_{Si} = 14 \text{ nm}$ , and  $X_J = 14 \text{ nm}$ .

**Fig. 3.1** illustrates the nominal quasi-planar bulk MOSFET design. The physical height ( $H_{Si}$ ) of the gated channel above the isolation-oxide surface is equal to  $T_{Si}$  to achieve the best performance [11], so that the physical channel width is 48 nm ( $W + 2H_{Si}$ ). Note that the electrical effective channel width ( $W_{eff}$ ) is actually smaller (by ~8 nm) than this, because the retrograde body doping profile is not perfectly abrupt.  $\Phi_M$  is set to 4.35 eV for the quasi-planar device design to achieve the same linear  $V_{TH}$  (0.34 V at  $V_{DS} = 0.1 \text{ V}$ ).

### 3.2.2 Methodology for Atomistic Device Simulation

The methodology described in [9] was used to generate atomistic body- and SDE-doping profiles for 3D device simulation as follows. First, a pseudo-lattice structure in



which each grid point represents a silicon atom is generated to represent the body and SDE regions. In other words, regions to be atomistically simulated are converted to cubic grids with the silicon lattice spacing. Then, the nominal doping profile information is used to calculate the probability of finding a dopant atom at each lattice site ( $P_{\text{RDF}}$ ). For each atomistic doping profile, a random probability following a uniform distribution ( $P_{\text{rand}}$ ) is generated for each lattice site, and a dopant atom is placed at every lattice site for which  $P_{\text{RDF}} > P_{\text{rand}}$ . The effective dopant concentration at each simulation mesh point is then calculated as follows. Rather than using a point charge definition of an ionized dopant atom, which would result in unrealistic singularities in potential and charge density, we followed the methodology of Sano et al. [12, 13] to model the “influence” of an ionized dopant atom, which decays as  $1/r$ , where  $r$  is the radial distance from the center of the atom. Also, we used the long-range potential of a conduction electron in the silicon lattice to derive a corresponding charge density:

$$\rho(r) = \frac{qk_c^3 \{ \sin(k_c r) - (k_c r) \cos(k_c r) \}}{2\pi^2 (k_c r)^3} \quad (1)$$

where  $k_c$  is the inverse screen length or the inverse of the Debye length. For each randomly placed dopant atom, the distances to its eight nearest simulation mesh points are computed and the effective doping density contributed by the ionized dopant atom at these points is calculated using the long-range potential charge density [13]. This appropriately weights the influence of each ionized dopant atom at each simulation mesh point. Finally, an ASCII file containing the total doping density at each simulation mesh point is generated and exported to a commercial device simulator [10] for I-V simulation. An example of a quasi-planar bulk MOSFET structure with atomistic doping profiles is shown in **Fig. 3.2**. The sequence of random dopant placement and I-V simulation with advanced physical models including the density gradient model and drift-diffusion transport model [10] was iterated 200 times for each device design, in order to obtain meaningful  $V_{\text{TH}}$  statistics.

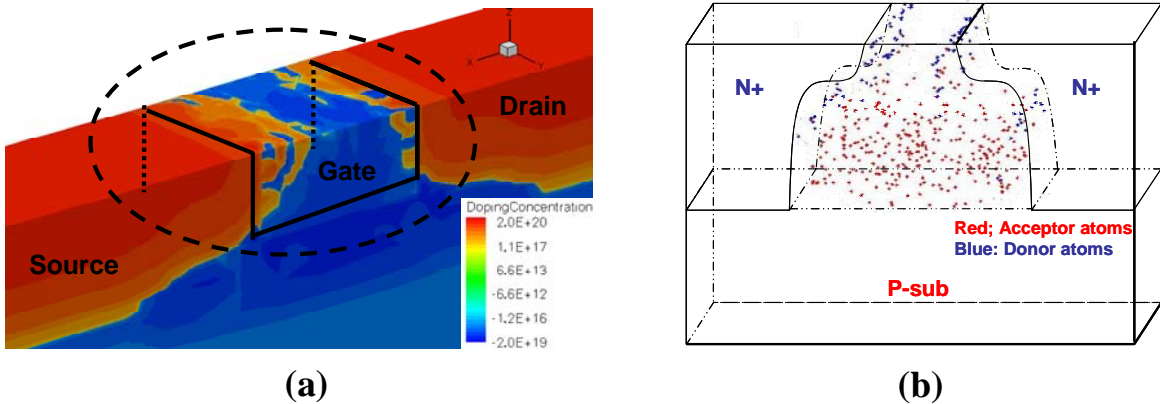


Figure 3.2. (a) Example of a quasi-planar bulk MOSFET with atomistic doping profiles. (b) Isometric view of the same quasi-planar bulk MOSFET, showing the randomly placed dopant atoms.

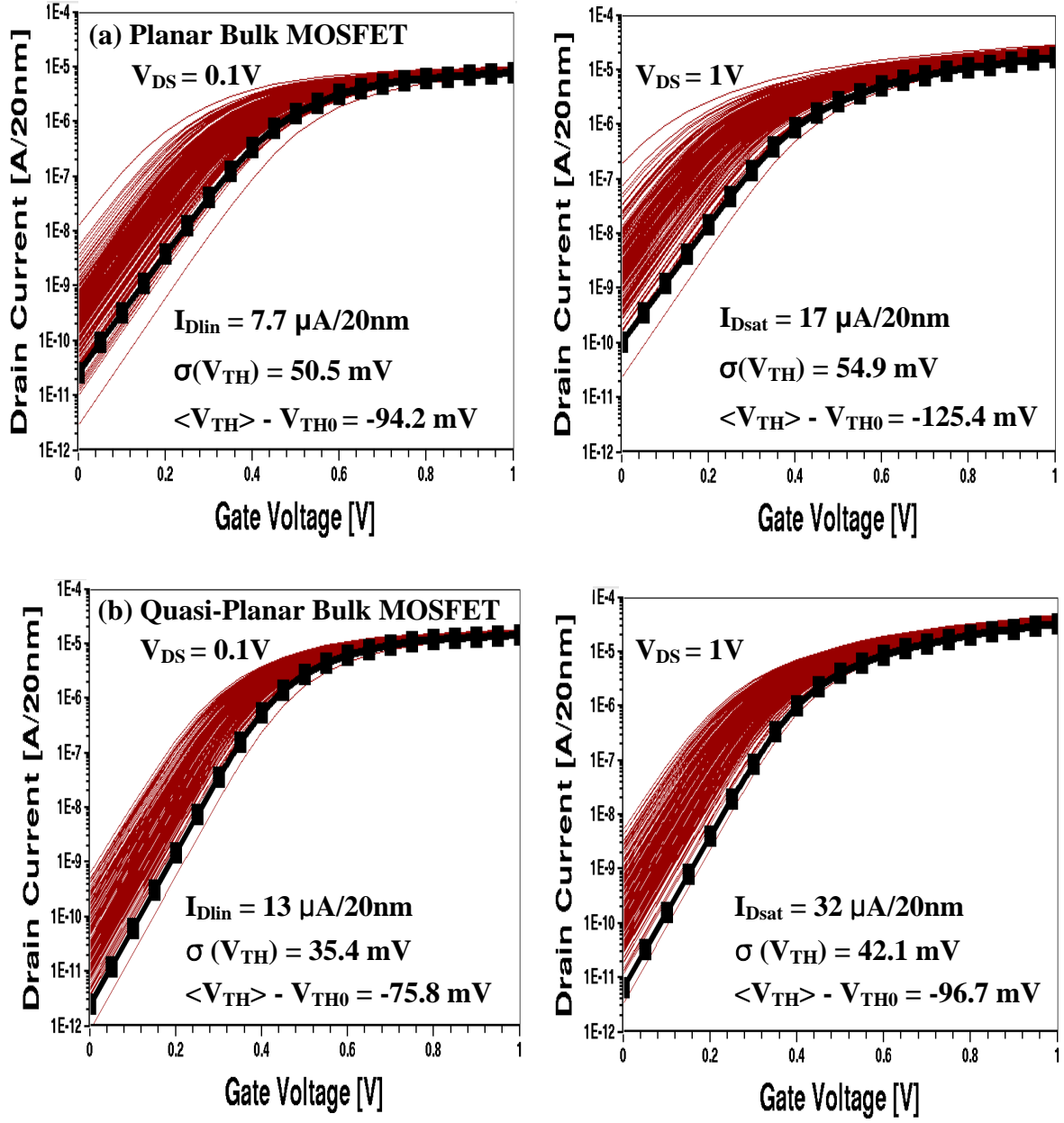


Figure 3.3. Simulated  $I_D$ - $V_{GS}$  curves for bulk MOSFETs with atomistic body and source/drain doping profiles (200 cases each): (a) planar device design, and (b) quasi-planar device design. The thick square-dotted solid curves show the simulated  $I_D$ - $V_{GS}$  curves obtained for continuum doping profiles. Note that the  $I_D$  values are for devices with 20nm layout width. It took approximately 30 minutes for each  $I_D$ - $V_{GS}$  curve simulation on an AMD64 machine with 8Gbit memory.

### 3.3. Results and Discussion

#### 3.3.1 Planar vs. Quasi-Planar Bulk MOSFET Designs

Simulated  $I_D$ - $V_{GS}$  curves for planar and quasi-planar MOSFETs with atomistic doping profiles are shown in **Fig. 3.3** [14]. For reference, the curves obtained for the same devices with continuum doping profiles are also plotted. It can be seen that the variation in off-state current is reduced by one order of magnitude for the quasi-planar device. The standard deviation of  $V_{TH}$  variation ( $\sigma(V_{TH})$ ) for the quasi-planar device is  $\sim 70\%$  that for the planar device, because the quasi-planar device has  $\sim 1.6\times$  larger  $W_{eff}$  (based on the ratio of  $I_{D,lin}$  values) and only slightly greater depletion charge due to its 3D channel geometry. This can be also explained by the following equation for  $\sigma(V_{TH})$  [15], which is derived below:

$$\sigma(V_{TH}) = \frac{\overline{Q_B}}{2C_{ox} \frac{W_{eff}}{W_{stripe}} \sqrt{W_{stripe} L_{eff} \overline{Q_B} / q}} \quad (2)$$

where  $C_{ox}$  is the areal gate capacitance,  $W_{stripe}$  is the layout width of a stripe, and  $\overline{Q_B}$  is the depletion charge per unit layout area.

$V_{TH}$  is given by the well-known equation  $V_{TH} = V_{FB} + 2\phi_B + \frac{Q_B}{C_{ox,total}}$ , where  $V_{FB}$  is the flat-band voltage,  $2\phi_B$  is the surface potential at the threshold condition,  $Q_B$  is the total depletion charge, and  $C_{ox,total}$  is the total gate capacitance. Noting that  $\delta Q_B / \delta N_a = Q_B / (2N_a)$  since  $Q_B \propto \sqrt{N_a}$ , it is derived from the above equation that  $\delta V_{TH} = \frac{\delta Q_B}{C_{ox,total}} = Q_B \frac{\delta N_a}{2N_a C_{ox,total}} = Q_B \frac{\delta n_a}{2n_a C_{ox,total}}$ , where  $N_a$  is the nominal doping concentration, and  $n_a$  is the number of dopant atoms, in the depletion region. It is assumed that the actual number of dopant atoms follows a normal distribution, so that  $\sigma(n_a) = \sqrt{n_a}$ . Considering that  $\overline{Q_B}$  is the depletion charge per unit layout area and  $C_{ox}$  is the areal gate capacitance,  $\sigma(V_{TH})$  for the quasi-planar bulk MOSFET is derived as follows.

$$\begin{aligned} \sigma(V_{TH}) &= Q_B \frac{\sigma(n_a)}{2n_a C_{ox,total}} = Q_B \frac{\sqrt{n_a}}{2n_a C_{ox,total}} = \frac{Q_B}{2C_{ox,total} \sqrt{n_a}} \\ &= \frac{\overline{Q_B} W_{stripe} L_{eff}}{2C_{ox} W_{eff} L_{eff} \sqrt{W_{stripe} L_{eff} \overline{Q_B} / q}} = \frac{\overline{Q_B}}{2C_{ox} \frac{W_{eff}}{W_{stripe}} \sqrt{W_{stripe} L_{eff} \overline{Q_B} / q}} \end{aligned}$$

Note that  $W_{eff} \cong W_{stripe}$  for the planar bulk MOSFET.

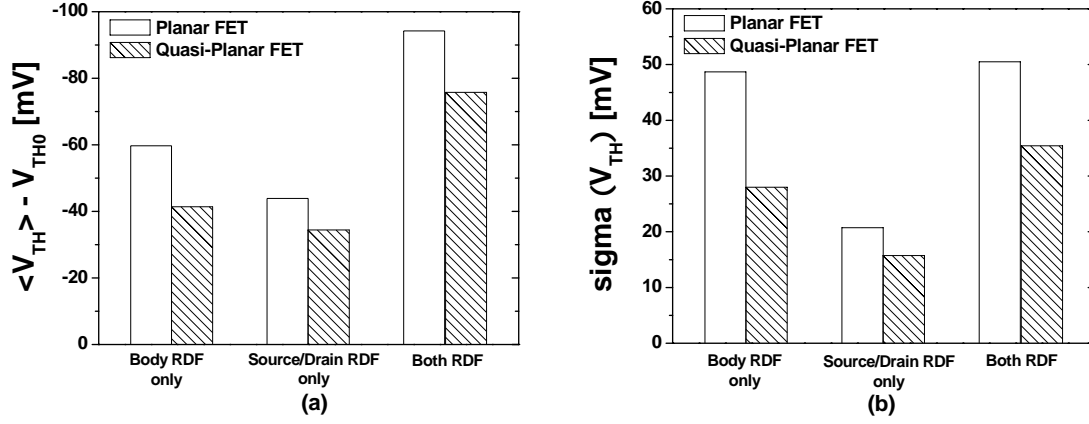


Figure 3.4. Comparison of body RDF vs. source/drain RDF effects on linear  $V_{TH}$  ( $V_{DS} = 0.1$  V): (a)  $V_{TH}$  lowering, (b)  $V_{TH}$  variation. Note that  $V_{TH}$  variation is reduced by ~30%, and that  $V_{TH}$  variation due to body RDF is relatively suppressed, for the quasi-planar FET.

### 3.3.2 Body RDF vs. Source/Drain RDF

To elucidate the impacts of body-RDF vs. source/drain-RDF, additional device simulations were performed with only atomistic body doping or only atomistic SDE doping (200 iterations for each case). From **Fig. 3.4**, it can be seen that both  $V_{TH}$  lowering and  $V_{TH}$  variation are dominated by body-RDF, because the position and number of dopant atoms in the body region are more important for determining  $V_{TH}$ . Therefore, precise control of the body doping profile is critical for reducing  $V_{TH}$  variation in bulk MOSFETs.

### 3.3.3 Assessment of $V_{TH}$ Adjustment Approaches

For the quasi-planar bulk MOSFET,  $V_{TH}$  can be adjusted by changing the body doping profile in two ways: by tuning its integrated dose, *i.e.*, its peak concentration ( $N_{peak}$ ), or its peak depth ( $T_{si}$ ). In order to compare the impacts of RDF for each  $V_{TH}$ -adjustment method, additional atomistic device simulations were performed for the quasi-planar bulk MOSFET structure with the body doping profile tuned to adjust  $V_{TH}$  either down to 0.15V or up to 0.4V (500 iterations for each  $V_{TH}$ , for each method). For the conventional method of dose adjustment,  $\sigma(V_{TH})$  increases with  $V_{TH}$  (**Fig. 3.5a**). In stark contrast, for the alternative method of  $T_{si}$  adjustment,  $\sigma(V_{TH})$  does not increase significantly with  $V_{TH}$  (**Fig. 3.5b**). This is expected based on **Eq. 2**, since the amount of depletion charge in the channel is increased significantly when  $N_{peak}$  is increased in order to increase  $V_{TH}$ . Note that  $W_{eff}$  decreases slightly with increasing  $N_{peak}$ , while  $L_{eff}$  increases. Calculated values of  $\sigma(V_{TH})$  using **Eq. 2** (with values for  $Q_B$  obtained by integrating the continuum retrograde body doping profile,

values for  $W_{\text{eff}}$  estimated from  $I_{D,\text{lin}}$ , and values for  $L_{\text{eff}}$  taken as the distance between the points where the source/drain doping profiles fall to  $2 \times 10^{19} \text{ cm}^{-3}$ ) were found to match the values of  $\sigma(V_{\text{TH}})$  obtained via atomistic simulation, to within 5%, for the range of  $N_{\text{peak}}$  values in **Fig. 3.5a**.  $\sigma(V_{\text{TH}})$  was found empirically (from the atomistic simulations) to be proportional to  $Q_B^{0.4}$  (rather than  $Q_B^{0.5}$  as in **Eq. 2**), consistent with findings in a previous study [3]. When instead  $T_{\text{si}}$  is decreased in order to increase  $V_{\text{TH}}$ , the increase in  $Q_B$  (and hence the increase in  $\sigma(V_{\text{TH}})$ ) is reduced.

For the conventional method, a tradeoff in short-channel control (increased drain-induced barrier lowering) is seen as  $N_{\text{peak}}$  is reduced to lower  $V_{\text{TH}}$  (**Fig. 3.5a**). For the alternative method, this tradeoff is less severe as  $T_{\text{si}}$  is increased to lower  $V_{\text{TH}}$  (**Fig. 3.5b**). Thus,  $V_{\text{TH}}$  adjustment via tuning of the retrograde body doping depth is advantageous for mitigating tradeoffs in  $V_{\text{TH}}$  variation and short-channel effect control. It should be noted that, for ease of process integration, a single value of  $H_{\text{si}}$  (achieved by uniform selective etching to recess the isolation oxide, or by uniform selective epitaxial growth to elevate the channel) can be used for both low- $V_{\text{TH}}$  and high- $V_{\text{TH}}$  quasi-planar bulk MOSFETs. That is, the physical height of the channel can be the same for all quasi-planar devices, while the depth of the retrograde body doping is tuned (*e.g.*, by adjusting the ion implantation energy) to adjust  $V_{\text{TH}}$  to minimize the trade-off in  $V_{\text{TH}}$  variation. Since this would result in  $H_{\text{si}} > T_{\text{si}}$  for the high- $V_{\text{TH}}$  devices, they would have proportionately larger intrinsic delay (due to larger gate-to-body capacitance); this should not present a serious issue, however, since high- $V_{\text{TH}}$  devices are not utilized in critical paths.

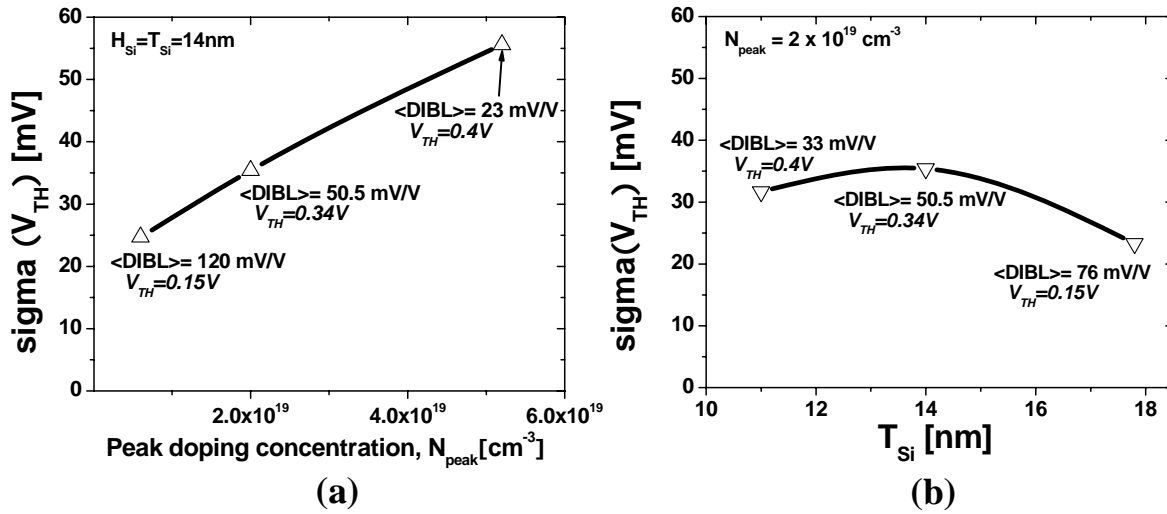


Figure 3.5. Impact of nominal  $V_{\text{TH}}$  adjustment on  $V_{\text{TH}}$  variation. (a) Conventional  $V_{\text{TH}}$ -adjustment method, with  $H_{\text{si}}$  and  $T_{\text{si}}$  each fixed at 14 nm. (b) Alternative  $V_{\text{TH}}$ -adjustment method, with  $N_{\text{peak}}$  fixed at  $2 \times 10^{19} \text{ cm}^{-3}$ . The average value of drain-induced barrier lower ( $\langle \text{DIBL} \rangle$ ) is indicated for each design point.  $\langle \text{DIBL} \rangle$  is tightly controlled within 100mV/V if the  $T_{\text{si}}$  adjustment method is used.

### 3.4 Summary

A study of random dopant fluctuation (RDF) effects on the quasi-planar bulk MOSFET vs. the planar bulk MOSFET is performed via atomistic three-dimensional device simulation, for devices with 20 nm gate length. The quasi-planar bulk MOSFET structure is more robust to RDF than a planar bulk MOSFET structure with identical nominal body and source/drain doping profiles and layout width. The effects of body RDF (vs. source/drain RDF) are dominant; hence, precise control of the body doping profile is critical for minimizing  $V_{TH}$  variation in a bulk MOSFET technology. The quasi-planar bulk MOSFET offers a new method of  $V_{TH}$  adjustment, via tuning of the retrograde body doping depth, to mitigate tradeoffs in  $V_{TH}$  variation and short-channel effect control.

### 3.5 References

- [1] K. Takeuchi, T. Fukai, T. Tsunomura, A. T. Putra, A. Nishida, S. Kamohara, and T. Hiramoto, "Understanding random threshold voltage fluctuation by comparing multiple fabs and technologies," *IEDM Tech. Dig.*, Dec. 2007, pp. 467–470.
- [2] A. Asenov, "Simulation of statistical variability in nano MOSFETs," *IEEE Symp. VLSI Technol., Dig. Tech. Papers*, Jun. 2007, pp. 86–87.
- [3] A. Asenov and S. Saini, "Suppression of random dopant-induced threshold voltage fluctuations in sub-0.1- $\mu$ m MOSFETs with epitaxial and  $\delta$ -doped channels," *IEEE Trans. Electron Devices*, vol. 46, no. 8, pp. 1718–1724, Aug. 1999.
- [4] T. Ohtou, N. Sugii, and T. Hiramoto, "Impact of parameter variations and random dopant fluctuations on short-channel fully depleted SOI MOSFETs with extremely thin BOX," *IEEE Electron Device Lett.*, vol. 28, no. 8, pp. 740–742, Aug. 2007.
- [5] K. Takeuchi, R. Koh, and T. Mogami, "A study of the threshold voltage variation for ultra-small bulk and SOI CMOS," *IEEE Trans. Electron Devices*, vol. 48, no. 9, pp. 1995–2001, Sep. 2001.
- [6] K. J. Kuhn, "Reducing variation in advanced logic technologies: Approaches to process and design for manufacturability of nanoscale CMOS," *IEDM Tech. Dig.*, Dec. 2007, pp. 471–474.
- [7] Y. Li and S.-M. Yu, "Comparison of random-dopant-induced threshold voltage fluctuation in nanoscale single-, double-, and surrounding gate field-effect transistors," *Jpn. J. Appl. Phys.*, vol. 45, no. 9A, pp. 6860–6865, Sep. 2006.
- [8] A. R. Brown, A. Asenov, and J. R. Watling, "Intrinsic fluctuations in sub 10-nm double-gate MOSFETs introduced by discreteness of charge and matter," *IEEE Trans. Electron Devices*, vol. 1, no. 4, pp. 195–200, Dec. 2002.
- [9] V. Varadarajan, L. Smith, S. Balasubramanian, and T.-J. King Liu, "Multigate FET design for tolerance to statistical dopant fluctuations," *Proc. Silicon Nanoelectronics Workshop*, Jun. 2006, pp. 137–138.
- [10] Sentaurus User's Manual, Synopsys, Inc., Mountain View, CA. v. 2006.12.

- [11] X. Sun, Q. Liu, V. Moroz, H. Takeuchi, G. Gebara, J. Wetzel, S. Ikeda, C. Shin, and T.-J. King Liu, "Tri-gate bulk MOSFET design for CMOS scaling to the end of the roadmap," *IEEE Electron Device Lett.*, vol. 29, no. 5, pp. 491–493, May 2008.
- [12] N. Sano, K. Matsuzawa, M. Mukai, and N. Nakayama, "Role of long range and short-range Coulomb potentials in threshold characteristics under discrete dopants in sub-0.1  $\mu\text{m}$  Si-MOSFETs," *IEDM Tech. Dig.*, Dec. 2000, pp. 275–278.
- [13] T. Ezaki, T. Ikezawa, A. Notsu, K. Tanaka, and M. Hane, "3D MOSFET simulation considering long-range Coulomb potential effects for analyzing statistical dopant-induced fluctuations associated with atomistic process simulator," *Proc. SISPAD*, Sep. 2002, pp. 87–90.
- [14] C. Shin, A. Carlson, X. Sun, K. Jeon, and T.-J. King Liu, "Tri-gate bulk MOSFET design for improved robustness to random dopant fluctuations," *IEEE Silicon Nanoelectronics Workshop*, Jun. 2008, pp. S1150.
- [15] T. Mizuno, J.-I. Okamura, and A. Toriumi, "Experimental study of threshold voltage fluctuation due to statistical variation of channel dopant number in MOSFETs," *IEEE Trans. Electron Devices*, vol. 41, no. 11, pp. 2216–2221, Nov. 1994.

## Chapter 4

# Full three-dimensional Simulation of 6-T SRAM Cells for the 22nm node

### 4.1 Introduction

A challenge for continued SRAM cell area scaling is threshold voltage ( $V_{TH}$ ) mismatch due to variability in transistor performance [1], which eventually degrades the minimum operating voltage of the SRAM array [2]. To suppress  $V_{TH}$  variation due to random dopant fluctuations (RDF) and process-induced variations in device parameters, light channel surface doping via a retrograde or delta-shaped body doping profile [3] or a fully-depleted ultra-thin-body/multi-gate architecture [4, 5] should be used. To avoid the need for expensive SOI substrates or more complex fabrication processes [6, 7], the segmented bulk MOSFET (SegFET) design was proposed to reduce  $V_{TH}$  variation [8, 9]. In this chapter, the benefits of SegFET technology for 6T-SRAM are assessed via full 3-dimensional (3D) cell simulation, in contrast to conventional mixed-mode (device-circuit) simulation, with regard to read stability, write-ability, cell yield, and susceptibility to single-event-upset (SEU).



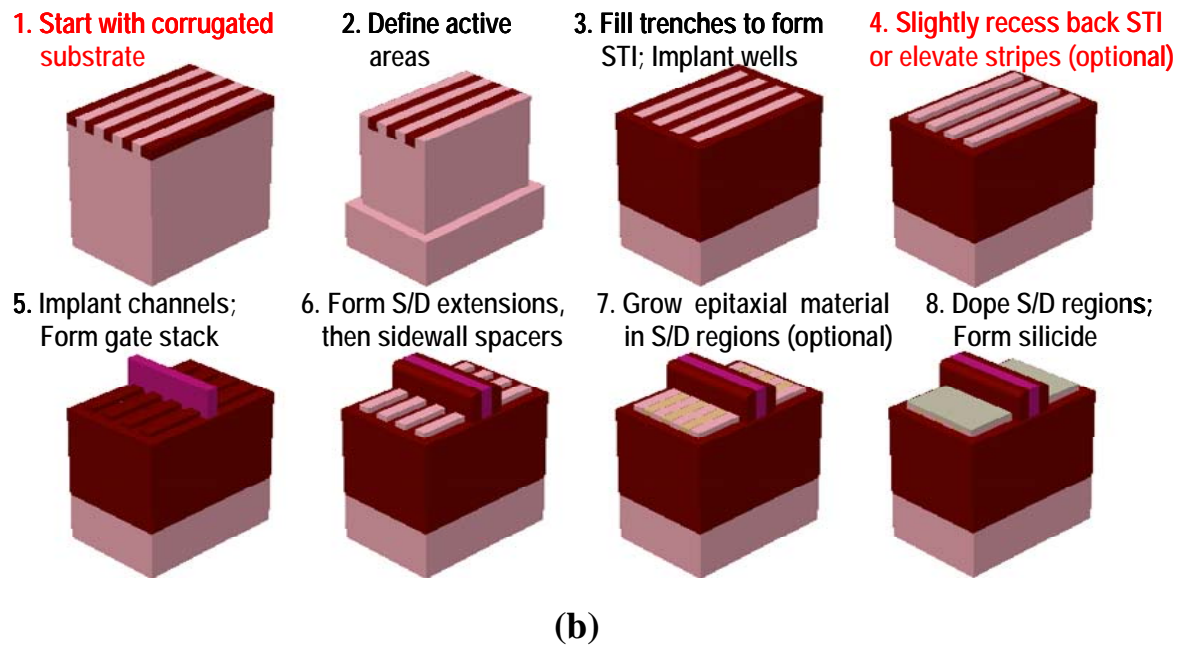
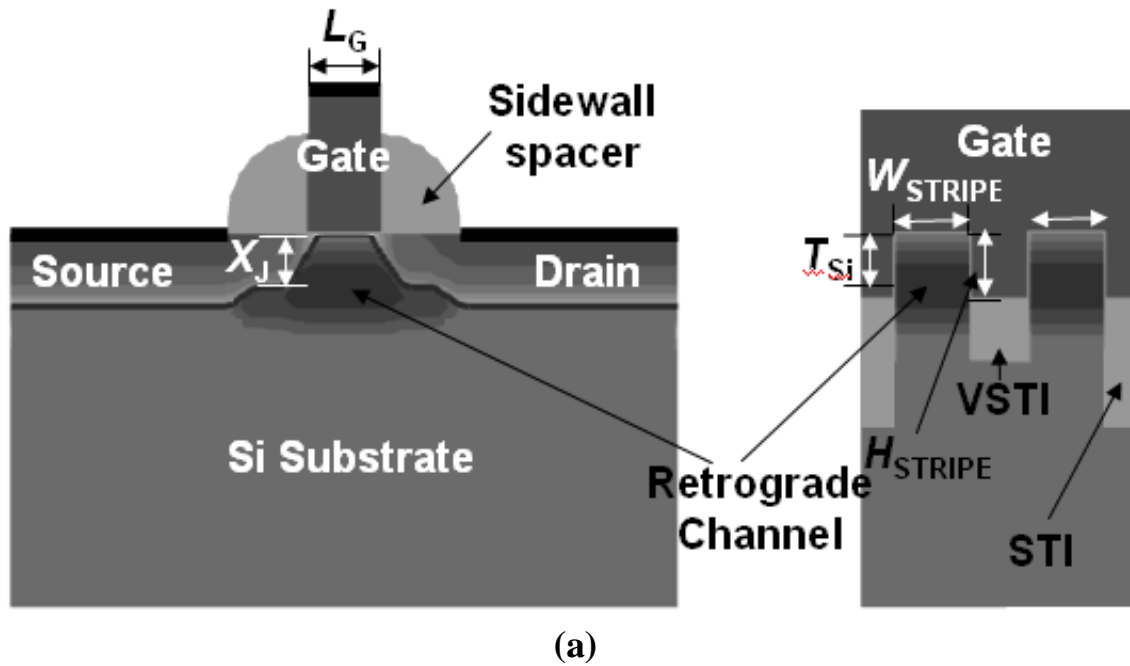


Figure 4.1. (a) Cross-sectional views of a two-stripped SegFET (used for the pull-down devices in the SegFET SRAM cell) along one stripe and across the channel, (b) Front-end-of-line fabrication process steps for a SegFET.

## 4.2 Segmented Bulk MOSFET Structure and Fabrication Process

The SegFET structure and front-end-of-line fabrication process steps are illustrated in **Fig. 4.1**. The channel is divided into stripes of equal width ( $W_{\text{STRIPE}}$ ), with very shallow trench isolation (VSTI) regions in-between the stripes. The VSTI depth should be deeper than the source/drain extension junction depth ( $X_j$ ) in order to fully suppress source-to-drain leakage current underneath the VSTI, but can be much shallower than the STI used to isolate transistors so that the channel stripes do not have a large aspect ratio. Within each stripe, the doping profiles are identical to those in a conventional planar bulk MOSFET (**Fig. 4.1a**). A quasi-planar structure is formed by recessing the VSTI by a small amount ( $H_{\text{STRIPE}}$ ) prior to gate stack formation; together with a retrograde channel doping profile (peaked at a depth  $T_{\text{si}}$ ), it provides for superior electrostatic integrity. The SegFET fabrication process (**Fig. 4.1b**) is identical to a conventional bulk MOSFET fabrication process, except that a corrugated substrate is used as the starting material. Since the features on the corrugated substrate are geometrically very regular, small-pitch and high-resolution patterning techniques such as multiple patterning or spacer lithography [11] can be readily used to achieve stripes of uniform width with very fine pitch. For improved layout area efficiency, the stripe spacing ( $W_{\text{SPACING}}$ ) can be less than  $W_{\text{STRIPE}}$ .

## 4.3 6-T SRAM Cell Designs

**Fig. 4.2** shows the scaling trend for 6T-SRAM cell area. Based on recent publications [12-16], the dimensions for 22nm-node cells (**Table 4.1**) were selected for this study.

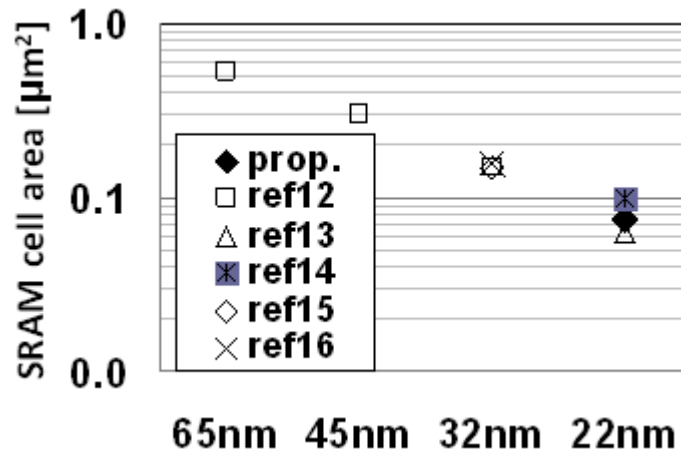


Figure 4.2. 6T-SRAM cell area scaling trend. The area of the proposed 22 nm node cell designs studied in this work is indicated.

Factor		symbol	Size
Height	PG Length	L <sub>a</sub>	0.025
	PD Length	L <sub>d</sub>	0.025
	CONT	X	0.030
	PO-CONT	Y	0.020
	<b>Total</b>		<b>0.190</b>
Width	PO-PO	A	0.030
	PO-DIF ext	B	0.020
	PD Width	W <sub>d</sub>	0.055
	N/P Isolation	C	0.050
	PU Width	W <sub>l</sub>	0.032
	DIF-DIF (min)	D	0.050
<b>Total</b>			<b>0.394</b>
<b>Cell Area</b>			<b>0.07486</b>

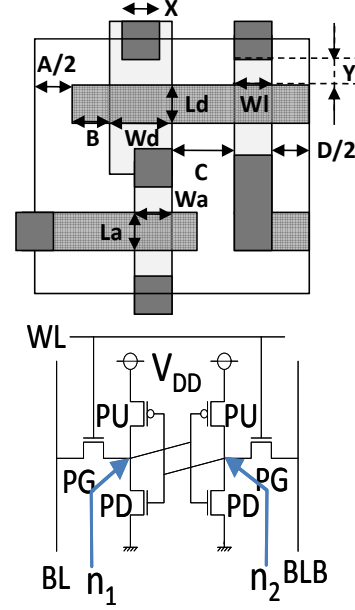


Table 4.1. SegFET 6T-SRAM cell dimensions for the 22nm node. The half-bit cell layout and 6T SRAM circuit schematic are shown to indicate the parameters designated in the table.

The pull-up ( $\alpha$ ) ratio and cell ( $\beta$ ) ratio of the SegFET SRAM cell design, with  $2 \times W_{\text{STRIPE}} = 40\text{nm}$ ,  $H_{\text{STRIPE}} = 10\text{nm}$ , and  $W_{\text{SPACING}} = 15\text{nm}$  for the pull-down devices, are comparable to those of the other SRAM cell designs. The gate-sidewall spacer width ( $\sim 10\text{nm}$ ), with an upper limit imposed by the gate-to-contact pitch, and the source/drain extension junction depth ( $\sim 10\text{nm}$ ) are each optimized to achieve good static noise margin (SNM) [17] and write-ability current ( $I_w$ ) [18]. To achieve the same  $V_{\text{TH,lin}}$  as for the planar devices, the gate work-function is set to  $4.3\text{eV}$  for the SegFETs. The SNM and  $I_w$  values for each cell design were obtained from full 3D simulations (**Fig. 4.3**) using advanced physical models including the density-gradient model and drift-diffusion transport model.

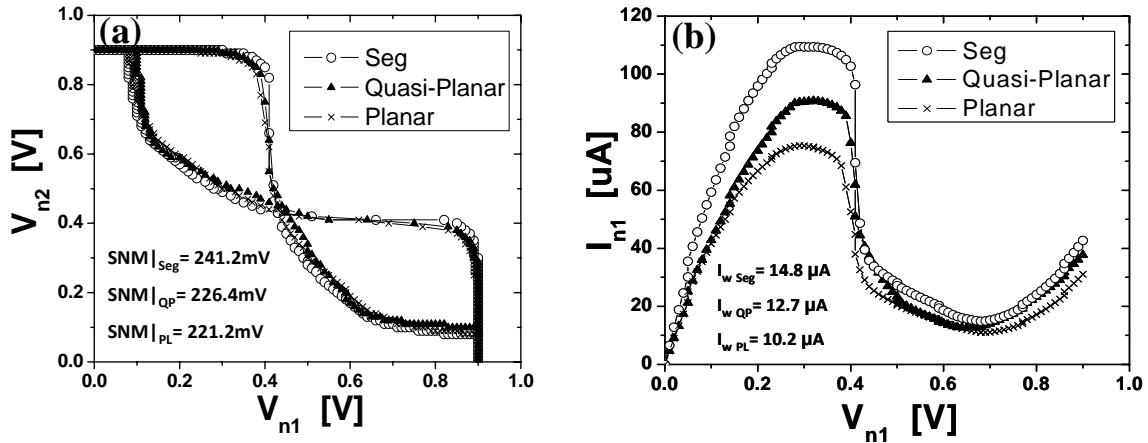


Figure 4.3. 3D 6-T SRAM cells simulation results: (a) butterfly plots and (b) write-N-curves for Planar, Quasi-Planar, and SegFET technologies. Each butterfly curve took  $\sim 6$  hrs to simulate using an AMD64 machine (8 cores).

**Fig. 4.4** shows the 3D 6T-SRAM cell structures used in this study. The STI oxide is not shown in (a)-(c) to allow the channel regions to be seen. The STI oxide and VSTI oxide in-between multiple stripes of the pull-down SegFETs are shown in (d).

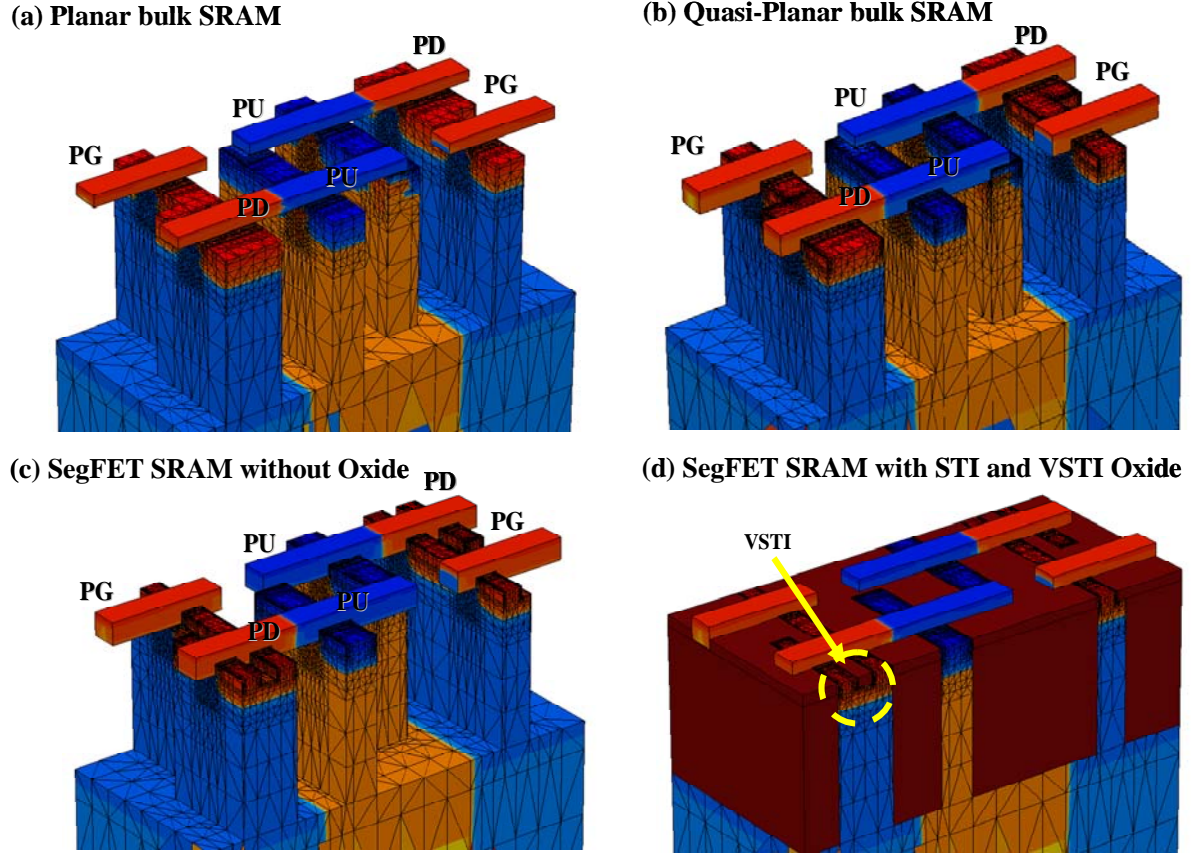


Figure 4.4. 3D 6T-SRAM cell structures with fine meshing ( $<1\text{nm}$ ) in the channel regions.

As shown in **Fig. 4.5**, the SegFET cell has the highest SNM across the entire range of  $V_{DD}$  values, and it is sufficient ( $\geq 0.2 \times V_{DD}$ ). The SNM at  $V_{DD} = 1.1\text{V}$  is smaller for the quasi-planar cell as compared to the planar cell due to a weaker body effect in the pass-gate devices [10].

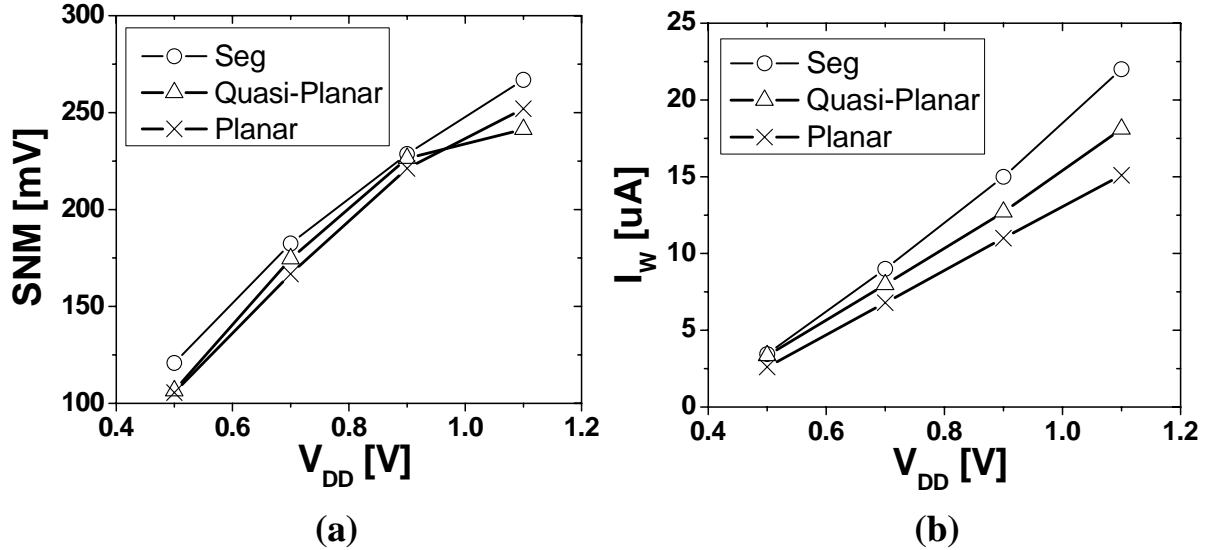


Figure 4.5. (a) SNM and (b)  $I_w$  vs.  $V_{DD}$ . The SegFET cell has higher SNM across the range of  $V_{DD}$ . The quasi-planar cell has better SNM at lower  $V_{DD}$  ( $<0.9V$ ), as compared to the planar cell.

## 4.4 Global and Local Variation Analysis

Due to its superior electrostatic integrity, the SegFET is more robust to global and local variations. **Figs. 4.6a and 4.6b** compare short-channel effects and narrow-width effects, respectively, for the SegFET vs. planar MOSFET structures. Variation due to RDF was evaluated via atomistic simulations [9]:  $\sigma(V_{TH}) \sim 25mV$  and  $28mV$  for n-channel and p-channel SegFET/quasi-planar devices, respectively;  $\sigma(V_{TH}) \sim 45mV$  and  $49mV$  for the n-channel and p-channel planar devices, respectively.

A sensitivity analysis was performed to assess the benefit of SegFET technology for improving SRAM cell yield using the concept of cell sigma, defined as the minimum amount of variation for read/write failure [10]. As shown in **Fig. 4.6c**, the SNM cell sigma for the SegFET cell is  $\sim 8$ , which is a 3-sigma improvement over the planar cell. The minimum  $V_{DD}$  that meets the six-sigma yield requirement for both SNM and  $I_w$  is  $\sim 0.75V$  for the SegFET cell. In stark contrast, the six-sigma yield requirement cannot be met by the planar cell for any value of  $V_{DD}$ ; it achieves only 5.5 SNM cell sigma at  $V_{DD} = 0.9V$ .

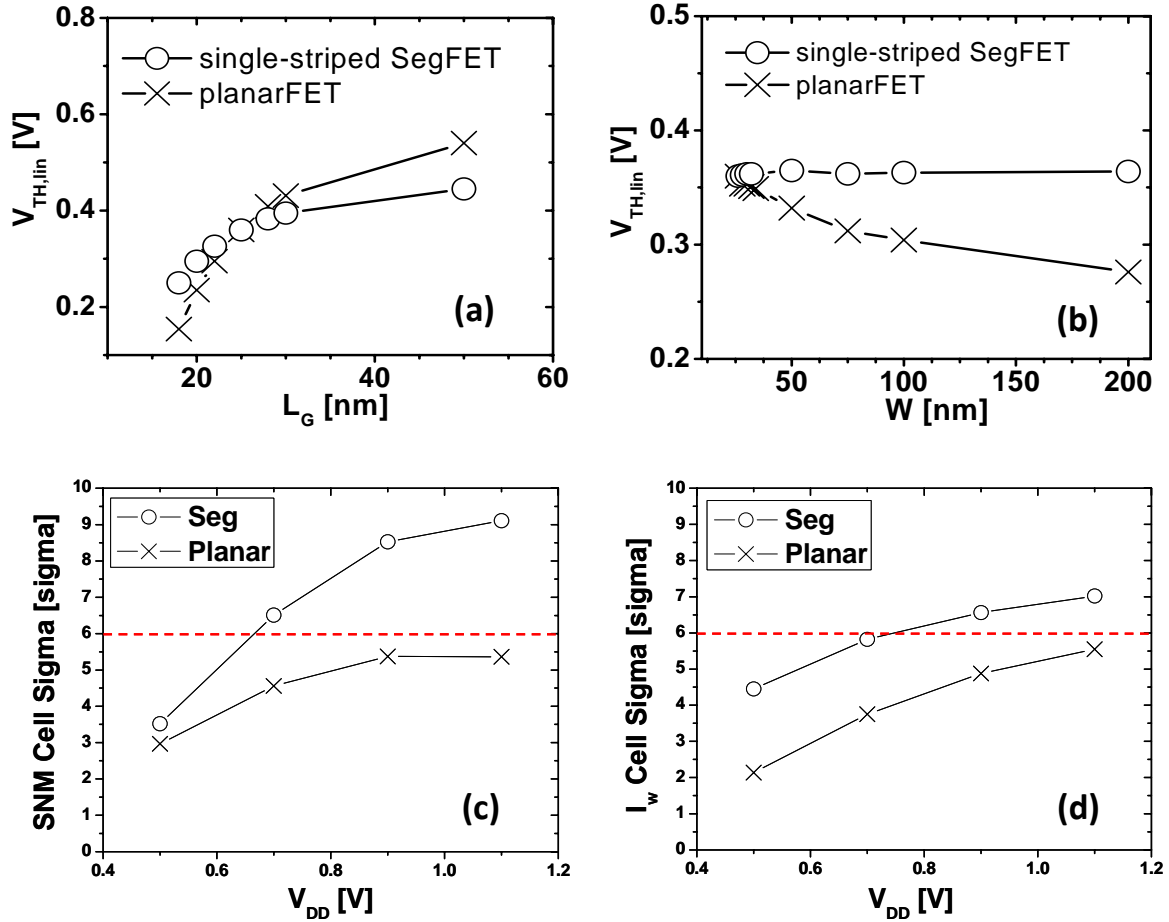


Figure 4.6. SegFET vs. planar MOSFET comparison: (a)  $V_{TH,lin}$  vs.  $L_g$  (b)  $V_{TH,lin}$  vs.  $W$  (c) SNM cell sigma (d)  $I_w$  cell sigma.

## 4.5 Simulation of Single-Event-Upset

SRAM cell soft-error tolerance was evaluated using an inverter model in [19]. The high (“1”) storage node is the region of the cell that is most sensitive to a particle strike, because the drain junction of the corresponding pull-down device is reverse-biased so that the probability of collecting generated electron-hole-pairs (EHPs) in the drain depletion region is relatively high. In this work, soft-error tolerance is studied via transient simulation of complete 3D 6T-SRAM structures. First, the cell is written and then the data is held. Then, a heavy ion beam (**Fig. 4.7**) is made to vertically impinge on the high (“1”) storage node at time  $t = t_{impact}$ , for each of the different SRAM cell designs. Due to the funneling effect [20], a parasitic thyristor turns on to short the drain node to the source node. This is evident in **Figs. 4.8a and 4.8b**, which show the high storage node ( $V_{n1}$ ) voltage being pulled down as a result of the particle strike, so that the low storage node ( $V_{n2}$ )

voltage is increased due to the SRAM cell's positive feedback. The simulation results indicate that the SegFET cell can withstand a particle strike with  $\sim 1.5\times$  larger linear energy transfer (LET) value ( $\sim 0.35\text{pC}/\mu\text{m}$  vs.  $\sim 0.24\text{pC}/\mu\text{m}$  for the planar cell) without data disturbance. This is because the SegFET cell has a stronger pull-up device (with  $\sim 40\%$  higher on current), slightly higher (by  $<10\%$ ) source/drain junction capacitance, and smaller body effect [8]. Based on the “rule of thumb” that the maximum LET (in  $\text{MeV}\cdot\text{cm}^2/\text{mg}$ ) of an ion beam is roughly equal to its atomic number  $Z$ , the SegFET cell is robust against much heavier particles ( $Z_{\text{max}} \sim 35$ ). Note that if the beam incidence angle is decreased to  $45^\circ$ , the threshold LET value is reduced by 5-10%.

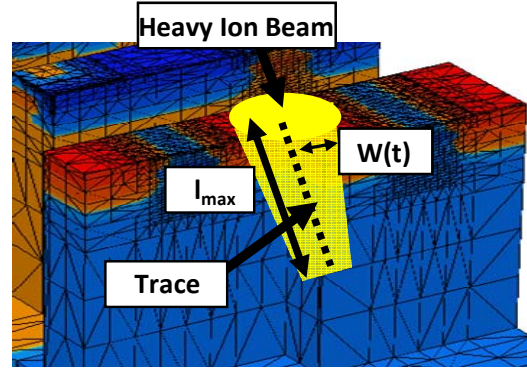


Figure 4.7. Heavy ion beam modeling. The Gaussian trace is characterized by the parameters  $l_{\text{max}}$  and  $w(t)$ . It is assumed that the trace is symmetric with respect to the track axis.

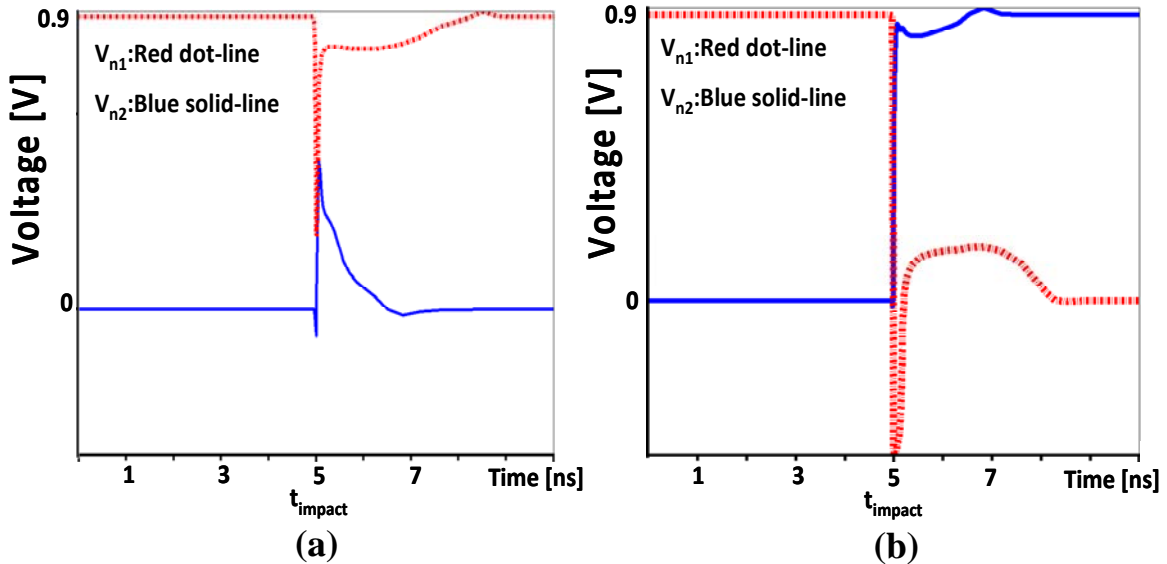


Figure 4.8. Transient simulations of heavy-ion-beam strike on the high storage node in (a) SegFET 6T-SRAM cell, and (b) planar 6T-SRAM cell.  $l_{\text{max}} = 1\mu\text{m}$ ,  $w(t) = 5\text{nm}$ , incidence angle =  $90^\circ$ .



## 4.6 Summary

Full 3D 6T-SRAM cell simulations are used to assess the benefits of advanced MOSFET structures at the 22nm node. Segmented MOSFET (SegFET) technology is projected to achieve enhanced read stability and write-ability, improved SRAM cell yield, and improved immunity to soft errors.

## 4.7 References

- [1] E. Josse, S. Parihar, O. Callen, P. Ferreira, C. Monget, A. Farcy, M. Zaleski, D. Villanueva, R. Ranica, M. Bidaud, D. Barge, C. Laviron, N. Auriac, C. Le Cam, S. Harrison, S. Warrick, F. Leverd, P. Gouraud, S. Zoll, F. Guyader, E. Perrin, E. Baylac, J. Belledent, B. Icard, B. Minghetti, S. Manakli, L. Pain, V. Huard, G. Ribes, K. Rochereau, S. Bordez, C. Blanc, A. Margain, D. Delille, R. Pantel, K. Barla, N. Cave, M. Haond, "A cost-effective low power platform for the 45-nm technology node," *IEDM Tech. Dig.*, Dec. 2006, pp. 1-4.
- [2] K. Nii, M. Yabuuchi, Y. Tsukamoto, S. Ohbayashi, Y. Oda, K. Usui, T. Kawamura, N. Tsuboi, T. Iwasaki, K. Hashimoto, H. Makino, and H. Shinohara, "A 45-nm single-port and dual-port SRAM family with robust read/write stabilizing circuitry under DVFS environment," *VLSI Symp. Circuit Dig.*, Jun. 2008, pp. 212-213.
- [3] A. Asenov, S. Saini, "Suppression of random dopant-induced threshold voltage fluctuations in sub-0.1- $\mu\text{m}$  MOSFET's with epitaxial and  $\delta$ -doped channels," *IEEE Trans. Electron Devices*, vol. 46, no. 8, pp. 1718-1724, Aug. 1999.
- [4] K. Takeuchi, R. Koh, T. Mogami, "A study of the threshold voltage variation for ultra-small bulk and SOI CMOS," *IEEE Trans. Electron Devices*, vol. 48, no. 9, pp. 1995-2001, Sep. 2001.
- [5] K. J. Kuhn, "Reducing variation in advanced logic technologies: Approaches to process and design for manufacturability of nanoscale CMOS," *IEDM Tech. Dig.*, Dec. 2007, pp. 471-474.
- [6] M. Jurczak, T. Skotnicki, M. Paoli, B. Tormen, J. Martin, J. L. Regolini, D. Dutartre, P. Ribot, D. Lenoble, R. Pantel, and S. Monfray, "Silicon-on-nothing (SON) – an innovative process for advanced CMOS," *IEEE Trans. Electron Devices*, vol. 47, no. 11, pp. 2179-2187, Nov. 2000.
- [7] T. Park, S. Choi, D. H. Lee, J. R. Yoo, B. C. Lee, J. Y. Kim, C. G. Lee, K. K. Chi, S. H. Hong, S. J. Hyun, Y. G. Shin, J. N. Han, I. S. Park, U. I. Chung, J. T. Moon, E. Yoon, and J. H. Lee, "Fabrication of body-tied FinFETs (Omega MOSFETs) using bulk Si wafers," *VLSI Symp. Tech. Dig.*, 2003, pp. 135-136.
- [8] X. Sun, Q. Liu, V. Moroz, H. Takeuchi, G. Gebara, J. Wetzel, S. Ikeda, C. Shin, and T.-J. King Liu, "Tri-gate bulk MOSFET design for CMOS scaling to the end of the roadmap," *IEEE Electron Device Lett.*, vol. 29, no. 5, pp. 491-493, May 2008.



- [9] C. Shin, A. Carlson, X. Sun, K. Jeon, and T.-J. King Liu, "Tri-gate bulk MOSFET design for improved robustness to random dopant fluctuations," *IEEE Silicon Nanoelectronics Workshop*, Jun. 2008, pp. 1-2.
- [10] A. Carlson, X. Sun, C. Shin, and T.-J. King Liu, "SRAM yield and performance enhancements with tri-gate bulk MOSFETs," *IEEE Silicon Nanoelectronics Workshop*, Jun. 2008, pp. 1-2.
- [11] Y.-K. Choi, T.-J. King, and C. Hu, "A spacer patterning technology for nanoscale CMOS," *IEEE Trans. Electron Devices*, vol. 49, no. 3, pp. 436-441, Mar. 2002.
- [12] H. S. Yang, R. Wong, R. Hasumi, Y. Gao, N. S. Kim, D. H. Lee, S. Badrudduza, D. Nair, M. Ostermayr, H. Kang, H. Zhuang, J. Li, L. Kang, X. Chen, A. Thean, F. Arnaud, L. Zhuang, C. Schiller, D. P. Sun, Y. W. Teh, J. Wallner, Y. Takasu, K. Stein, S. Samavedam, D. Jaeger, C. V. Baiocco, M. Sherony, M. Khare, C. Lage, J. Pape, J. Sudijono, A. L. Steegen, and S. Stiffler, "Scaling of 32nm low Power SRAM with high-K metal gate," *IEDM Tech. Dig.*, 2008, pp. 233-236.
- [13] H. Kawasaki, M. Khater, M. Guillorn, N. Fuller, J. Chang, S. Kanakasabapathy, L. Chang, R. Muralidhar, K. Babich, Q. Yang, J. Ott, D. Klaus, E. Kratschmer, E. Sikorski, R. Miller, R. Viswanathan, Y. Zhang, J. Silverman, Q. Ouyang, A. Yagishita, M. Takayanagi, W. Haensch, and K. Ishimaru, "Demonstration of highly scaled FinFET SRAM cells with high-K/metal gate and investigation of characteristic variability for the 32nm node and beyond," *IEDM Tech. Dig.*, 2008, pp. 237-240.
- [14] B. S. Haran, A. Kumar, L. Adam, J. Chang, V. Basker, S. Kanakasabapathy, D. Horak, S. Fan, J. Chen, J. Faltermeier, S. Seo, M. Burkhardt, S. Burns, S. Halle, S. Holmes, R. Johnson, E. McLellan, T. M. Levin, Y. Zhu, J. Kuss, A. Ebert, J. Cummings, D. Canaperi, S. Paparao, J. Arnold, T. Sparks, C. S. Koay, T. Kanarsky, S. Schmitz, K. Petrillo, R. H. Kim, J. Demarest, L. F. Edge, H. Jagannathan, M. Smalley, N. Berliner, K. Cheng, D. LaTulipe, C. Koburger, S. Mehta, M. Raymond, M. Colburn, T. Spooner, V. Paruchuri, W. Haensch, D. McHerron, and B. Doris, "22nm technology compatible fully functional  $0.1\mu\text{m}^2$  6T-SRAM cell," *IEDM Tech. Dig.*, 2008, pp. 625-628.
- [15] C. H. Diaz, K. Goto, H. T. Huang, Y. Yasuda, C. P. Tsao, T. T. Chu, W. T. Lu, V. Chang, Y. T. Hou, Y. S. Chao, P. F. Hsu, C. L. Chen, K. C. Lin, J. A. Ng, W. C. Yang, C. H. Chen, Y. H. Peng, C. J. Chen, C. C. Chen, M. H. Yu, L. Y. Yeh, K. S. You, K. S. Chen, K. B. Thei, C. H. Lee, S. H. Yang, J. Y. Cheng, K. Y. Huang, J. J. Liaw, Y. Ku, S. M. Jang, H. Chuang, and M. S. Liang, "32nm gate-first high-K/metal-gate technology for high performance low power applications," *IEDM Tech. Dig.*, 2008, pp. 629-632.
- [16] F. Arnaud, J. Liu, Y. M. Lee, K. Y. Lim, S. Kohler, J. Chen, B. K. Moon, C. W. Lai, M. Lipinski, L. Sang, F. Guarin, C. Hobbs, P. Ferreira, K. Ohuchi, J. Li, H. Zhuang, P. Mora, Q. Zhang, D. R. Nair, D. H. Lee, K. K. Chan, S. Satadru, S. Yang, J. Koshy, W. Hayter, M. Zaleski, D. V. Coolbaugh, H. W. Kim, Y. C. Ee, J. Sudijono, A. Thean, M. Sherony, S. Samavedam, M. Khare, C. Goldberg, and A. Steegen, "32nm general purpose bulk CMOS technology for high performance applications at low voltage," *IEDM Tech. Dig.*, 2008, pp. 633-636.
- [17] E. Seevinck, F. J. List, and J. Lohstroh, "Static-noise margin analysis of MOS SRAM cells," *Journal of Solid-State Circuits*, vol. 22, no. 5, pp. 748-754, Oct. 1987.

- [18] C. Wann, R. Wong, D. J. Frank, R. Mann, S.-B. Ko, P. Croce, D. Lea, D. Hoyniak, Y.-M. Lee, J. Toomey, M. Weybright, J. Sudijono, "SRAM cell design for stability methodology," *Proc. IEEE VLSI-TSA*, Apr. 2005, pp. 21–22.
- [19] K. Yamaguchi, Y. Takemura, K. Osada, K. Ishibashi, and Y. Saito, "3-D device modeling for SRAM soft-Error immunity and tolerance analysis," *IEEE Trans. Electron Devices*, vol. 51, no. 3, pp. 378-388, Mar. 2004.
- [20] K. Osada, K. Yamaguchi, Y. Saitoh, and T. Kawahara, "SRAM immunity to cosmic-ray-induced multierrors based on analysis of an induced parasitic bipolar effect," *Journal of Solid-State Circuits*, vol. 39, no. 5, pp. 827-833, May 2004.

## Chapter 5

# Quasi-Planar Bulk CMOS Technology for Improved SRAM Scalability

### 5.1 Introduction

Following Moore's Law, transistor density has roughly doubled with each new CMOS technology generation largely due to the steady miniaturization of the transistor. Variation in transistor threshold voltage ( $V_{TH}$ ) due to random dopant fluctuations and line-edge-roughness [1] and gate work-function variation [2] become more significant as the transistor gate length ( $L_G$ ) is reduced below 30nm, so that continued transistor scaling poses a growing challenge, particularly for static random-access memory (SRAM) arrays which typically employ the smallest transistors and have the most stringent yield requirement [3].  $V_{TH}$  mismatch makes it difficult to lower the SRAM operating voltage [4], so that increasing power density has become a critical issue. Therefore, an improved transistor design that provides for reduced short-channel effects (*i.e.*, improved gate control over the channel potential) and hence reduced  $V_{TH}$  sensitivity to process-induced variations is needed to facilitate voltage scaling. Examples include the fully depleted silicon-on-insulator (FD-SOI) MOSFET with thin buried-oxide (thin-BOX) [5] and multiple-gate transistor structures (*e.g.*, FinFET, MuGFET, Tri-Gate FET) [6]; but these require either expensive SOI substrates and/or more complex fabrication processes that pose significant barriers to their widespread adoption. Recently, a low-cost quasi-planar bulk CMOS technology was proposed and demonstrated to provide for improved performance and reduced variability [7, 8]. In contrast with FinFET/MuGFET/Tri-Gate FET structures which employ a narrow body region to suppress short-channel effects, the quasi-planar bulk MOSFET structure uses the conventional retrograde channel doping of the planar bulk

MOSFET structure to suppress leakage current, in addition to a quasi-planar gate electrode and gate fringing electric fields, to achieve improved gate control.

This chapter presents more details of the study of quasi-planar bulk CMOS technology for improved SRAM scalability [8]. In Section 5.2, the device fabrication process is described. In Section 5.3, the benefits of the quasi-planar MOSFET design for improving transistor performance and reducing variability to improve SRAM yield are presented. Section 5.4 presents the conclusions from this study.

## 5.2 Device Fabrication

(100) epi-Si wafers were used as the starting substrates for fabricating MOSFETs with  $\langle 110 \rangle$  channel orientation in an early 28nm-generation bulk CMOS logic technology. The sequence of front-end-of-line fabrication process steps is outlined in **Fig. 5.1**. After conventional shallow-trench-isolation (STI) processing, N/P well and  $V_{TH}$ -adjust ion implantation steps were performed, followed by high-temperature rapid thermal annealing (RTA). Subsequently, dilute hydrofluoric acid (DHF) was used to remove residual sacrificial oxide, as well as to recess the STI oxide by a small amount (15nm) prior to gate stack formation to achieve quasi-planar MOSFETs. A shorter DHF dip was used for the control (planar MOSFET) devices. The gate stack was formed by plasma nitridation of a thermal oxide layer of 1.45nm physical thickness followed by deposition of an undoped polycrystalline silicon layer of 70nm thickness. To define the gate electrodes with tight control of physical gate length (as small as 30nm) for logic transistors and  $0.149\mu\text{m}^2$  6-T SRAM bit cells, a double-patterning/double-etch (2P2E) process employing 193nm immersion lithography and advanced hard-mask etching techniques was used. After gate stack patterning, pocket ion implantation was performed. An experimental split was included to explore lighter pocket doping, in which the implant dose was lowered by  $10^{13}\text{cm}^{-2}$ . Gate-sidewall spacers were formed prior to source/drain ion implantation. To activate the implanted dopants, a rapid thermal process (RTP) followed by laser spike annealing (LSA) was used to enhance the electrical conductivity in the source/drain regions. Afterwards, a nickel silicidation (NiSi) process was applied. Subsequently, dual contact etch stop layers (CESL) of  $\text{SiN}_x$  -- highly compressive stress liner for PMOS devices, and highly tensile stress liner for NMOS devices -- for performance enhancement were formed by plasma-enhanced chemical vapor deposition (PECVD). After interlayer dielectric (ILD) oxide deposition, contact hole definition, tungsten plug formation and chemical mechanical planarization (CMP), a standard copper metal interconnection process was followed.

A standard test-chip mask set was used to fabricate individual logic transistors and 6T-SRAM arrays, ~2500 cells per device-under-test (DUT). **Fig. 5.2** shows plan-view

scanning electron microscopy and cross-sectional transmission electron microscopy images of a fabricated SRAM cell.

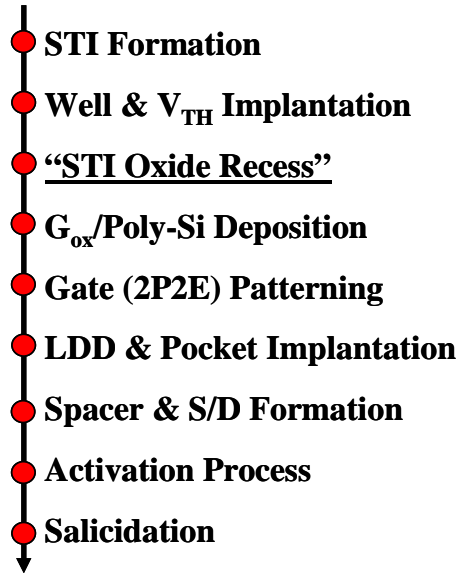


Figure 5.1. Sequence of front-end-of-line CMOS fabrication process steps used to fabricate logic devices and SRAM arrays in this work.

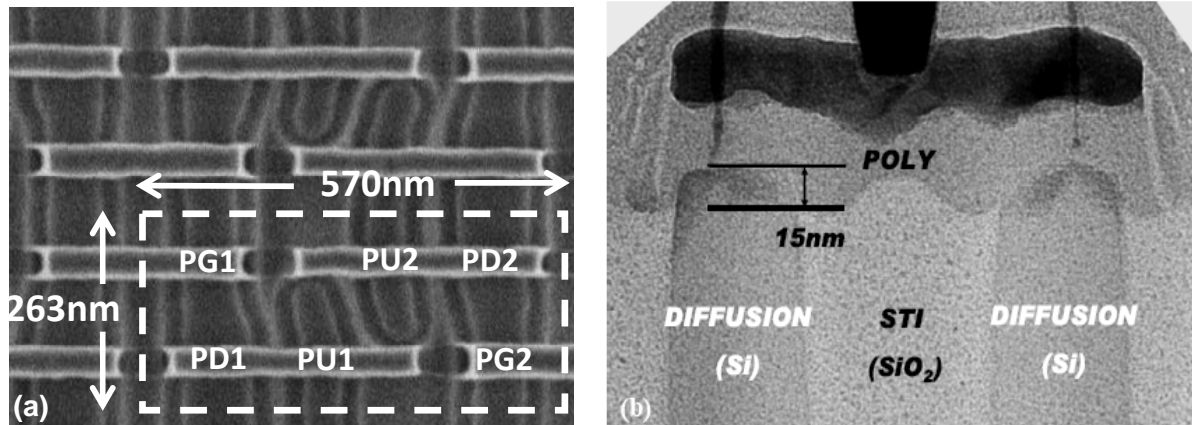


Figure 5.2. (a)  $0.149\mu m^2$  SRAM cell plan-view CDSEM image after gate patterning. (b) XTEM taken along a poly-Si gate electrode in an SRAM array, for 15nm nominal STI-oxide recess depth.

## 5.3 Results and Discussion

### 5.3.1 Quasi-Planar vs. Planar MOSFETs

#### 5.3.1.1 Improved Performance

Due to improved gate control and increased effective channel width, quasi-planar MOSFETs (in which the STI oxide is recessed by 15nm) have higher on-state drive current ( $I_{ON}$ ) for comparable off-state leakage current ( $I_{OFF}$ ), as shown in **Fig. 5.3**. Lower pocket doping results in lower  $V_{TH}$  as well as higher average effective mobility, and hence even higher  $I_{ON}$ . Because the benefit of sidewall gating increases as the layout width decreases, the pass-gate (PG) devices show greater improvement ( $2.4\times$ ) in  $I_{ON}$  than the pull-down (PD) devices ( $2.1\times$  improvement). The performance enhancement ( $4.5\times$ ) is greatest for the PMOS devices not only because they have the narrowest layout width and but also because hole mobility is higher for the (110) sidewall channel surfaces, whereas electron mobility is lower [9].

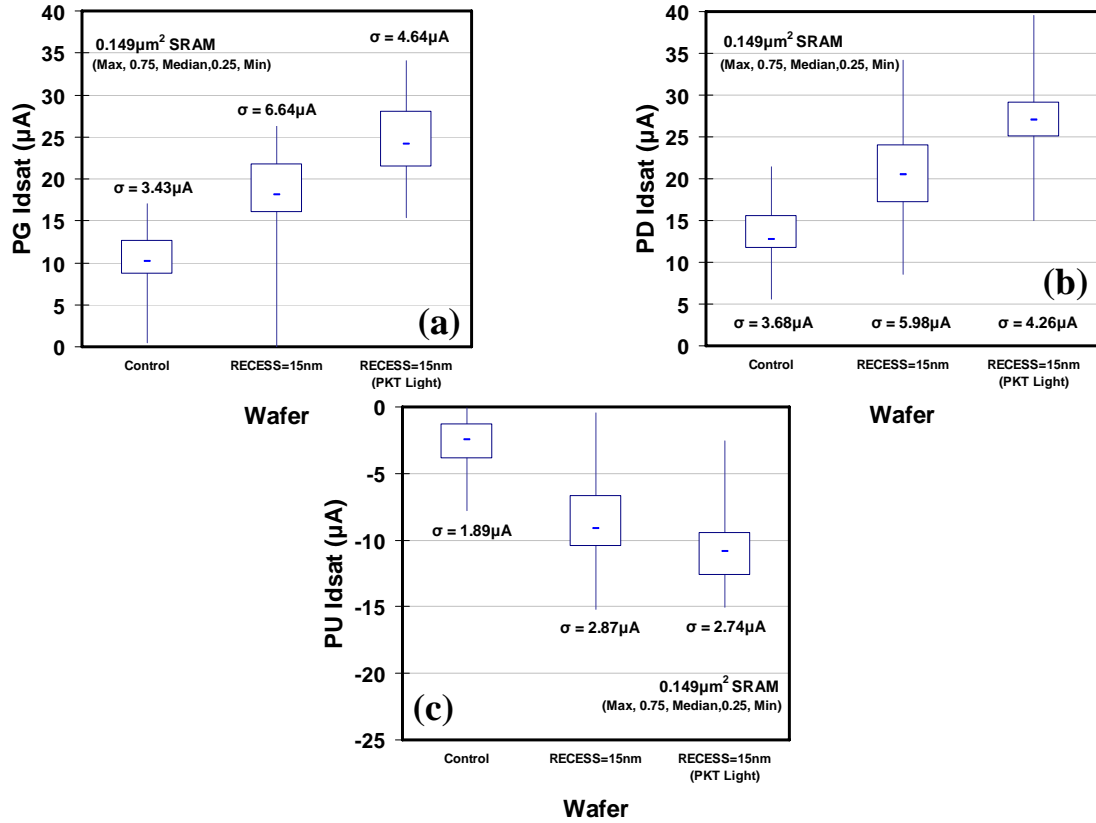


Figure 5.3. Comparison of ON/OFF current statistics for planar (Control) vs. quasi-planar (RECESS=15nm) bulk MOSFETs in SRAM cells. (a) pass-gate NMOS  $I_{ON}$ , (b) pull-down NMOS  $I_{ON}$ , (c) pull-up PMOS  $I_{ON}$ .

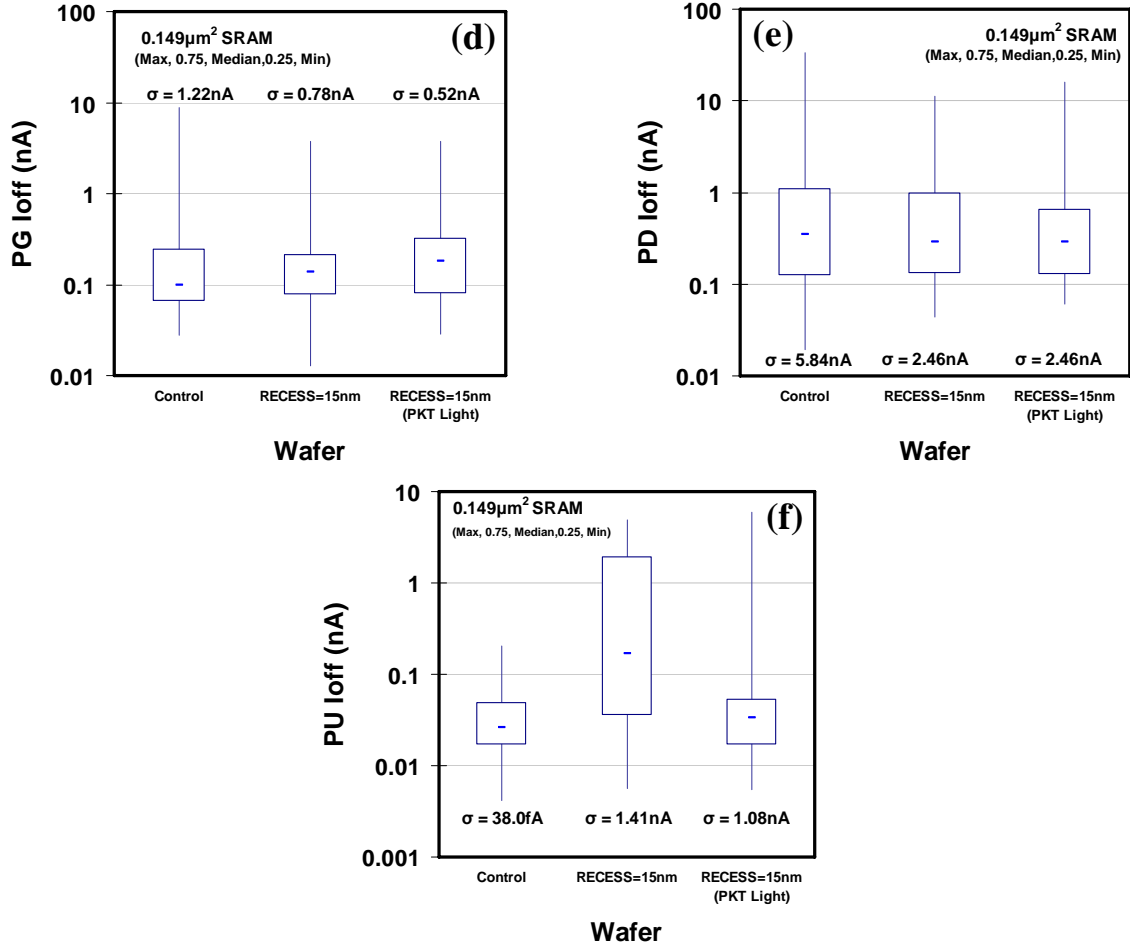


Figure 5.3. Comparison of ON/OFF current statistics for planar (Control) vs. quasi-planar (RECESS=15nm) bulk MOSFETs in SRAM cells. (d) pass-gate NMOS  $I_{\text{OFF}}$ , (e) pull-down NMOS  $I_{\text{OFF}}$ , (f) pull-up PMOS  $I_{\text{OFF}}$ .

### 5.3.1.2 Suppressed $V_{\text{TH}}$ Variation

$V_{\text{TH}}$  statistics are shown in **Fig. 5.4** for the PG/PD/PU devices. Improved gate control results in steeper subthreshold swing and hence lower  $V_{\text{TH}}$  for the quasi-planar MOSFETs. In this early 28nm CMOS process, the standard pocket implant dose is relatively high for the n-channel devices. As a result, variation in  $V_{\text{TH}}$  is slightly larger for the quasi-planar PG and PD devices, due to more significant impact of random dopant fluctuations (RDF) for the gated sidewalls. This undesirable effect is eliminated by using a lighter pocket implant dose, as shown in **Figs. 5.4a and 5.4b**, which further lowers  $V_{\text{TH}}$  without significantly increasing  $I_{\text{OFF}}$  (ref. Figs. 5.3d and 5.3e). The standard pocket implant dose is lower for the p-channel devices, so that the impact of RDF for the gated sidewalls is not an issue. Thus, PMOS  $V_{\text{TH}}$  variation is reduced when the STI oxide is recessed, due to the

superior electrostatic integrity of the quasi-planar structure (**Fig. 5.4c**). If an even lighter pocket implant dose is used, then  $V_{TH}$  variation is slightly larger due to degraded short-channel effect. In short,  $V_{TH}$  variation in quasi-planar devices can be lower than in planar devices if the channel/pocket doping level is optimized.

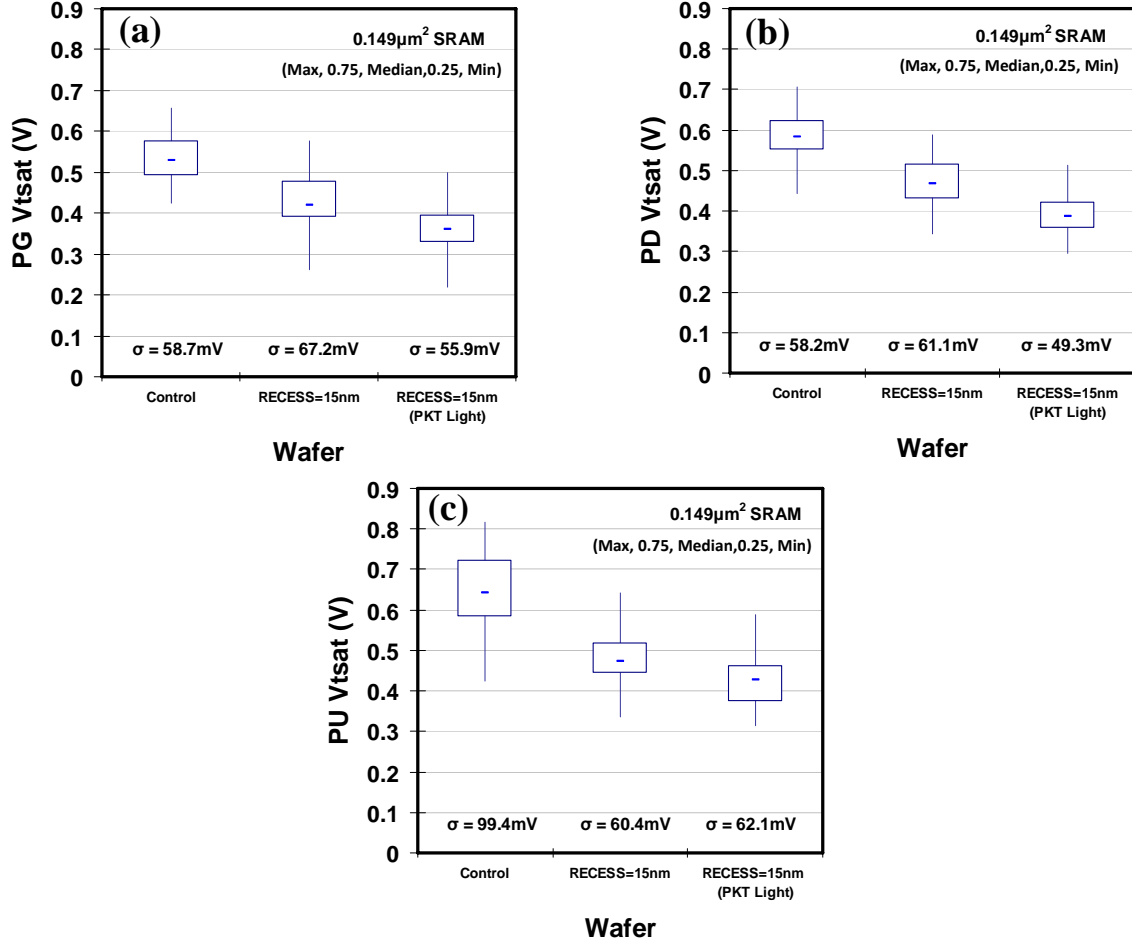


Figure 5.4. Comparison of saturation  $V_{TH}$  statistics for planar (Control) vs. quasi-planar (RECESS=15nm) bulk MOSFETs in SRAM cells: (a) pass-gate NMOS, (b) pull-down NMOS, (c) pull-up PMOS.

Pelgrom plots [10] showing how  $V_{TH}$  variation increases with decreasing channel area, for logic devices, are shown in **Fig. 5.5**. Pelgrom's coefficient ( $A_{VT}$ ) is reduced by 8% and 7% for the NMOS and PMOS quasi-planar devices with lower pocket doping, respectively. This improvement is consistent with the SRAM device results shown in **Fig. 5.4**.



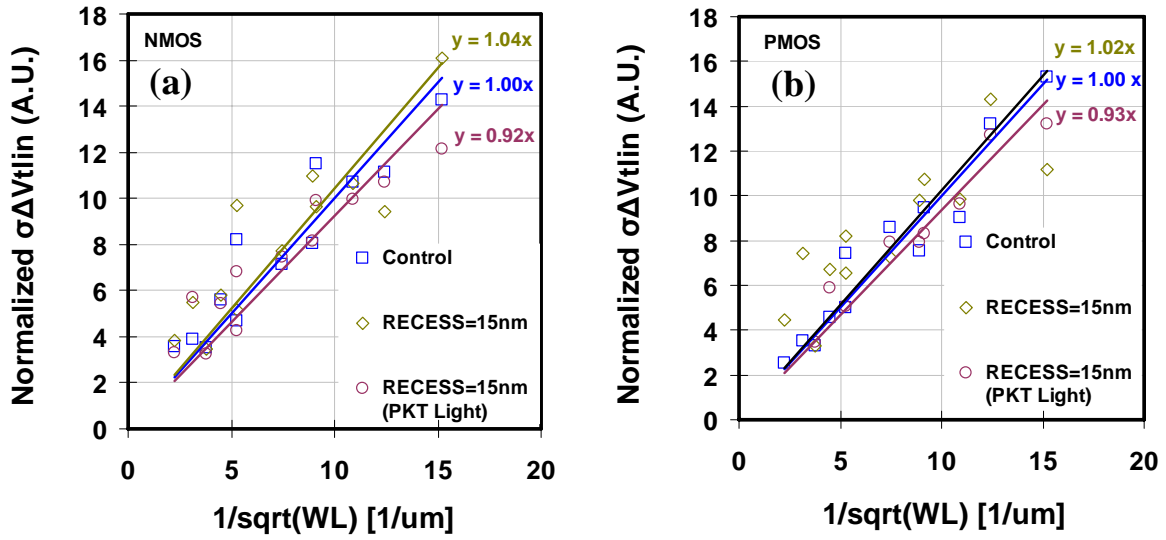


Figure 5.5. Pelgrom plots for (a) NMOS and (b) PMOS logic devices with drawn width ranging from 120nm to 1 $\mu$ m and drawn gate length ranging from 36nm to 0.2 $\mu$ m.

### 5.3.1.3 Improved Short-Channel Effect

**Fig. 5.6** shows the short-channel effect for logic devices with 250nm drawn width. It can be seen that VT roll-off is reduced for the quasi-planar structures, even though the channel is much wider (by  $>16\times$ ) than the STI oxide recess depth. Reasonable short-channel control is maintained by the quasi-planar structure even with lighter pocket doping.

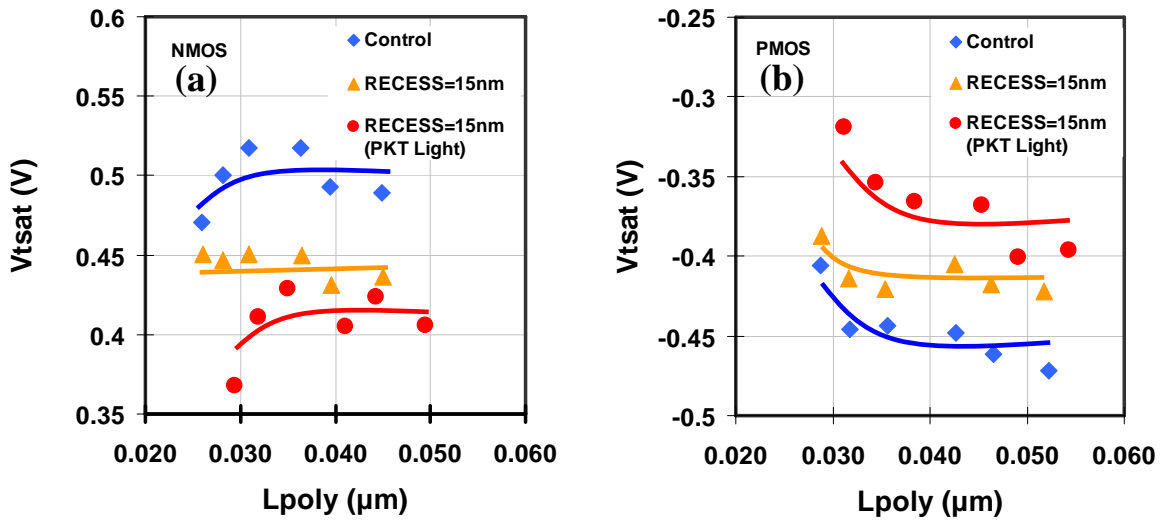


Figure 5.6. Saturation threshold voltage with decreasing gate length, for logic devices with 0.25 $\mu$ m drawn width. (a) NMOS (b) PMOS.

### 5.3.1.4 Increased Narrow Width Effect

The reverse narrow width effect, *i.e.*,  $V_{TH}$  reduction with decreasing channel width ( $W$ ), stems from increased gate control for narrower channel width due to fringing electric fields between the gate electrode and channel sidewalls. This effect is intensified in quasi-planar devices, as shown in **Fig. 5.7**. It should be noted that, overall,  $V_{TH}$  variation is lower for quasi-planar devices -- even with reduced pocket doping -- than for the planar devices, due to improved short channel control.

To maximize the benefits of quasi-planar CMOS technology, wider transistors should be segmented into stripes of uniform width less than or equal to  $\sim 2L_G$  [11]. A double-patterning approach [12] similar to that used for gate patterning in state-of-the-art CMOS processes can be used to form channel segments of highly uniform width without the need for forming high-aspect-ratio isolation trenches.

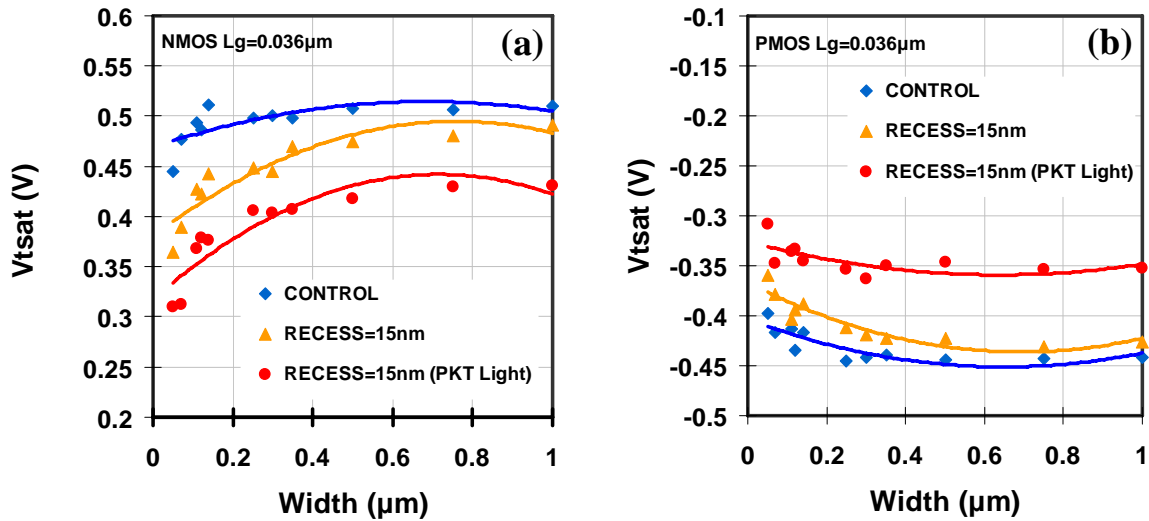


Figure 5.7. Measured reverse narrow width effect for devices with 36nm gate length: (a) NMOS (b) PMOS. Median  $V_{TH}$  is lower when the STI oxide is recessed, due to improved gate control over the channel potential.

### 5.3.1.5 Compact Transistor Model

One of the advantages of quasi-planar CMOS technology over FD-SOI and FinFET/MuGFET/Tri-Gate FET technologies is that it is compatible with standard bulk MOSFET compact models used for circuit design. In this work, the BSIM4.6 compact model was calibrated to the electrical characteristics of quasi-planar bulk MOSFETs, with fitting parameters including electrical and physical gate-oxide thickness, gate length offset,

and the number of fingers in the device. **Fig. 5.8** shows that the compact model can be well-fitted to quasi-planar bulk MOSFET characteristics, including the body effect. This illustrates another advantage of quasi-planar CMOS technology, which is that it allows for adaptive body biasing, *i.e.*, dynamic optimization of the trade-off between performance (delay) and power consumption (energy).

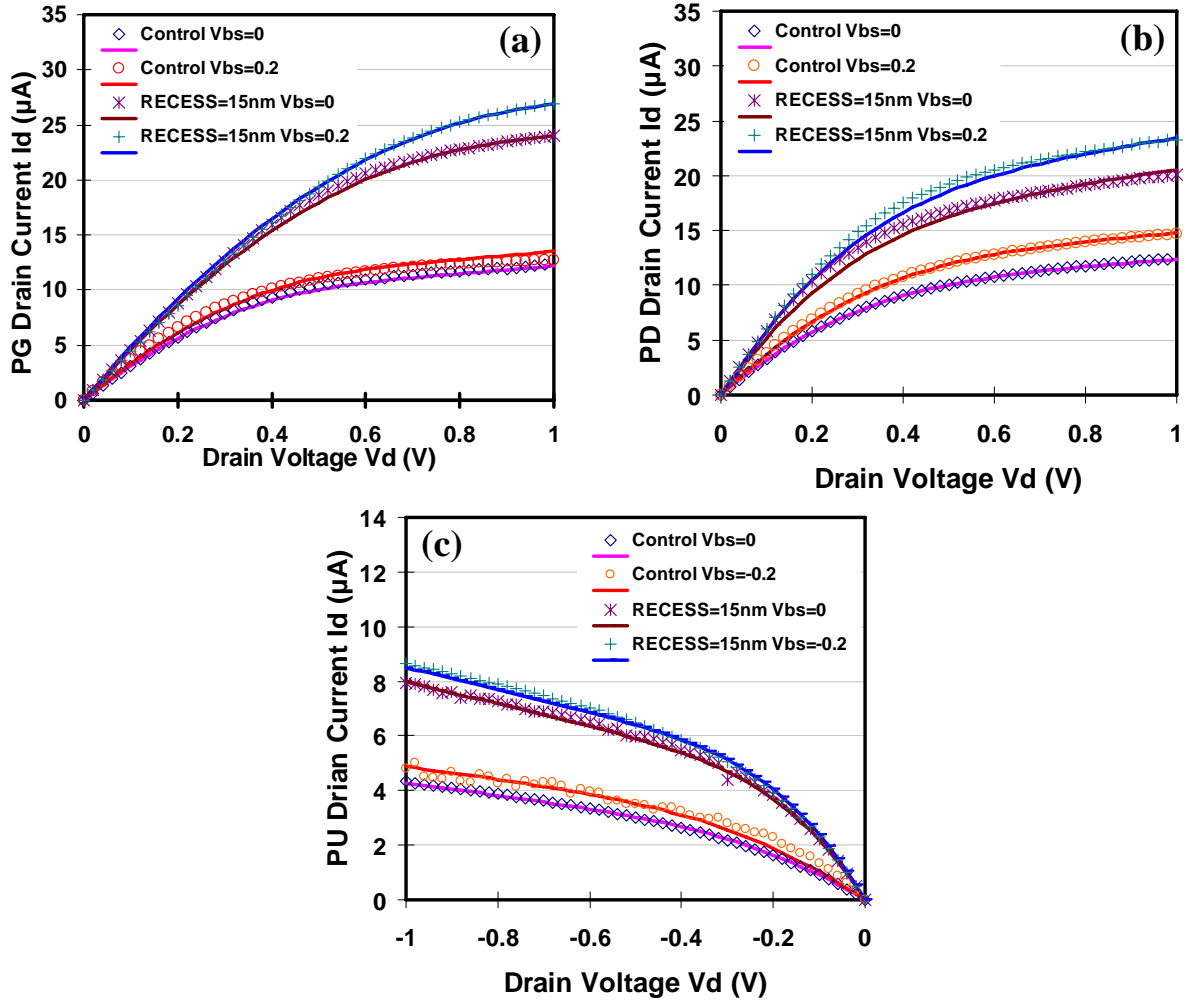


Figure 5.8. Comparison of measured output characteristics for planar (Control) vs. quasi-planar (RECESS=15nm) bulk MOSFETs in SRAM cells, for  $|V_{GS}| = 1.0V$ . The effect of forward body biasing is also shown. (a) pass-gate NMOS, (b) pull-down NMOS, (c) pull-up PMOS. The symbols are measured data; the lines show the fitted compact model.

## 5.3.2 Benefits of Quasi-Planar Bulk CMOS Technology for 6T-SRAM

### 5.3.2.1 Cell Yield Enhancement

In this early 28nm CMOS technology, SRAM yield (gauged by 3-sigma/mean values for DC read and write noise margins, SNM and WRM, respectively) was slightly diminished by recessing the STI oxide, because of the aforementioned increase in NMOS  $V_{TH}$  variation (ref. Figs. 5.4a and 5.4b). If lighter pocket doping is used, however, variability is reduced so that yield is superior for the quasi-planar CMOS technology, as shown in **Fig. 5.9**. The nominal SNM is degraded by recessing the STI oxide because the cell beta ratio is degraded (even though the drive strength of the PU device is improved), which is why the increase in 3sigma/median is larger than for sigma (**Fig. 5.9a**). The fact that nominal WRM is improved by recessing the STI oxide accounts for the observation that 3sigma/median does not increase by very much, even though sigma increases significantly due to increased PG  $V_{TH}$  variation (**Fig. 5.9b**).

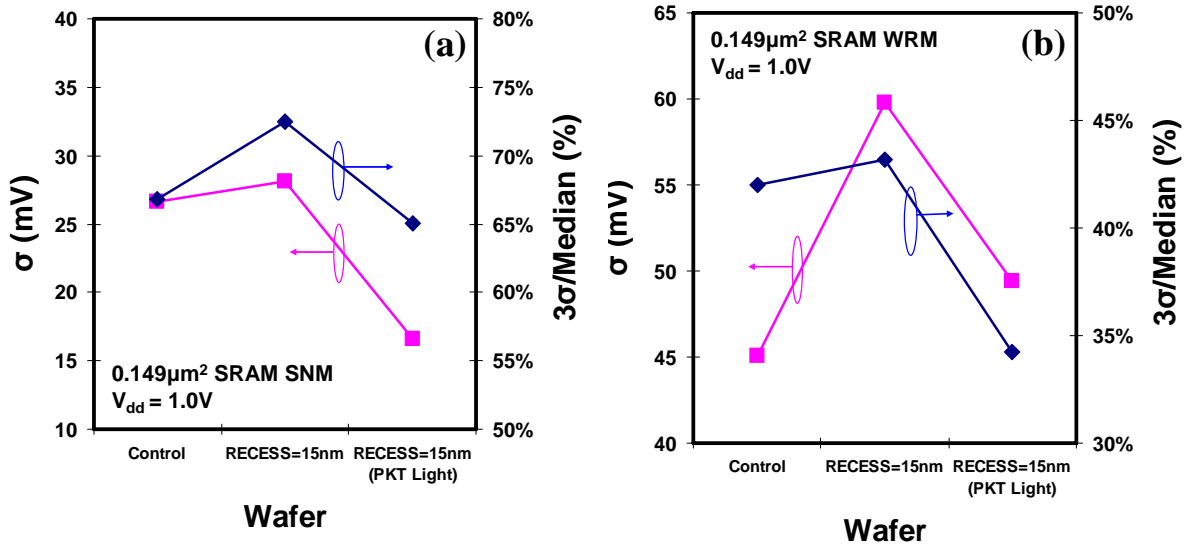


Figure 5.9. Sigma and 3-sigma/median values for (a) read margin (SNM) and (b) write margin (WRM).  $V_{dd} = 1.0\text{V}$ .

### 5.3.2.2 Supply-Voltage Reduction

Supply-voltage ( $V_{dd}$ ) reduction is desirable to reduce power density and to facilitate increased transistor density. Generally, however, relative variability increases as the gate overdrive ( $V_{dd} - V_{TH}$ ) decreases, so that yield is degraded. **Fig. 5.10** shows that the degradation in SNM yield with  $V_{dd}$  reduction (from 1.0V to 0.8V) is dramatically reduced for quasi-planar bulk CMOS technology with reduced pocket doping, while the degradation

in WRM yield with  $V_{dd}$  reduction is not significantly worse for quasi-planar bulk CMOS technology. With separately optimized pocket implant doses for the NMOS and PMOS devices, reduced degradation in both SNM yield and WRM yield with  $V_{dd}$  scaling can be achieved.

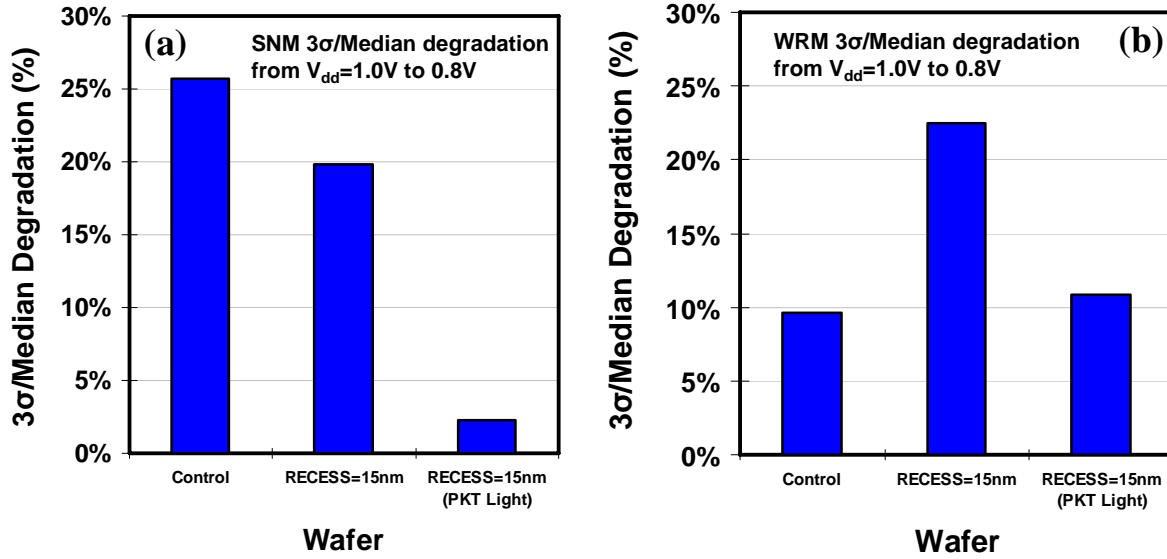


Figure 5.10. Degradation in 3-sigma/median for (a) SNM and (b) WRM as  $V_{dd}$  is reduced from 1.0V to 0.8V.

## 5.4 Summary

With optimized pocket doping, quasi-planar MOSFETs achieved by slightly recessing the STI oxide prior to gate-stack formation in an otherwise conventional CMOS fabrication process can provide for improved performance and reduced variability, and hence can facilitate the scaling of SRAM operating voltage. The benefits of the quasi-planar bulk MOSFET design increase with decreasing channel width, so that quasi-planar CMOS technology is a compelling solution for future generations (22nm and beyond).

As already discussed in the Chapter 2, fully-depleted silicon-on-insulator (FD-SOI) technology with thin buried-oxide (thin-BOX) provides for improved read-stability yield (by 1.2 $\sigma$ ), and write-ability yield (by 2.2 $\sigma$ ) for fixed SRAM cell area, as compared against planar bulk technology. For fixed yield, the FD-SOI SRAM cell provides a cell-area savings of ~ 25%. This benefit of area savings is offset by the incremental cost of an SOI substrate. In addition, established strain engineering techniques such as the use of embedded source/drain stressors cannot be used with FD-SOI technology, due to inherently ultra-shallow source/drain regions. In contrast, the quasi-planar bulk technology described herein offers a more cost-effective alternative, one that preserves the advantages of a conventional planar bulk technology (compatibility of strain engineering techniques to

enhance mobility, dynamic threshold voltage control, an established compact device model, and low substrate cost) while offering the advantages of a multi-gate technology (improved performance and scalability). The benefits of quasi-planar bulk MOSFET technology will only increase with transistor scaling, since decreasing channel width results in improved electrostatic integrity, so that it is a compelling solution for CMOS scaling to the end of the technology roadmap (sub-10nm gate lengths).

## 5.5 References

- [1] A. Asenov, A. R. Brown, J. H. Davies, S. Kaya, and G. Slavcheva, "Simulation of intrinsic parameter fluctuations in decanometer and nanometer-scale MOSFETs," *IEEE Trans. Electron Devices*, vol. 50, no. 9, pp. 1837–1852, Sep. 2003.
- [2] H. Dadgour, K. Endo, V. De, and K. Banerjee, "Modeling and analysis of grain-orientation effects in emerging metal-gate devices and implications for SRAM reliability," *IEDM Tech. Dig.*, 2008, pp. 705–708.
- [3] K. A. Bowman, X. Tang, J. C. Eble, and J. D. Meindl, "Impact of extrinsic and intrinsic parameter fluctuations on CMOS circuit performance," *IEEE J. Solid-State Circuits*, vol. 35, no. 8, pp. 1186–1193, Aug. 2000.
- [4] K. Nii, M. Yabuuchi, Y. Tsukamoto, S. Ohbayashi, Y. Oda, K. Usui, T. Kawamura, N. Tsuboi, T. Iwasaki, K. Hashimoto, H. Makino, and H. Shinohara, "A 45-nm single-port and dual-port SRAM family with robust read/write stabilizing circuitry under DVFS environment," *VLSI Symp. Circuit Dig.*, 2008, pp. 212–213.
- [5] C. Fenouillet-Beranger, S. Denorme, P. Perreau, C. Buj, O. Faynot, F. Andrieu, L. Tosti, S. Barnola, T. Salvétat, X. Garros, M. Casse, F. Allain, N. Loubet, L. Pham-Nguyen, E. Deloffre, M. Gros-Jean, R. Beneyton, C. Laviro, M. Marin, C. Leyris, S. Haendler, F. Leverd, P. Gouraud, P. Scheiblin, L. Clement, R. Pantel, S. Deleonibus, and T. Skotnicki, "FDSOI devices with thin BOX and ground plane integration for 32 nm node and below," *Solid State Electron.*, vol. 53, no. 7, pp. 730–734, Jul. 2009.
- [6] H. Kawasaki, M. Khater, M. Guillorn, N. Fuller, J. Chang, S. Kanakasabapathy, L. Chang, R. Muralidhar, K. Babich, Q. Yang, J. Ott, D. Klaus, E. Kratschmer, E. Sikorski, R. Miller, R. Viswanathan, Y. Zhang, J. Silverman, Q. Ouyang, A. Yagishita, M. Takayanagi, W. Haensch, and K. Ishimaru, "Demonstration of highly scaled FinFET SRAM cells with high-K/metal gate and investigation of characteristic variability for the 32 nm node and beyond," *IEDM Tech. Dig.*, 2008, pp. 237–240.
- [7] C. H. Tsai, T.-J. King Liu, S. H. Tsai, C. F. Chang, Y. M. Tseng, R. Liao, R. M. Huang, P. W. Liu, C. T. Tsai, C. Shin, B. Nikolić, C. W. Liang, "Segmented tri-gate CMOS technology for device variability improvement," *Proc. IEEE VLSI-TSA*, Apr. 2010, pp. 114–115.
- [8] C. Shin, C. H. Tsai, M. H. Wu, C. F. Chang, Y. R. Liu, C. Y. Kao, G. S. Lin, K. L. Chiu, C.-S. Fu, C.-T. Tsai, C. W. Liang, B. Nikolić, T.-J. King, Liu, "Tri-gate bulk CMOS technology for improved SRAM scalability," *Proc. IEEE European Solid-State Device Research Conf.* Sep. 2010, pp. 142–145.

- [9] L. Chang, M. Jeong, and M. Yang, "CMOS circuit performance enhancement by surface orientation optimization," *IEEE Trans. Electron Devices*, vol. 51, no. 10, pp. 1621–1627, Oct. 2004.
- [10] M. J. M. Pelgrom, A. Duinmaijer, and A. Welbers, "Matching properties of MOS transistors," *IEEE J. Solid-State Circuits*, vol. 24, no. 5, pp. 1433–1440, Oct. 1989.
- [11] X. Sun, Q. Liu, V. Moroz, H. Takeuchi, G. Gebara, J. Wetzel, S. Ikeda, C. Shin, and T.-J. King Liu, "Tri-gate bulk MOSFET design for CMOS scaling to the end of the roadmap," *IEEE Electron Device Lett.*, vol. 29, no. 5, pp. 491–493, May 2008.
- [12] U.S. patent 7,190,050.

## Chapter 6

# Performance and Yield Benefits of Quasi-Planar Bulk CMOS Technology for 6-T SRAM at the 22 nm Node

### 6.1 Introduction

Efforts to reduce six-transistor (6-T) SRAM cell area [1-5] by a factor of two with each new technology generation are the de facto driving force for cutting-edge CMOS technology development. Continued SRAM cell area scaling is essential to sustaining Moore's Law. However, it is challenged by both increased process-induced variability with transistor scaling and the need to integrate more cells on a die at each successive technology node. Specifically, a growing issue is transistor threshold voltage ( $V_{TH}$ ) mismatch due to systematic and random variations [6, 7], which sets a lower limit for the operating voltage of the SRAM array [8]. Variations in  $V_{TH}$  caused by random dopant fluctuations (RDF) and gate line-edge-roughness (LER) will become dominant as the gate length ( $L_G$ ) is scaled down below 30 nm [9].

Various circuit- and transistor-design approaches have been proposed to address the issue of increasing  $V_{TH}$  variation. These include the use of read-assist and write-assist techniques to enhance SRAM read and write margins, for example read/write-assist column circuitry, word-line bias, pulsed bit lines, and lower column supply voltages during write [10, 11] – which results in lower array efficiency (*i.e.*, larger array layout area). Transistor-design approaches include the use of a super-steep retrograde or delta-shaped body doping profile [12], or the adoption of a transistor structure that provides for improved electrostatic integrity, such as fully depleted ultra-thin-body or multi-gate structures [13-15], to reduce



$V_{TH}$  sensitivity to variations. To avoid the need for costly silicon-on-insulator substrates or complex fabrication processes [16, 17], the quasi-planar bulk MOSFET design (**Fig. 6.1**) was recently proposed [18]. A simple approach for manufacturing this structure using a conventional CMOS process flow was recently demonstrated to provide for improved yield in an early 28 nm-generation SRAM technology [19, 20]: a timed dilute-HF etch is used to slightly recess the shallow trench isolation (STI) oxide just prior to gate-stack formation, resulting in gate electrodes that each wrap around the top portion of their respective MOSFET channel region. In this chapter, the potential benefits of quasi-planar bulk CMOS technology *vs.* planar bulk CMOS technology with regard to six-transistor (6-T) SRAM cell performance and yield are assessed, for the 22 nm technology node.

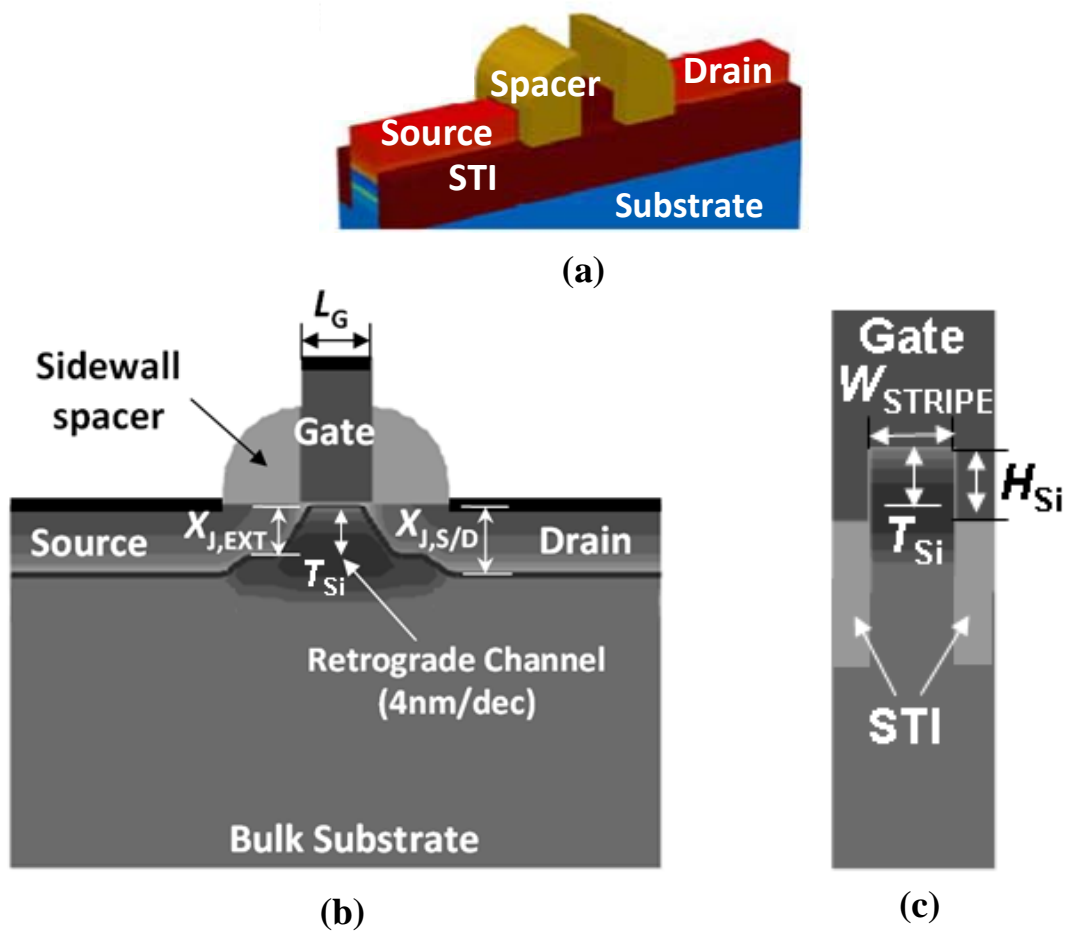


Figure 6.1. (a) Bird-eye view of a quasi-planar bulk MOSFET (gate electrode not shown to allow channel region to be seen), and its cross-sectional views (b) along and (c) across the channel.

## 6.2 Quasi-Planar Bulk Technology

### 6.2.1 Optimized MOSFET Performance

Quasi-Planar bulk CMOSFET designs were optimized for gate length  $L_G = 25$  nm and transistor width  $W_{\text{STRIP}} = 30$  nm, using three-dimensional (3-D) device simulations, to achieve the highest on-state drive current ( $I_{\text{ON}}$ ) for an off-state leakage current ( $I_{\text{OFF}}$ ) no greater than 3 nA/um, effective oxide thickness (EOT)  $T_{\text{ox}} = 9$  Å and  $V_{\text{DD}} = 1$  V: electrical channel length (defined as the distance between the points where the source/drain extension (SDE) doping profiles fall to  $2 \times 10^{19} \text{ cm}^{-3}$ )  $L_{\text{eff}} = 27$  nm for NMOS, 28 nm for PMOS; source/drain extension (SDE) junction depth  $X_{\text{J,EXT}} = 10$  nm; deep source/drain junction depth  $X_{\text{J,S/D}} = 28$  nm; shallow-trench-isolation (STI) oxide recess depth ( $H_{\text{si}}$ ) = 10 nm; near-band-edge gate work functions  $\Phi_M = 4.2$  eV for NMOS, 5.1 eV for PMOS. The retrograde channel doping profile is assumed to have a gradient of 4 nm/dec and peak doping concentration ( $N_{\text{peak}} = 10^{19} \text{ cm}^{-3}$ ) at a depth  $T_{\text{si}}$  below the top channel surface; the SDE doping profile is assumed to have a steep lateral gradient of 2 nm/dec. Steep retrograde doping profiles have been achieved in practice via selective epitaxial growth of the lightly doped (or undoped) channel region [21-26] or by utilizing diffusion-barrier layers [27]. The same design parameter values are assumed for the planar bulk MOSFET design, except that  $\Phi_M = 4.08$  eV for NMOS and 5.2 eV for PMOS to yield similar nominal values of saturation threshold voltage as their quasi-planar counterparts.

**Fig. 6.2** shows the transfer characteristics ( $I_{\text{DS}}$  vs.  $V_{\text{GS}}$ ) for the optimized quasi-planar bulk and planar bulk MOSFET structures, with  $T_{\text{si}} = 10$  nm. The quasi-planar bulk devices exhibit steeper sub-threshold slopes due to better capacitive coupling between the gate and the channel region. A summary comparison of device performance parameters is given in **Table 6.1**. These simulation results are consistent with recently-reported experimental results [20] for devices which have worse electrostatic integrity (*e.g.*,  $\text{DIBL} > 100$  mV/dec), that have shown that quasi-planar bulk MOSFETs achieve higher  $I_{\text{ON}}$  at comparable  $I_{\text{OFF}}$  -- and have lower  $V_{\text{TH}}$  variation -- as compared to conventional planar bulk MOSFETs, so that they provide for improved SRAM yield. In this chapter, the planar bulk MOSFET design is optimized with very shallow SDE junction depths [28] to achieve very good electrostatic integrity --  $\text{DIBL} < 50$  mV/V -- to present the best-case scenario against which to compare the quasi-planar bulk MOSFET design.

An analytical I-V model for the short-channel MOSFET [15] was fit to the simulated current-vs.-voltage characteristics. This model can be used to estimate SRAM performance metrics such as read static noise margin (SNM) [29, 31], static write margin expressed through the write-ability current ( $I_w$ ) [30, 31], and read current. It is used in this work to estimate SRAM cell yield following the methodology described in [32].

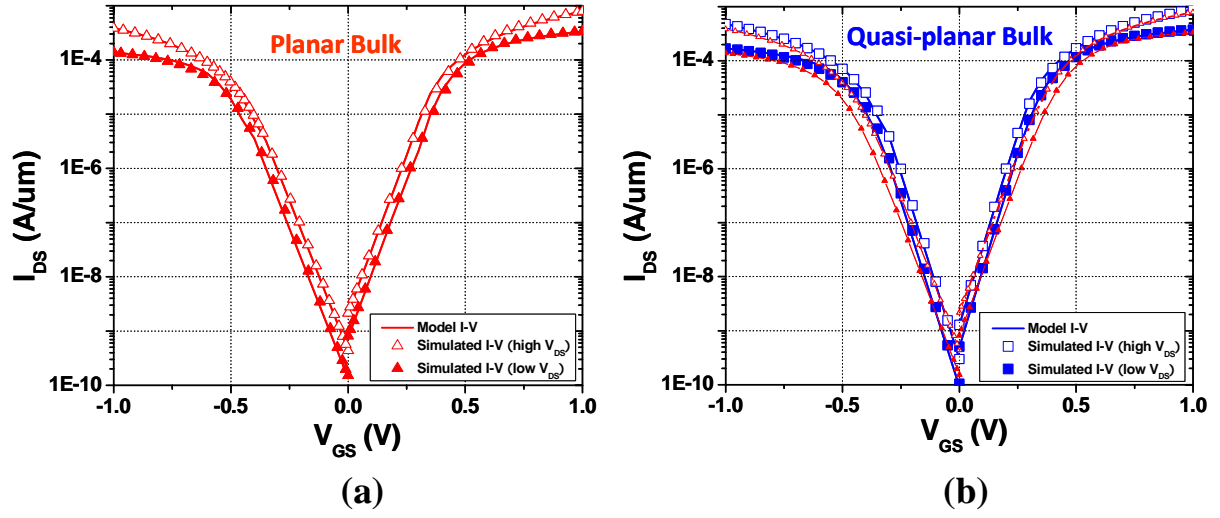


Figure 6.2. Simulated transfer characteristics for (a) planar bulk and (b) quasi-planar bulk MOSFETs. To facilitate a direct comparison, the curves from (a) are overlaid in (b). The current is normalized to  $W_{\text{STRIPE}} + 2 \times H_{\text{Si}}$ .

$V_{\text{DD}} = 1.0\text{V}$	Quasi-planar bulk		Planar bulk	
	N-type	P-type	N-type	P-type
$I_{\text{ON}} [\mu\text{A}/\mu\text{m}]$	884	476	786	386
$I_{\text{OFF}} [\text{nA}/\mu\text{m}]$	1.3	0.30	2.2	0.44
SS [mV/dec]	69	71	85	88
$ V_{\text{TH,LIN}}  [\text{V}]$	0.16	0.21	0.17	0.25
$ V_{\text{TH,SAT}}  [\text{V}]$	0.13	0.18	0.13	0.21
DIBL [mV/V]	33	37	44	46
$L_{\text{eff}} [\text{nm}]$	27	28	27	28

Table 6.1. Summary of transistor performance parameters. The ON/OFF currents are normalized to  $W_{\text{STRIPE}} + 2 \times H_{\text{Si}}$ .

## 6.2.2 Impact of Random and Systematic Variations

The impact of random variations on transistor performance was studied via 3-D device simulations using realistic gate-electrode profiles and atomistic doping. Gate LER was simulated by sampling line-edge profiles from a scanning electron microscopy (SEM) image of photoresist lines printed for the 22 nm node. This represents the worst-case scenario, since the LER of a patterned gate electrode generally is less severe than that of the resist line used to define it. Also, the SDE junction lateral profiles are assumed to have the same LER as the gate electrode, so that  $L_{\text{eff}}$  will have the same roughness profile as  $L_G$ . In this manner, gate-LER-induced variations in  $V_{\text{TH}}$  (*i.e.*,  $\sigma(V_{\text{TH}})|_{\text{gate-LER}}$ ) were found to be = 31 mV for the planar bulk MOSFET and 16 mV for the quasi-planar bulk MOSFET with  $W_{\text{STRIPE}}/L_G=30\text{nm}/25\text{nm}$ .

Since the quasi-planar bulk MOSFET structure is an evolutionary form of the conventional planar bulk MOSFET structure [18] -- in contrast to the vertical FinFET/MuGFET structure -- it can be reasonably expected that gate-LER-induced variation for a quasi-planar bulk MOSFET would be very similar to that for a conventional planar bulk MOSFET. To verify this, LER-induced  $V_{\text{TH}}$  variation for the various device architectures was compared: it was found that for the high-aspect-ratio FinFET/MuGFET, LER-induced  $V_{\text{TH}}$  variation increases with decreasing correlation length due to increased misalignment between the front and back gates [33]; in contrast, for the low-aspect-ratio quasi-planar MOSFET and conventional planar MOSFET, LER-induced  $V_{\text{TH}}$  variation decreases with decreasing correlation length due to an averaging effect.

The methodology proposed by Sano [34], wherein only the long-range Coulomb potential for an ionized dopant atom is considered to avoid unrealistic singularities in potential profile, was used to simulate the effect of RDF for each of the gate-electrode profile cases. Details are described in [35], and only the results are summarized here:  $\sigma(V_{\text{TH}})|_{\text{RDF}} = 54$  mV for the planar bulk MOSFET and 30 mV for the quasi-planar bulk MOSFET with  $W_{\text{STRIPE}}/L_G=30\text{nm}/25\text{nm}$ .

**Fig. 6.3a** shows the distributions of saturation  $V_{\text{TH}}$  (*i.e.*, the value of  $V_{\text{GS}}$  corresponding to 100 nA/um for  $V_{\text{DS}} = 1$  V) obtained from the simulated  $I_{\text{DS}}-V_{\text{GS}}$  curves (200 cases) for each device structure. The standard deviation of  $V_{\text{TH}}$  variation ( $\sigma(V_{\text{TH}})$ ) for the quasi-planar device is smaller than that for the planar device. This is due to improved suppression of short-channel effects (SCE) in the quasi-planar device, and the fact that it has  $\sim 1.6\times$  larger effective channel width  $W_{\text{eff}}$  (based on linear  $I_{\text{DS}}$  values) but only slightly greater depletion charge [35].

**Fig. 6.3b** compares the  $V_{\text{TH}}$  mismatch, gauged by the Pelgrom coefficient ( $A_{\text{VT}}$ ) [36], for the simulated devices in this work against that of experimental devices reported in the

literature. It can be seen that  $A_{VT}$  for the planar bulk device design in this work follows the trend for planar bulk technologies.  $A_{VT}$  of the quasi-planar bulk device design is improved, to be slightly worse than  $A_{VT}$  for reported ultra-thin-body MOSFET technologies.

The impacts of systematic variations ( $\pm 10\%$ ) in  $L_G$ , EOT, and  $W_{\text{STRIPE}}$ , are shown in **Figs. 6.3c, 6.3d, and 6.3e**, respectively. The short channel effect is better suppressed in the quasi-planar bulk MOSFET, due to improved gate control. This benefit is equivalent to  $>6$  Å reduction in  $T_{\text{ox}}$ . Also, variations in  $T_{\text{ox}}$  have less impact for the quasi-planar bulk MOSFET. The quasi-planar bulk MOSFET shows a stronger reverse-narrow-width effect, but it is still less than 10 mV for 10% variation in  $W_{\text{STRIPE}}$ .

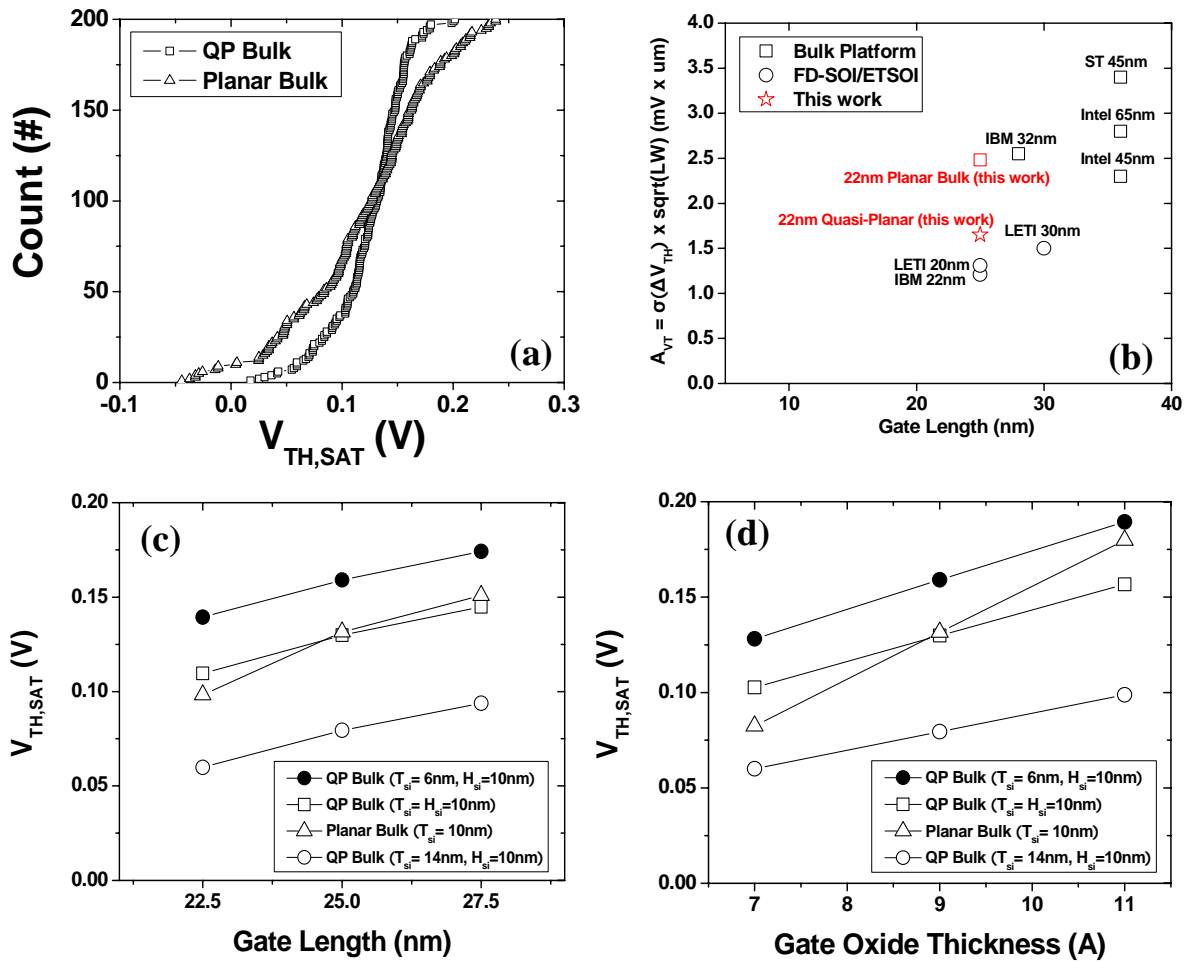


Figure 6.3. Simulated saturation threshold voltage ( $V_{\text{TH,SAT}}$ ) for planar bulk vs. quasi-planar bulk MOSFETs: (a) Distribution of  $V_{\text{TH,SAT}}$  caused by gate-LER and RDF (for  $W_{\text{STRIPE}}/L_G = 30\text{nm}/25\text{nm}$ ), from which  $\sigma(V_{\text{TH,SAT}}|_{\text{Planar Bulk}}) = 61.6$  mV and  $\sigma(V_{\text{TH,SAT}}|_{\text{QP Bulk}}) = 33.1$  mV, (b) Comparison of Pelgrom coefficients for simulated vs. experimental reported devices. (c)  $V_{\text{TH,SAT}}$  vs.  $L_G$ , (d)  $V_{\text{TH,SAT}}$  vs.  $T_{\text{ox}}$ ,

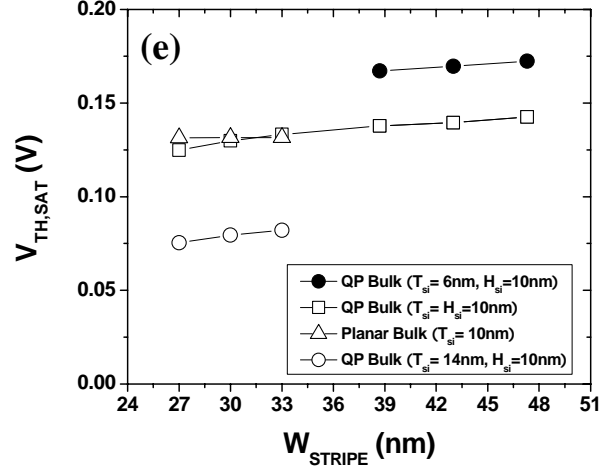


Figure 6.3. Simulated saturation threshold voltage ( $V_{\text{TH,SAT}}$ ) for planar bulk vs. quasi-planar bulk MOSFETs: (e)  $V_{\text{TH,SAT}}$  vs.  $W_{\text{STRIPE}}$ . Note that the quasi-planar bulk MOSFET shows less sensitivity to variations in gate length ( $L_G$ ) and gate-oxide thickness ( $T_{\text{ox}}$ ), and that the depth of the retrograde channel doping profile ( $T_{\text{si}}$ ) can be used to tune the threshold voltage without impacting short-channel control. The quasi-planar bulk MOSFET shows more sensitivity to variations in transistor width, if  $W_{\text{STRIPE}}$  is small (30 nm).

### 6.3 Notchless 6-T SRAM Cell Designs

Layout parameters for 22 nm 6-T SRAM cells (**Fig. 6.4**) were selected based on recent publications [1-5] and are summarized in **Table 6.2**. Nominal SNM and  $I_W$  values were obtained via 3-D simulations of full cell structures using advanced physical models including the density-gradient/drift-diffusion transport model and the phenomenological van Dort quantum correction model to account for energy quantization in the channel regions.

In a conventional SRAM cell layout (**Fig. 6.4a**), the width of the NMOS pull-down (PD) device is larger than the width of the NMOS pass-gate (PG) device, to achieve a cell beta ratio greater than 1 for sufficient nominal SNM. As a result, the NMOS active area pattern is notched. Due to limitations of optical lithography the corners of the active area will be rounded in practice, so that (vertical) misalignment between the gate layer and the active layer results in asymmetric variations in NMOS device width (*i.e.*, mismatch) between the left and right sides of the cell, which can significantly degrade SNM [39].

An advantage of the quasi-planar bulk MOSFET design is that it allows for  $V_{\text{TH}}$  to be adjusted by tuning the depth ( $T_{\text{si}}$ ) -- rather than the dose ( $N_{\text{peak}}$ ) -- of the retrograde channel doping profile, without increasing either short-channel effects or  $V_{\text{TH}}$  variation [35]. (Note that fringing electric fields through the isolation oxide allow good gate control to be

maintained even if  $T_{si}$  is slightly larger than  $H_{si}$ .) This remarkable feature can be exploited to tune the SRAM cell beta ratio by adjusting transistor  $V_{TH}$  values rather than transistor widths, so that a notchless active area pattern (**Fig. 6.4b**) can be used. A notchless cell design can provide for area savings as well as reduced variation in NMOS device width resulting from lithographic misalignment, due to improved printability of the active area pattern.

To achieve sufficient SNM with a notchless quasi-planar SRAM cell design, the NMOS pull-down and PMOS pull-up (PU) devices should have lower  $V_{TH}$  values than the NMOS pass-gate device. This is achieved with a deeper retrograde channel doping profile (**ref. Figs. 6.3c-6.3e**) which could be achieved in practice by using a higher ion-implantation energy. Note that  $H_{si}$  is constrained to be the same for all of the devices in a quasi-planar SRAM cell for ease of manufacture, *i.e.*, the isolation oxide is uniformly recessed (*e.g.*, by using a timed etch in dilute hydrofluoric acid solution, or by elevating the channel with a selective epitaxial growth process) prior to gate-stack formation<sup>1</sup>. Further note that the transistor widths ( $W_{PU}$ ,  $W_{PD}$ , and  $W_{PG}$ ) are constrained to be equal in a notchless cell design, so as to be compatible with a regularly corrugated starting substrate [40] for improved active-area width control.

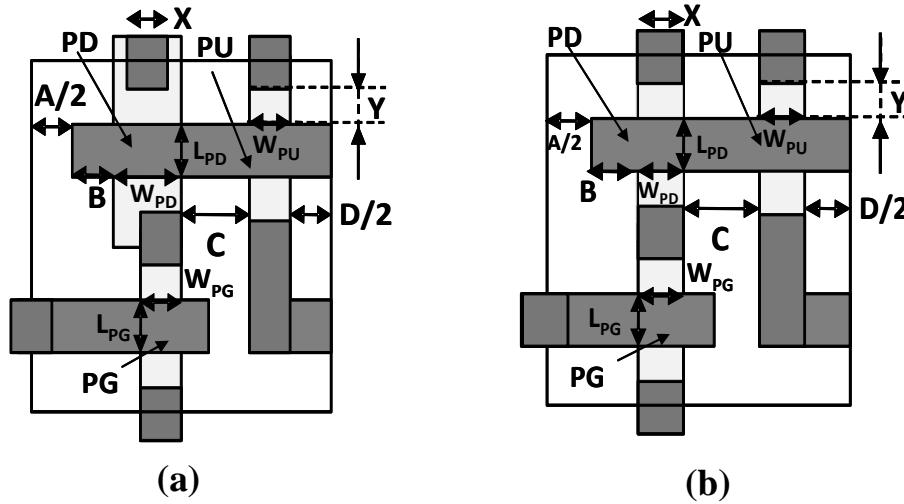


Figure 6.4. Half-bit cell layouts for (a) notched and (b) notchless SRAM cell designs.

Design rules		Symbol	Size [nm]
Cell Height	PG CH length	$L_{PG}$	25
	PD CH length	$L_{PD}$	25
	CONT size	X	30
	Gate-to-CONT	Y	20
	Total	190	
Cell Width	POLY-to-POLY	A	30
	POLY-to-DIF ext	B	20
	PD Width	$W_{PD}$	55 / 30 / 43
	PG width	$W_{PG}$	30 / 30 / 43
	PU width	$W_{PU}$	30 / 30 / 43
	N/P isolation	C	50
	DIF-DIF (min)	D	50
	$H_{si}$ for quasi-planar	$H_{si}$	10
	Total	390 / 340 / 392	
A SRAM cell area		0.0741 / 0.0646 / 0.0745 $\mu m^2$	

Table 6.2. 22nm-node 6-T SRAM cell layout parameters for planar bulk and quasi-planar bulk CMOS technologies.

As can be seen from **Fig. 6.5**, the small notchless quasi-planar SRAM cell achieves comparable SNM and superior write-ability as compared against a conventional notched planar SRAM cell. Significantly larger read current is offered by the quasi-planar SRAM cell designs across a wide range of  $V_{DD}$  (**Fig. 6.6a**). Although gate capacitance is also higher for the quasi-planar SRAM cell designs (**Fig. 6.6b**), simulations of the storage-node transient voltage during a write operation (**Fig. 6.6c**) show that the write time is still shorter for the quasi-planar SRAM cell designs.

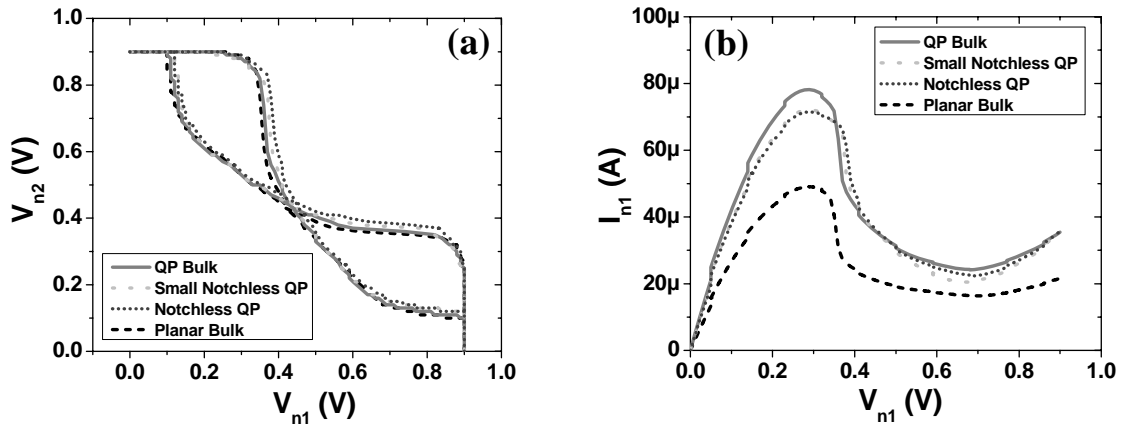


Figure 6.5. 3-D 6-T SRAM cell simulation results for the planar bulk, quasi-planar bulk, and notchless quasi-planar bulk SRAM cells: (a) Butterfly curves, (b) write-N-curves.



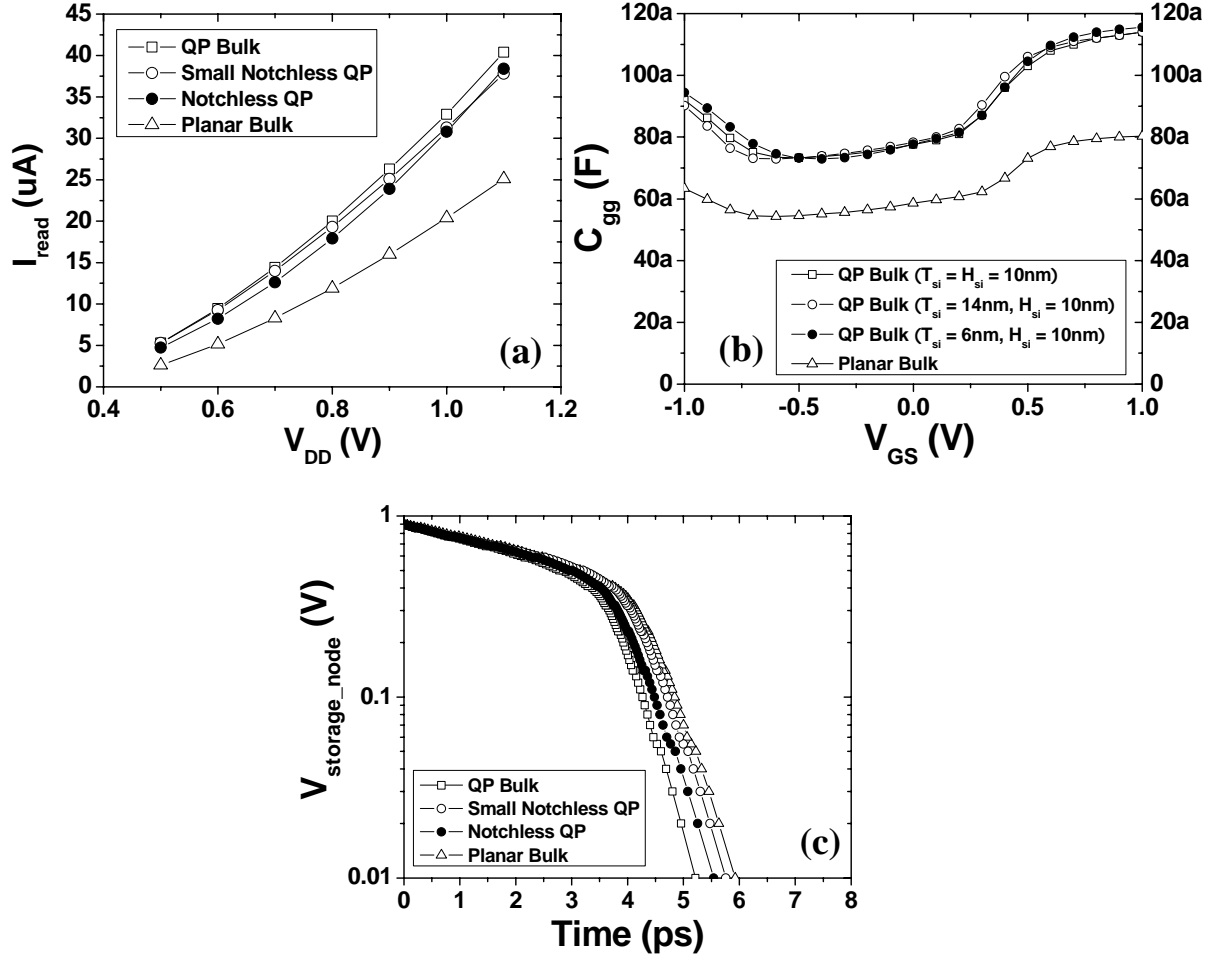


Figure 6.6. (a) SRAM cell read current, (b) PD device gate capacitance, (c) Pseudo-transient simulation of the storage-node voltage during a write operation.

**Table 6.3** summarizes the projected cell performance metrics and cell area values for the planar and quasi-planar SRAM cells. Since  $V_{\text{TH}}$  is lower for the PD and PU devices in the small notchless quasi-planar cell, it has higher standby power consumption ( $P_{\text{standby}}$ ) than the planar (notched) cell.  $P_{\text{standby}}$  can be lowered by increasing  $V_{\text{TH}}$  for all of the transistors in the notchless quasi-planar cell, but then the transistors must be widened to maintain a comparable level of performance and yield, *i.e.*, there would be no area savings in comparison with the notched cell design. The devices in an optimized notchless quasi-planar cell design have shallower retrograde channel doping depths of 10/6/10 nm for PD/PG/PU and widths of 43 nm.

Technology	SNM [mV]	$I_w$ [ $\mu$ A]	Cell area [ $\mu\text{m}^2$ ]	$P_{\text{standby}}$ per bit [nW]
Planar Bulk	180.5	16.4	0.0741	0.218
Quasi-planar Bulk	183.5	24.1	0.0741	0.186
Small Notchless Quasi-planar Bulk ( $W_{\text{STRIPE}} = 30\text{nm}$ , $T_{\text{si}}$ for PD/PG/PU = 14/10/14nm, $H_{\text{si}} = 10\text{nm}$ )	175.6	20.5	0.0646	0.351
Notchless Quasi-planar Bulk ( $W_{\text{STRIPE}} = 43\text{nm}$ , $T_{\text{si}}$ for PD/PG/PU = 10/6/10nm, $H_{\text{si}} = 10\text{nm}$ )	182.7	22.3	0.0745	0.107

Table 6.3. Comparison of projected performance metrics and cell areas for planar bulk and quasi-planar bulk SRAM cells at  $V_{\text{DD}} = 0.9\text{V}$ .

## 6.4 SRAM Yield Estimation

In the previous section, the quasi-planar bulk SRAM cell designs were shown to have improved static performance (*i.e.*, better read stability and write-ability current) and better transient performance (*i.e.*, shorter write time). In this section, the corresponding improvement in cell yield is evaluated using the concept of cell sigma, defined as the minimum amount of variation for read/write failure [32]. If a SRAM cell read/write metric has a Gaussian distribution, its cell sigma is simply its mean value divided by its standard deviation. Random variations due to gate-LER, RDF, and WFV, as well as global variations due to process-induced variations (Gaussian with 3 sigma corresponding to  $\pm 10\%$ ) in gate length, stripe width, gate oxide thickness, and channel stripe height ( $H_{\text{si}}$ ) are considered together in estimating the cell sigma. Although  $\sigma(V_{\text{TH,LIN}})$  is generally smaller than  $\sigma(V_{\text{TH,SAT}})$ , the worst-case scenario  $\sigma(V_{\text{TH,LIN}}) = \sigma(V_{\text{TH,SAT}})$  is assumed herein. Six-sigma ( $6\sigma$ ) yield is required for large SRAM arrays to be functional, *i.e.*, no more than one bit cell can fail out of 505 million bit cells to achieve sufficiently high chip yields.

### 6.4.1 Iso-Area and Iso-Yield Comparisons between Planar and Quasi-Planar Bulk Cell Designs

As shown in **Fig. 6.7**, the SNM cell sigma for the quasi-planar cell is  $\sim 6.3$  at  $V_{\text{DD}} = 0.9\text{V}$ , which is a 1.3-sigma improvement over the planar cell. This yield enhancement can be attributed primarily to lower  $V_{\text{TH}}$  variation for the quasi-planar MOSFET structure. The minimum  $V_{\text{DD}}$  that meets the six-sigma yield requirement for both SNM and  $I_w$  is  $\sim 0.65\text{V}$  for the quasi-planar cell. In stark contrast, the six-sigma yield requirement cannot be met by the planar cell for any value of  $V_{\text{DD}}$ ; it achieves only  $\sim 5$  SNM cell sigma at  $V_{\text{DD}} = 0.9\text{V}$ .

In order for the planar cell to have read and write yields comparable to those of the quasi-planar cell, the widths of the PD, PG and PU transistors must be increased to 110 nm,

65 nm and 65 nm, respectively. The planar cell area must therefore be enlarged to  $\sim 0.1 \mu\text{m}^2$  by  $\sim 46\%$ . In other words, the area savings offered by the quasi-planar cell design is  $\sim 32\%$ .

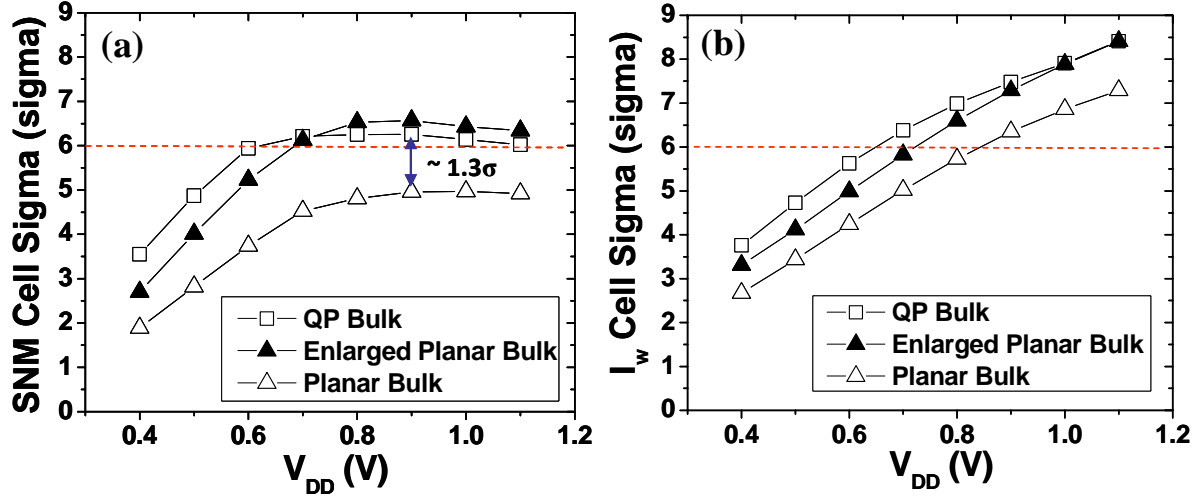


Figure 6.7. SRAM cell sigma comparisons for (a) SNM and (b)  $I_w$ .

#### 6.4.2 Notchless Quasi-Planar Bulk SRAM Cell Yield

As can be seen from **Fig. 6.8**, the notchless quasi-planar cell can meet the 6-sigma yield requirements for  $V_{DD}$  down to  $\sim 0.8V$ , with comparable cell area and faster write time as compared to the conventional planar cell (ref. **Fig. 6.6c**). The small notchless quasi-planar cell (with  $\sim 13\%$  smaller area) is projected to meet the 6-sigma cell yield requirement for  $V_{DD}$  down to  $\sim 0.9V$ .

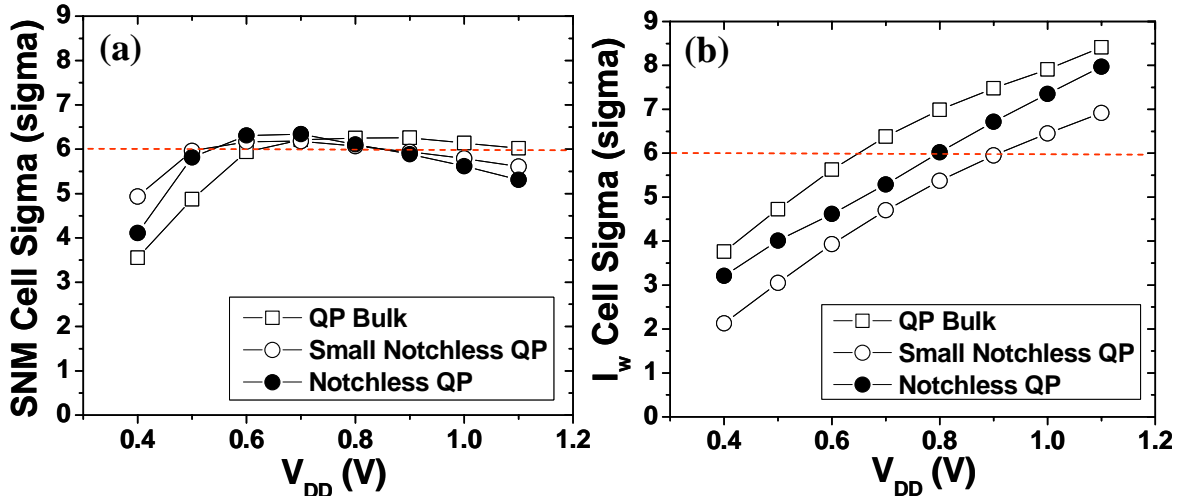


Figure 6.8. SRAM cell sigma comparisons for (a) SNM and (b)  $I_w$ .

## 6.5 Summary

As compared against a planar bulk MOSFET, the quasi-planar bulk MOSFET provides for larger drive current and reduced  $V_{TH}$  variation, due to improved gate control. As a result, quasi-planar bulk SRAM cells are projected to have enhanced write-ability current and faster write time for comparable read stability, as well as  $>1$  sigma improvement in cell yield. A notchless quasi-planar bulk SRAM cell design is proposed for improved lithographic printability and either smaller area or lower standby power, and is projected to achieve 6-sigma cell yields at operating voltages down to  $\sim 0.8V$ .

Although the height ( $H_{si}$ ) of the quasi-planar bulk MOSFET can be made taller to increase its layout area efficiency, this would require a concomitant reduction in silicon width for adequate suppression of short-channel effects. In general, low-aspect-ratio (short and wide) features are preferred for ease of manufacture and design flexibility (*i.e.*, to allow for finer increments in designed  $W_{eff}$ ). On the other hand, if  $H_{si}$  were very short, the benefit of the quasi-planar bulk structure would be diminished. For example, if  $H_{si}$  is only 5 nm, the minimum operating voltage (for 6-sigma cell yield) for the notched quasi-planar SRAM cell is  $\sim 0.9V$ . Thus, the value of  $H_{si} = 10$  nm chosen in this work represents a good trade-off between manufacturability and performance/scalability.

## 6.6 References

- [1] H. S. Yang, R. Wong, R. Hasumi, Y. Gao, N. S. Kim, D. H. Lee, S. Badrudduza, D. Nair, M. Ostermayr, H. Kang, H. Zhuang, J. Li, L. Kang, X. Chen, A. Thean, F. Arnaud, L. Zhuang, C. Schiller, D. P. Sun, Y. W. Teh, J. Wallner, Y. Takasu, K. Stein, S. Samavedam, D. Jaeger, C. V. Baiocco, M. Sherony, M. Khare, C. Lage, J. Pape, J. Sudijono, A. L. Steegen, and S. Stiffler, "Scaling of 32nm low Power SRAM with high-K metal gate," *IEDM Tech. Dig.*, 2008, pp. 233-236.
- [2] H. Kawasaki, M. Khater, M. Guillorn, N. Fuller, J. Chang, S. Kanakasabapathy, L. Chang, R. Muralidhar, K. Babich, Q. Yang, J. Ott, D. Klaus, E. Kratschmer, E. Sikorski, R. Miller, R. Viswanathan, Y. Zhang, J. Silverman, Q. Ouyang, A. Yagishita, M. Takayanagi, W. Haensch, and K. Ishimaru, "Demonstration of highly scaled FinFET SRAM cells with high-K/metal gate and investigation of characteristic variability for the 32nm node and beyond," *IEDM Tech. Dig.*, 2008, pp. 237-240.
- [3] B. S. Haran, A. Kumar, L. Adam, J. Chang, V. Basker, S. Kanakasabapathy, D. Horak, S. Fan, J. Chen, J. Faltermeier, S. Seo, M. Burkhardt, S. Burns, S. Halle, S. Holmes, R. Johnson, E. McLellan, T. M. Levin, Y. Zhu, J. Kuss, A. Ebert, J. Cummings, D. Canaperi, S. Paparao, J. Arnold, T. Sparks, C. S. Koay, T. Kanarsky, S. Schmitz, K. Petrillo, R. H. Kim, J. Demarest, L. F. Edge, H. Jagannathan, M. Smalley, N. Berliner, K. Cheng, D. LaTulipe, C. Koburger, S. Mehta, M. Raymond, M. Colburn, T. Spooner,

- V. Paruchuri, W. Haensch, D. McHerron, and B. Doris, "22nm technology compatible fully functional  $0.1\mu\text{m}^2$  6T-SRAM cell," *IEDM Tech. Dig.*, 2008, pp. 625-628.
- [4] C. H. Diaz, K. Goto, H. T. Huang, Y. Yasuda, C. P. Tsao, T. T. Chu, W. T. Lu, V. Chang, Y. T. Hou, Y. S. Chao, P. F. Hsu, C. L. Chen, K. C. Lin, J. A. Ng, W. C. Yang, C. H. Chen, Y. H. Peng, C. J. Chen, C. C. Chen, M. H. Yu, L. Y. Yeh, K. S. You, K. S. Chen, K. B. Thei, C. H. Lee, S. H. Yang, J. Y. Cheng, K. Y. Huang, J. J. Liaw, Y. Ku, S. M. Jang, H. Chuang, and M. S. Liang, "32nm gate-first high-K/metal-gate technology for high performance low power applications," *IEDM Tech. Dig.*, 2008, pp. 629-632.
- [5] F. Arnaud, J. Liu, Y. M. Lee, K. Y. Lim, S. Kohler, J. Chen, B. K. Moon, C. W. Lai, M. Lipinski, L. Sang, F. Guarin, C. Hobbs, P. Ferreira, K. Ohuchi, J. Li, H. Zhuang, P. Mora, Q. Zhang, D. R. Nair, D. H. Lee, K. K. Chan, S. Satadru, S. Yang, J. Koshy, W. Hayter, M. Zaleski, D. V. Coolbaugh, H. W. Kim, Y. C. Ee, J. Sudijono, A. Thean, M. Sherony, S. Samavedam, M. Khare, C. Goldberg, and A. Steegen, "32nm general purpose bulk CMOS technology for high performance applications at low voltage," *IEDM Tech. Dig.*, 2008, pp. 633-636.
- [6] E. Josse, S. Parihar, O. Callen, P. Ferreira, C. Monget, A. Farcy, M. Zaleski, D. Villanueva, R. Ranica, M. Bidaud, D. Barge, C. Laviro, N. Auriac, C. Le Cam, S. Harrison, S. Warrick, F. Leverd, P. Gouraud, S. Zoll, F. Guyader, E. Perrin, E. Baylac, J. Belledent, B. Icard, B. Minghetti, S. Manakli, L. Pain, V. Huard, G. Ribes, K. Rochereau, S. Bordez, C. Blanc, A. Margain, D. Delille, R. Pantel, K. Barla, N. Cave, M. Haond, "A cost-effective low power platform for the 45-nm technology node," *IEDM Tech. Dig.*, 2006, pp. 1-4.
- [7] B. Nikolić, C. Shin, M.-H. Cho, X. Sun, T.-J. King Liu, and B.-Y. Nguyen, "SRAM design in fully-depleted SOI technology," *Proc. IEEE ISCAS*, 2010, pp. 1707-1710.
- [8] K. Nii, M. Yabuuchi, Y. Tsukamoto, S. Ohbayashi, Y. Oda, K. Usui, T. Kawamura, N. Tsuboi, T. Iwasaki, K. Hashimoto, H. Makino and H. Shinohara, "A 45-nm single-port and dual-port SRAM family with robust read/write stabilizing circuitry under DVFS environment," *VLSI Symp. Circuits Dig.*, 2008, pp. 212-213.
- [9] A. Asenov, "Simulation of statistical variability in nano MOSFETs," *VLSI Symp. Tech. Dig.*, 2007, pp. 86-87.
- [10] H. Pilo, J. Barwin, G. Bracer, C. Browning, S. Burns, J. Gabric, S. Lamphier, M. Miller, A. Roberts, and F. Towler, "An SRAM design in 65nm and 45nm technology nodes featuring read and write-assist circuits to expand operating voltage," *VLSI Symp. Circuits Dig.*, 2006, pp. 15-16.
- [11] K. Zhang, U. Bhattacharya, Z. Chen, F. Hamzaoglu, D. Murray, N. Vallepalli, Y. Wang, B. Zheng, and M. Bohr, "A 3 GHz 70Mb SRAM in 65nm CMOS technology with integrated column-based dynamic power supply," *Proc. ISSCC*, 2005, pp. 474-475.
- [12] A. Asenov, S. Saini, "Suppression of random dopant-induced threshold voltage fluctuations in sub- $0.1\mu\text{m}$  MOSFET's with epitaxial and  $\delta$ -doped channels," *IEEE Trans. Electron Devices*, vol. 46, no. 8, pp. 1718-1724, Aug. 1999.
- [13] K. Takeuchi, R. Koh, T. Mogami, "A study of the threshold voltage variation for ultra-small bulk and SOI CMOS," *IEEE Trans. Electron Devices*, vol. 48, no. 9, pp. 1995-2001, Sep. 2001.

- [14] K. J. Kuhn, "Reducing variation in advanced logic technologies: approaches to process and design for manufacturability of nanoscale CMOS," *IEDM Tech. Dig.*, 2007, pp. 471-474.
- [15] C. Shin, M.-H. Cho, Y. Tsukamoto, B.-Y. Nguyen, C. Mazuré, B. Nikolić, and T.-J. King Liu, "Performance and area benefits of FD-SOI technology for 6-T SRAM cells at the 22nm node", *IEEE Trans. Electron Devices*, vol. 57, no. 6, pp. 1301-1309, Jun. 2010.
- [16] M. Jurczak, T. Skotnicki, M. Paoli, B. Tormen, J. Martins, J. L. Regolini, D. Dutartre, P. Ribot, D. Lenoble, R. Pantel, and S. Monfray, "Silicon-on-nothing (SON) – an innovative process for advanced CMOS," *IEEE Trans. Electron Devices*, vol. 47, no. 11, pp. 2179-2187, Nov. 2000.
- [17] T. Park, S. Choi, D. H. Lee, J. R. Yoo, B. C. Lee, J. Y. Kim, C. G. Lee, K. K. Chi, S. H. Hay, S. J. Hynn, Y. G. Shin, J. N. Han, I. S. Park, U. I. Chune, J. T. Moon, E. Yoon, and J. H. Lee, "Fabrication of body-tied FinFETs (Omega MOSFETs) using bulk Si wafers," *VLSI Symp. Tech. Dig.*, 2003, pp. 135-136.
- [18] X. Sun, Q. Lu, V. Moroz, H. Takeuchi, G. Gebara, J. Wetzel, S. Ikeda, C. Shin, and T.-J. King Liu, "Tri-gate bulk MOSFET design for CMOS scaling to the end of the roadmap," *IEEE Electron Device Lett.*, vol. 29, no. 5, pp. 491-493, May 2008.
- [19] C. H. Tsai, T.-J. King Liu, S. H. Tsai, C. F. Chang, Y. M. Tseng, R. Liao, R. M. Huang, P. W. Liu, C. T. Tsai, C. Shin, B. Nikolić, C. W. Liang, "Segmented tri-gate CMOS technology for device variability improvement," *Proc. IEEE VLSI-TSA*, 2010, pp. 114-115.
- [20] C. Shin, C. H. Tsai, M. H. Wu, C. F. Chang, Y. R. Liu, C. Y. Kao, G. S. Lin, K. L. Chiu, C.-S. Fu, C.-T. Tsai, C. W. Liang, B. Nikolić, T.-J. King, Liu, "Tri-gate bulk CMOS technology for improved SRAM scalability," *Proc. IEEE ESSDERC*, 2010, pp. 142-145.
- [21] A. Hori, T. Hirai, M. Tanaka, H. Nakaoka, H. Umimoto, and M. Yasuhira, "A 0.1  $\mu\text{m}$  CMOS with a step channel profile formed by ultra high vacuum CVD and in-situ doped ions," *IEDM Tech. Dig.*, 1993, pp. 909-911.
- [22] K. Noda, T. Uchida, T. Tatsumi, T. Aoyama, K. Nakajima, H. Miyamoto, T. Hashimoto, and I. Sasaki, "0.1  $\mu\text{m}$  delta-doped MOSFET using post low-energy implanting selective epitaxy," *VLSI Symp. Tech. Dig.*, 1994, pp. 19-20.
- [23] K. Noda, T. Tatsumi, T. Uchida, K. Nakajima, H. Miyamoto, and C. Hu, "A 0.1- $\mu\text{m}$  delta-doped MOSFET fabricated with post-low-energy implanting selective epitaxy," *IEEE Trans. Electron Devices*, vol. 45, no. 4, pp. 809-814, Apr. 1998.
- [24] T. Ohguro, H. Naruse, H. Sugaya, H. Kimijima, E. Morifuji, T. Yoshitomi, T. Morimoto, H. S. Momose, Y. Katsumata, and H. Iwai, "0.12  $\mu\text{m}$  raised gate/source/drain epitaxial channel NMOS technology," *IEDM Tech. Dig.*, 1998, pp. 927-930.
- [25] S. Song, W. S. Kim, J. S. Lee, T. H. Choe, J. H. Choi, M. S. Kang, U. I. Chung, N. I. Lee, K. Fujihara, H. K. Kang, S. I. Lee, and M. Y. Lee, "Design of sub-100nm CMOSFETs: gate dielectrics and channel engineering," *VLSI Symp. Tech. Dig.*, 2000, pp. 190-191.

- [26] S. Song, J. H. Yi, W. S. Kim, J. S. Lee, K. Fujihara, H. K. Kang, J. T. Moon, and M. Y. Lee, "CMOS device scaling beyond 100nm," *IEDM Tech. Dig.*, 2000, pp. 235-238.
- [27] A. Hokazono, H. Itokawa, N. Kusunoki, I. Mizushima, S. Inaba, S. Kawanaka, and Y. Toyoshima, "Steep channel & halo profiles utilizing boron-diffusion-barrier layer (Si:C) for 32nm node and beyond," *VLSI Symp. Tech. Dig.*, 2008, pp. 112-113.
- [28] S. Wolf, *Silicon Processing for the VLSI Era*, vol. 3, Lattice Press.
- [29] E. Seevinck, F. J. List, and J. Lohstroh, "Static-noise margin analysis of MOS SRAM cells," *Journal of Solid-State Circuits*, vol. 22, no. 5, pp. 748-754, Oct. 1987.
- [30] C. Wann, R. Wong, D. J. Frank, R. Mann, S.-B. Ko, P. Croce, D. Lea, D. Hoyniak, Y.-M. Lee, J. Toomey, M. Weybright, J. Sudijono, "SRAM cell design for stability methodology," *Proc. IEEE VLSI-TSA*, Apr. 2005, pp. 21-22.
- [31] E. Grossar, M. Stucchi, K. Maex, and W. Dehaene, "Read stability and write-ability analysis of SRAM cells for nanometer technologies," *Journal of Solid-State Circuits*, vol. 41, no. 11, pp. 2577-2588, Nov. 2006.
- [32] A. E. Carlson, "Device and circuit techniques for reducing variation in nanoscale SRAM," Ph.D. dissertation, Univ. California Berkeley, Berkeley, CA, May 2008.
- [33] K. Patel, T.-J. King Liu, and C. J. Spanos, "Gate line edge roughness model for estimation of FinFET performance variability," *IEEE Trans. Electron Devices*, vol. 56, no. 12, pp. 3055-3063, Dec. 2009.
- [34] N. Sano, K. Matsuzawa, M. Mukai, and N. Nakayama, "Role of long-range and short-range coulomb potentials in threshold characteristics under discrete dopants in sub-0.1  $\mu\text{m}$  Si-MOSFETs," *IEDM Tech. Dig.*, 2000, pp. 275-278.
- [35] C. Shin, X. Sun, and T.-J. King Liu, "Study of random-dopant-fluctuation (RDF) effects for the trigate bulk MOSFET," *IEEE Trans. Electron Devices*, vol. 56, no. 7, pp. 1538-1542, Jul. 2009.
- [36] M. J. M. Pelgrom, A. Duinmaijer, and A. Welbers, "Matching properties of MOS transistors," *IEEE J. Solid-State Circuits*, vol. 24, no. 5, pp. 1433-1440, Oct. 1989.
- [37] H. Dadgour, K. Endo, V. De, and K. Banerjee, "Modeling and analysis of grain-orientation effects in emerging metal-gate devices and implications for SRAM reliability," *IEDM Tech. Dig.*, 2008, pp. 705-708.
- [38] A. Cathignol, B. Cheng, D. Chanemougame, A. R. Brown, K. Rochereau, G. Ghibaud, and A. Asenov, "Quantitative evaluation of statistical variability sources in a 45-nm technological node LP N-MOSFET," *IEEE Electron Device Lett.*, vol. 29, no. 6, pp. 609-611, Jun. 2008.
- [39] Z. Guo, A. Carlson, L.-T. Pang, K. T. Duong, T.-J. King Liu, B. Nikolić, "Large-scale SRAM variability characterization in 45nm CMOS," *Journal of Solid-State Circuits*, vol. 44, no. 11, pp. 3174-3192, Nov. 2009.
- [40] U.S. Patent 7,190,050.
- [41] X. Sun, V. Moroz, N. Damrongplasit, C. Shin, and T.-J. King Liu, "Variation study of the tri-gate bulk MOSFET design," *IEEE Trans. Electron Devices*, submitted, Jan. 2011.

# Chapter 7

## Conclusion

Since 1958 when Jack Killby invented the integrated circuit (IC), improvements in IC performance and cost reduction have been successfully enabled by the steady miniaturization of the transistor (*i.e.*, minimum pitch is reduced by a factor of 0.7 in every new technology generation). However, increasing variation in transistor performance with miniaturization is a major challenge for continued planar-bulk/PD-SOI CMOS technology advancement [1, 2] to 22nm node and beyond, particularly, for SRAM scaling. Increased transistor mismatch results in lower SRAM bit-cell yield, and hence threatens to limit cell-area scaling and/or operating voltage ( $V_{DD}$ ) reduction. Advanced transistor structures which suppress short-channel effects more effectively than conventional bulk/PD-SOI MOSFET structures, without the need for heavy channel doping, will be needed to overcome the challenge and therefore enhance SRAM yield for sub-22 nm CMOS technology nodes. Hence, the formidable challenge, *i.e.*, variability, presents an opportunity for the introduction of variation-robust transistor architectures at the 22nm node. For this reason, this dissertation investigates the benefits of various alternate transistor designs.

### 7.1 Contributions of This Work

The first part of this dissertation investigated the fully-depleted silicon-on-insulator (FD-SOI) MOSFET structure with very thin-BOX (buried Oxide) of 10nm, from the perspective of the performance and area scaling benefits for 6-T SRAM cells at 22nm node [3, 4]. Via three-dimensional (3-D) process and device simulations, thin-BOX FD-SOI and planar bulk CMOSFET designs for low-operating-power (LOP) CMOS technology at the 22nm node were optimized. For the same standby-power consumption (*i.e.*, at comparable  $I_{OFF}$ ), the FD-SOI device achieves ~ 40% higher performance and ~50% lower threshold-



voltage ( $V_{TH}$ ) variation, as compared against the planar bulk device. Based on the optimized design of each device structure, 6-T SRAM cell performance metrics such as static-noise-margin (SNM), write-ability current ( $I_w$ ), and read current ( $I_{read}$ ) are quantitatively estimated and compared, using an analytical model fit to the simulated transfer characteristics for the optimized device designs. For the fixed cell area (*i.e.*,  $0.075\mu m^2$ ), FD-SOI technology was found to provide for improved SNM yield (by  $1.2\sigma$ ), and  $I_w$  yield (by  $2.2\sigma$ ). For the fixed yield of six cell-sigma in the planar bulk SRAM cell (*i.e.*, 1 failure out of 505 million), the FD-SOI cell provides an area savings of  $\sim 25\%$ . Lastly but not least, the minimum operating voltage for  $6\sigma$  yield ( $V_{min}$ ) is  $\sim 0.6V$  for the FD-SOI cell whereas it is  $>0.8V$  for the planar bulk cell. Thus, thin-BOX FD-SOI technology can facilitate the scaling of 6-T SRAM cell area and operating voltage. A challenge, which the industry is currently facing to reap the full benefits of FD-SOI technology, is the higher cost of silicon-on-insulator (SOI) substrates.

The rest of this dissertation theoretically/experimentally investigated the benefits of the quasi-planar bulk MOSFET structure for extending dimensional and voltage scaling of CMOS devices, particularly to guide the semiconductor industry in its efforts to simply and cost-effectively increase the storage density and yield (cost) of static-memory (SRAM) arrays. The quasi-planar bulk MOSFET is proposed and researched to preserve the advantages of a conventional planar bulk MOSFET (*e.g.*, already-developed stress engineering techniques, dynamic threshold voltage control, established compact model, and particularly very low substrate cost), along with the advantages of a multi-gate MOSFET (*e.g.*, enhanced short-channel control, improved performance and scalability).

A simple approach for manufacturing quasi-planar bulk MOSFET structures is experimentally demonstrated and shown to be effective not only for improving device performance but also for reducing variation in 6T-SRAM read and write margins, in an early 28nm CMOS technology [5, 6, 7]: a timed dilute-HF (hydrofluoric) etch is used to slightly recess the shallow trench isolation (STI) oxide just prior to gate-stack formation, resulting in gate electrodes that each wrap around the top portion of their respective MOSFET channel region. With optimization of the pocket implant doses (*i.e.*, lowering the dose by  $10^{13}cm^{-2}$ ), voltage scaling down to 0.8V is also facilitated. Since its benefits increase with decreasing channel width, the benefits of the quasi-planar bulk MOSFET technology should be increasingly significant for future CMOS technology generations (22nm and beyond). Note that the control of the oxide recess depth can be improved by selectively increasing the wet etch rate down to a precise depth, by Ar ion implantation [8].

As compared against a planar bulk MOSFET, the quasi-planar bulk MOSFET provides for larger drive current and reduced  $V_{TH}$  variation, due to improved gate control [9]. As a result, quasi-planar bulk SRAM cells are projected to have enhanced write-ability current and faster write time for comparable read stability, as well as  $>1$  sigma improvement in cell yield. Additionally, a notchless quasi-planar bulk SRAM cell design [7, 9] is proposed for

improved lithographic printability and either smaller area or lower standby power, and is projected to achieve 6-sigma cell yields at operating voltages down to  $\sim 0.8V$ .

Random dopant fluctuation (RDF) effects on the quasi-planar bulk MOSFET vs. the planar bulk MOSFET is studied using atomistic three-dimensional device simulation, for devices with 20 nm gate length [10]. Due primarily to better gate-to-channel control, the quasi-planar bulk MOSFET structure is more robust to RDF than a planar bulk MOSFET structure with identical nominal body and source/drain doping profiles and layout width. In addition, it is revealed that precise control of the body/channel doping profile is critical for minimizing  $V_{TH}$  variation in a bulk MOSFET technology. Lastly, the quasi-planar bulk MOSFET offers a new method of variation-robust  $V_{TH}$  adjustment, via tuning of the retrograde body/channel doping depth: it can mitigate the tradeoff between  $V_{TH}$  variation and short-channel effect control, for planar bulk MOSFETs.

Full 3-D 6T-SRAM cell simulations are used to assess the benefits of the quasi-planar bulk MOSFET structure at the 22nm node. The quasi-planar bulk technology (particularly, the Segmented-FET-based SRAM using the quasi-planar bulk technology [11]) is projected to achieve enhanced read stability and write-ability, improved SRAM cell yield, and improved immunity to single-event-upset.

Today, planar FD-SOI technology offers an excellent value proposition for low power products. As discussed in the Chapter 2, a planar FD-SOI technology is projected to reduce  $V_{TH}$  variation by  $\sim 50\%$  (resulting in higher SRAM yield and lower  $V_{min}$ ) and improved  $I_{ON}/I_{OFF}$  (facilitating lower  $V_{DD}$  for digital logic) as compared against a conventional planar bulk technology. Recently, a team of SOI Industry Consortium members designed an ARM Cortex<sup>TM</sup>-M0 core [12] and demonstrated that planar FD-SOI technology enables designers to reduce  $V_{DD}$  to  $\sim 0.7V$  to reduce the overall power consumption while meeting performance requirements. A practical issue for FD-SOI technology is the higher cost of silicon-on-insulator (SOI) substrates, particularly those with thin BOX ( $\sim 10nm$ ) and thin Si ( $\sim 10nm$ ) layers. To provide a lower-cost alternative to improving yield and lower power consumption, the quasi-planar bulk MOSFET has been proposed and investigated in Chapters 3 to 6. It is shown to preserve the advantages of a conventional planar bulk technology (compatibility with strain engineering techniques for enhanced mobility, dynamic threshold voltage control, an established compact device model, and low substrate cost) while offering the advantages of a multi-gate technology (improved performance and scalability). The benefits of quasi-planar bulk MOSFET technology will only increase with transistor scaling, since decreasing channel width results in improved electrostatic integrity, so that it is a compelling solution for CMOS scaling to the end of the technology roadmap (sub-10nm gate lengths). Note that Table 7.1 summarizes some main advantages and disadvantages of each technology.

Devices	Variability	Short-channel-effect (SCE) or electrostatic Integrity	SRAM (area, $V_{min}$ , yield)	Cost	Process maturity
Planar Bulk	<ul style="list-style-type: none"> <li>× Large random variation</li> <li>- doped channel for multi <math>V_{TH}</math> ; more RDF</li> <li>× Scaling threatened by RDF</li> </ul>	<ul style="list-style-type: none"> <li>× Weak SCE</li> </ul>	<ul style="list-style-type: none"> <li>× &lt; 6 cell-sigma</li> <li>× Limited scaling with 6-T SRAM (8-T SRAM required for L1 cache)</li> </ul>	<ul style="list-style-type: none"> <li>✓ Bulk substrate</li> </ul>	<ul style="list-style-type: none"> <li>✓ Matured</li> </ul>
FD-SOI with thin-BOX	<ul style="list-style-type: none"> <li>✓ Small random variation</li> <li>- undoped channel</li> </ul>	<ul style="list-style-type: none"> <li>✓ Good SCE</li> <li>- higher gate-to-channel capacitive coupling</li> <li>- Thin BOX (vs. Thick BOX)</li> </ul>	<ul style="list-style-type: none"> <li>✓ &gt; 6 cell-sigma</li> <li>✓ <math>V_{min} \sim 0.60V</math></li> <li>✓ 6-T SRAM for L1~3</li> <li>✓ 30% cell-area saving</li> <li>✓ Good for LOP</li> <li>× Bad for HP (lower <math>I_{ON}</math>)</li> </ul>	<ul style="list-style-type: none"> <li>× Expensive thin-BOX SOI substrate</li> <li>✓ Ion-implantation-free</li> </ul>	<ul style="list-style-type: none"> <li>× Immatured</li> <li>× Additional I/O process</li> </ul>
Quasi-Planar Bulk	<ul style="list-style-type: none"> <li>✓ Small random variation</li> <li>- undoped channel</li> <li>- Retrograde channel doping (process-complexity)</li> </ul>	<ul style="list-style-type: none"> <li>✓ Good SCE</li> <li>- tri-gating effect</li> <li>- retrograde doping</li> <li>× Worse narrow width effect</li> <li>- compensated by the other</li> </ul>	<ul style="list-style-type: none"> <li>✓ &gt; 6 cell-sigma</li> <li>✓ <math>V_{min} \sim 0.65V</math></li> <li>✓ 6-T SRAM for L1~L3</li> <li>✓ 10% cell-area saving</li> <li>✓ Good for LOP and HP</li> </ul>	<ul style="list-style-type: none"> <li>✓ Bulk substrate</li> </ul>	<ul style="list-style-type: none"> <li>✓ Compatible to matured Planar Bulk</li> <li>✓ Ease for manufacture</li> </ul>

Table 7.1. Comparison of three different device architectures: Planar bulk technology, thin-BOX FD-SOI technology, and quasi-planar Bulk technology.

## 7.2 Suggested Future Work

In order to suppress  $V_{TH}$  mismatch and lower  $V_{DD}$ , an advanced transistor design that provides for reduced short-channel effects (*i.e.*, improved gate control over the channel potential) and hence reduced  $V_{TH}$  sensitivity to process-induced variations is needed to facilitate voltage scaling. In addition, circuit-design approaches for alleviating  $V_{TH}$  mismatch include the use of read-assist and write-assist techniques to enhance SRAM read and write margins, for example read/write-assist column circuitry, word-line bias, pulsed bit lines, and lower column supply voltages during write – which results in lower array efficiency (*i.e.*, larger array layout area). A layout-design approach for high manufacturability (*i.e.*, reducing lithography complexity) and for adaptive biasing should be explored. The proposed SRAM bit-cell layout below is able to reduce lithography resolution enhancement requirements by utilizing (i) a bar-type contact to connect transistor drain regions and gate-electrode in the bit-cell, (ii) separate active region for each transistor device (*i.e.*, no notch/jog in the active pattern). In addition, the proposed cell layout allows for external voltage-skew to be easily applied, for the purpose of both understanding read/write failure and adaptive biasing. The proposed bit-cell layout (**Fig. 7.1(a)**) can have various benefits as described below.

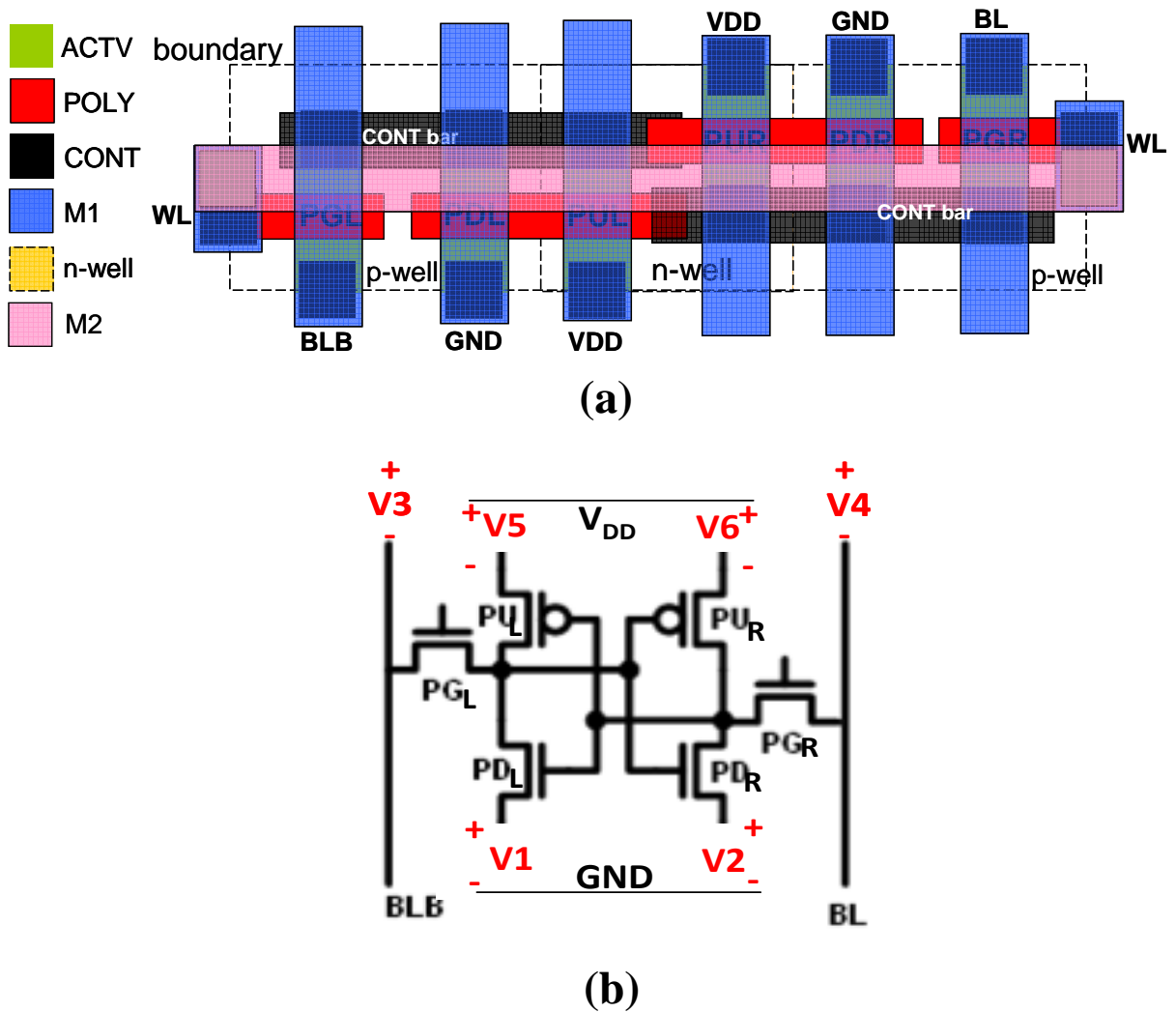


Figure 7.1. (a) Proposed new layout of the 6-T SRAM bit-cell. (b) Circuit schematic of the 6-T SRAM bit-cell showing how voltage skews can be implemented.

## A. Improved Manufacturability

In contrast to the conventional 6-T SRAM cell layout (**Fig. 7.2**) which has a jog/notch in the active pattern between pull-down and pass-gate transistor, and multi-patterned metal layers for connecting a storage node to the opposite input node, the proposed cell layout utilizes only rectangular features. Uni-directionality of patterns within each layer of the proposed layout (*i.e.*, active/metal 1 patterns running vertically, poly/contact/metal 2 patterns running laterally) makes it easier to print the patterns with high fidelity, so that less process-induced variations in channel length/width can be achieved. The bar-type contact reduces the total number of contacts within the cell (*i.e.*, 4 contacts *vs.* 6 contacts in the conventional 6-T SRAM cell), and thereby avoids issues caused by L-shaped contact.

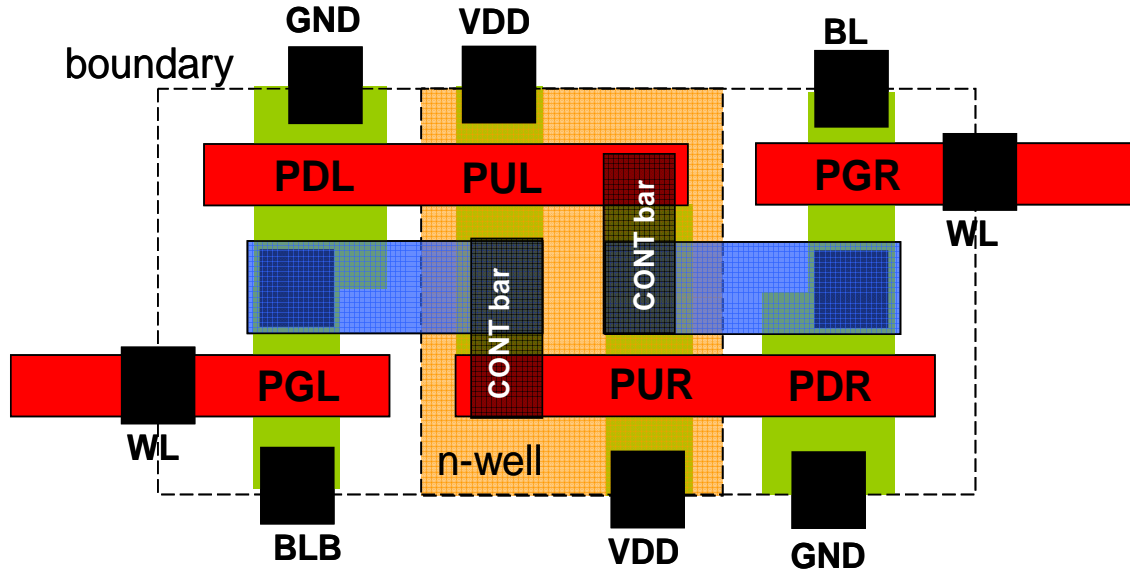


Figure 7.2. Conventional layout of a 6-T SRAM bit-cell.

## B. Independent Biasing of Transistors

As shown in the proposed cell layout (**Fig. 7.1(a)**), only two metal layers (*i.e.*, metal 1 running vertically and metal 2 running laterally) are required for read/write operations, if a bar-type contact is available in a given technology. With a separate active region for each transistor, it is possible to individually tune each one's gate overdrive, so that voltage-skew (as shown in **Fig. 7.1(b)**) can be introduced. This is useful for explaining SRAM read/write failure and allows for adaptive biasing to self-heal the cell. The number of externally-accessible nodes in the conventional SRAM cell layout is very limited unless every node is padded-out. Not only does this result in larger cell size, but also the padded-out cell will likely have different failure characteristics. It is also easy to independently adjust alpha/beta/gamma ratios of the cell, using external voltage-skews. Lastly, if the p-wells for pass-gate and pull-down devices are intrinsically separated by sufficiently deep shallow-trench-isolation (STI), independent biasing of the transistors can be easily implemented for adjusting the cell beta ratio and alpha ratio.

## C. Compatibility with Advanced Device Architectures

The proposed cell layout can be implemented with advanced CMOS devices including fully-depleted silicon-on-insulator (FD-SOI), FinFET, Tri-Gate MOSFETs, and quasi-planar MOSFETs. In addition, this cell can be easily implemented with corrugated-substrate technology [13], due to its regular active pattern.

## 7.3 References

- [1] M. J. M. Pelgrom, A. Duinmaijer, and A. Welbers, "Matching properties of MOS transistors," *IEEE J. Solid-State Circuits*, vol. 24, no. 5, pp. 1433–1440, Oct. 1989.
- [2] K. J. Kuhn, "Reducing variation in advanced logic technologies: Approaches to process and design for manufacturability of nanoscale CMOS," *IEDM Tech. Dig.*, Dec. 2007, pp. 471–474.
- [3] C. Shin, M. H. Cho, Y. Tsukamoto, B.-Y. Nguyen, C. Mazuré, B. Nikolić, and T.-J. King Liu, "Performance and area benefits of FD-SOI technology for 6-T SRAM cells at the 22nm node," *IEEE Trans. Electron Devices*, vol. 57, no. 6, pp. 1301–1309, Jun. 2010.
- [4] C. Shin, M. H. Cho, Y. Tsukamoto, B.-Y. Nguyen, B. Nikolić, and T.-J. King Liu, "SRAM yield enhancement with thin-BOX FD-SOI," *IEEE International SOI Conference*, Oct. 2009, pp. 1–4.
- [5] C. Shin, C. H. Tsai, M. H. Wu, C. F. Chang, Y. R. Liu, C. Y. Kao, G. S. Lin, K. L. Chiu, C.-S. Fu, C.-T. Tsai, C. W. Liang, B. Nikolić, and T.-J. King Liu, "Quasi-planar bulk CMOS technology for improved SRAM scalability," Special Issue for ESSDERC 2010, *Solid State Electron.*, to be printed in early 2011.
- [6] C.H. Tsai, T.-J. King Liu, S.H. Tsai, C.F. Chang, Y.M. Tseng, R. Liao, R.M. Huang, P.W. Liu, C.T. Tsai, C. Shin, B.Nikolić, C.W. Liang, "Segmented tri-gate CMOS technology for device variability improvement," *IEEE International Symposium on VLSI Technology Systems and Applications (VLSI-TSA)*, Apr. 2010, pp. 114–115.
- [7] C. Shin, B. Nikolić, T.-J. King Liu, C. H. Tsai, M. H. Wu, C. F. Chang, Y. R. Liu, C. Y. Kao, G. S. Lin, K. L. Chiu, C.-S. Fu, C.-T. Tsai, C. W. Liang, "Tri-gate bulk CMOS technology for improved SRAM scalability," *Proc. of European Solid-State Device Research Conference (ESSDERC)*, Sep. 2010, pp. 142–145.
- [8] X. Sun, Q. Lu, H. Takeuchi, S. Balasubramanian, and T.-J. King Liu, "Selective enhancement of SiO<sub>2</sub> etch rate by Ar-ion implantation for improved etch depth control," *Electrochemical and Solid-State Letters*, vol. 10, no. 9, pp. D89–D91, 2007.
- [9] C. Shin, N. Damrongplasit, X. Sun, Y. Tsukamoto, B. Nikolić, and T.-J. King Liu, "Performance and yield benefits of quasi-planar bulk technology for 6-T SRAM at the 22nm node," *IEEE Trans. Electron Devices*, to be appeared, 2011.
- [10] C. Shin, X. Sun, and T.-J. King Liu, "Study of random dopant fluctuation (RDF) effects for the tri-gate bulk MOSFET," *IEEE Trans. Electron Devices*, vol. 56, no. 7, pp. 1538–1542, Jul. 2009.
- [11] C. Shin, Y. Tsukamoto, X. Sun, and T.-J. King Liu, "Full 3D simulation of 6T-SRAM cells for the 22nm node," *IEEE International Conference on Simulation of Semiconductor Processes and Devices (SISPAD)*, Sep. 2009, pp. 1–4.
- [12] SOI consortium: <http://www.soiconsortium.org>
- [13] U.S. patent 7,190,050.